Zhaohui Wang

Aging of Si_3N_4-bonded SiC Sidewall Materials in Hall-Héroult Cells

Material Characterization and Computer Simulation

Thesis for the degree of Philosophiae Doctor

Trondheim, November 2010

Norwegian University of Science and Technology
Faculty of Natural Sciences and Technology
Department of Materials Science and Engineering

NTNU – Trondheim
Norwegian University of
Science and Technology

NTNU
Norwegian University of Science and Technology

Thesis for the degree of Philosophiae Doctor

Faculty of Natural Sciences and Technology
Department of Materials Science and Engineering

ISBN 978-82-471-2446-8 (printed ver.)
ISBN 978-82-471-2447-5 (electronic ver.)
ISSN 1503-8181

Doctoral theses at NTNU, 2010:229

Printed by NTNU-trykk

This thesis has been submitted to

Department of Materials Science and Engineering
Norwegian University of Science and Technology

in partial fulfillment of the requirements for
the academic degree

Philosophiae Doctor

September 2010

Acknowledgment

Time flies fast, I am soon approaching the finishing point of my 3 years PhD life. During these years, I have experienced both ups and downs like most others have done. Even though it has been very painful sometimes, this period has been one of the best times in my life. It is a great time to learn science, to know people and to know more about myself.

This thesis could not have been done without the help from a lot of people. First of all, I would like to thank my supervisor Prof. Tor Grande. His enthusiasm, intelligence and broad knowledge has been an invaluable source of the research. He always gave me encouragement and motivation by his warm smiling and valuable instructions throughout the work. He has been a wonderful support to me during these years. In fact, it was HIM who "opened" the way for me to this research field and brought me from an "embarrassed" master student to a "confident" PhD candidate. I appreciate and are proud to work with him. I thank him also for reading my numerous manuscripts for publications and the drafts of the thesis. All my publications and my thesis include his great efforts.

I am indebted to research manager Egil Skybakmoen from SINTEF for many valuable discussions about the project and his participation in some of my publications, as well as the help in autopsies and lab works. His helps were not limited in the research. He also introduced me to the sidewall block suppliers and gave me broad "eyes". I am grateful to chief scientist Asbjørn Solheim and senior adviser Christian Schøning from SINTEF. Their ideas, sometimes like a light in darkness, suddenly enlighten my work.

I would like to thank Hydro Aluminium AS for their 100% financial support throughout my PhD project and for allowing the publications during the work.

I am grateful to Dr. Jørn Lone Rutlin from Hydro Aluminium AS for reading my "long" manuscripts very patiently from time to time. His comments are always

helpful to improve both my scientific knowledge and my English. Thanks a lot! I thank him also for our frequently discussions about the research work. He gave me insights to the industry concerns. I am also grateful to Dr. Eirik Hagen, principal engineer Stanislaw Jarek and Dr. Ingo Eick from Hydro Aluminium AS for their valuable comments during meetings and personal communications.

There is one person I should give my special thank - my office mate - my "refractory twin" - Kati Tschöpe, a beautiful lovely German girl. She is my colleague, friend and sometimes my consulter of the life in European countries. Our daily discussion help the research work a lot and I feel sometimes discussion is more efficient than thinking alone. In addition, arguments make our "ideas" more clear and convincing.

I would like to thank all the people in Ceramic Group, both researchers and administrative persons. All our group seminars are impressive and they make our research life more social. Especially the "cake day". Thanks for all the traditional foreign cakes and sweets. Delicious!

I also would like to thank all people in the BIP group for their valuable suggestions and comments during all BIP meetings. Thank goes to Dr. Nancy Jorunn Holt for organizing all these wonderful meetings.

I would like to thank the technical staff for always being helpful, especially Eli Beate Jakobsen, Gunn Torill Wikdahl, Dr. Julian Tolchard from NTNU and Anne Støre, Ove Darell from SINTEF for instrument training and assistance in labs. Special thanks go to Dr. Yinda Yu for his assistance in TEM.

During all these years my family has always been there and helped me through difficult times. I have been traveling so far away from them for a long time, but I feel they are just around me and can give a hand anytime I need. I really appreciate it.

Specially, this thesis is devoted to my family and my deepest love ... no words can express my gratefulness to your unlimited support ...

Preface

The present dissertation is based on work carried out at Inorganic Materials and Ceramics Research Group, the Department of Materials Science and Engineering, the Norwegian University of Science and Technology (NTNU), under the supervision of Prof. Tor Grande. The work was done during the period August 16th 2007 to September 15th, 2010.

The PhD project is financed by Hydro Aluminium AS and is associated to the Project Innovations for High Current Density (PI-HDC), Sub-project 5 - Development of tools for simulation of degradation of cathode linings.

All experiments have been conducted by the author, except the following work. Transmission electron microscopy of the needle grains in the virgin and spent materials was operated by Dr. Yingda Yu at the Department of Materials Science and Engineering, NTNU. X-ray diffraction for samples from the spent sidewall block at the age of 604 days was done by CERAM Research Ltd, UK. LECO for samples from the spent sidewall block at the age of 604 and 1569 days was operated by Anne Støre (SINTEF).

Parts of this dissertation have been published in the following papers:

Zh. Wang, E. Skybakmoen and T. Grande, "Chemical Degradation of Si_3N_4-Bonded SiC Sidelining Materials in Aluminum Electrolysis Cells", *J. Am. Ceram. Soc.,* **92** [6] p1296-1302, 2009.

Zh. Wang, E. Skybakmoen and T. Grande, "Spent Si_3N_4 Bonded SiC Sidelining Materials in Aluminium Electrolysis Cells", *Light Metals (TMS)*, p353-358, 2009.

Zh. Wang and T. Grande, "Sodium Diffusion in Cathode Lining in Aluminium Electrolysis Cells", *Light Metals (TMS)*, p841-847, 2010.

Zh. Wang, E. Skybakmoen and T. Grande, "Thermal Conductivity of Si_3N_4-bonded SiC Sidewall Materials in Aluminium Electrolysis Cells", to be submitted.

Summary

Si_3N_4-bonded SiC materials have become the state-of-the-art sidewall block materials used in aluminium electrolysis cells. Despite its outstanding properties, the material properties degradate in the cell over time. The mineralogical transformations and chemical reactions cause changes in the physical and thermal properties, which influence the thermal balance of the electrolysis cell. Sodium plays an important role in the degradation of the sidewall block, as in the other parts of the cathode lining, and the transportation of sodium in the cathode lining has been in focus in the study in order to understand the degradation mechanisms.

Commercial virgin Si_3N_4-bonded SiC materials have been thoroughly characterized with respect to microstructure and phase composition. α-Si_3N_4 was found more pronounced in the area close to the surface of the virgin block than in the center by refinement of X-ray diffraction patterns. The morphology of the phases of the materials was investigated by scanning electron microscopy (SEM). The needle grains in the nitride binder were confirmed to be α-Si_3N_4 by transmission electron microscopy, while β-Si_3N_4 was proposed to be hexagonal rod shaped grains. The apparent porosity was lower in the area close to the surface while the density was higher.

The degradation of the Si_3N_4-bonded SiC materials was studied by investigating spent blocks. The degradation mechanisms in the gas zone (top part) and the electrolyte zone (bottom part) of the spent sidewall block were different due to the different chemical environments in the cell. In the electrolyte zone, the degradation involves reactions with sodium, and the main degradation phase was Na_2SiO_3 or a mixture of Na_2SiO_3 and $Na_2Si_2O_5$. The presence of only Na_2SiO_3 points to a higher chemical potential of sodium. The formed silicates filled up the pores and dramatically decreased the apparent porosity. The layer structure of the sodium silicate was confirmed by SEM. In the gas zone, the degradation mechanism was more complicated. The material underwent active oxidation, and the

main degradation phase was Si_2ON_2 or cristobalite depending on the partial pressure of oxygen. The apparent porosity and density of the bulk material was not significantly changed compared to the virgin material. At the surface of the block towards the pot, material loss was observed. The remaining material at the surface appeared porous and a significantly higher porosity was inferred. The needles in the binder in the gas zone was found thinner compared to the ones found in the virgin material. HF was proposed to play an important role in the material loss at the surface and the change in the morphology of the binder.

The thermal conductivity of the Si_3N_4-bonded SiC materials before and after operation was measured by the lasher flash method. The thermal conductivity was found to be higher in the area close to the surface of the virgin block than in the center despite a higher apparent porosity at the surface. Moreover, the thermal conductivity dropped dramatically in both the electrolyte zone and the gas zone of the spent blocks. The variation in the thermal conductivity of the material was modeled taking into account the phase composition, the apparent porosity and the microstructure related properties such as grain boundary resistance, pore shape and orientation factor and finally a thermal resistance layer. Both analytical models and computer simulations showed that the microstructure evolution had a strong influence on the thermal conductivity. Furthermore, the computer simulation demonstrated that the drop in the thermal conductivity of the sidewall block would result in a hotter surface of the block towards the bath and a thinner side ledge.

Sodium diffusion and reaction throughout the whole cathode lining has been investigated by a computer simulation by taking into consideration the different degradation mechanisms in each material of the cathode lining. The simulation demonstrated that the dominant transport of sodium in the carbon cathode was solid phase diffusion. The diffusion in the sidewall block was gas phase diffusion, and the diffusion is to some degree limited by the chemical reactions. Using the diffusion constant of sodium in the refractory layer close to the sodium self-diffusion in an albite like molten oxide reproduced the sodium penetration depth found in autopsies.

As shown in the work, sodium causes the severe degradation in the cathode lining. Moreover, it “opens” the way for the bath to penetrate into the cathode lining resulting in more severe degradation. Two approaches were applied to estimate the bath infiltration rate into the carbon cathode block. The simulations demonstrated that the infiltration rate was determined by the changes in the wetting property of the carbon material towards the bath, meaning that it was determined by the

sodium diffusion rate, which explains that sodium always infiltrates faster than the bath.

A diffusion barrier (like a steel plate or a chemical barrier) is recommended to be placed between the ramming paste (big joint) and the sidewall block, which could inhibit/reduce the sodium infiltration into the sidewall block and so eliminate further degradation. That will not only improve the chemical stability of the sidewall block but also its thermal stability, and thereby maintain the thermal balance during the cell operation. This may also open up for heat recovery from the heat flux through the side walls.

Contents

Chapter 1

Introduction

1.1 Background

Industrial production of primary aluminium is carried out in alumina reduction cells by the Hall-Héroult process. It is named after its inventors, Charles Martin Hall from the United States and Paul Louis Toussaint Héroult from France, who independently developed and patented an electrolytic process in 1886. During the process alumina (Al_2O_3) is dissolved in an electrolyte, consisting mainly of liquid cryolite, and is reduced at the cathode to produce molten aluminium [1–3]. Although there are many developments and modifications regarding process control and cell design, the main principle of the process remains unchanged. The overall electrochemical reaction is written as

$$2Al_2O_3(dis) + 3C(s) \longrightarrow 3CO_2(g) + 4Al(l) \tag{1.1}$$

As shown in this reaction, the carbon anode is consumed gradually during the process and gaseous carbon dioxide (CO_2) is produced. Based on the two basic anode designs, the alumina reduction cell can be classified into two categories: Söderberg cell and prebaked cell [2, 4]. A prebaked cell contains several single prebaked carbon anodes (mostly more than 20) depending on the cell design and line current. The prebaked anodes need to be replaced at regular intervals when they have reacted down to about 1/3 or 1/4 of its original height, usually after 22 to 26 days. In a Söderberg cell there is only one large carbon anode. Green paste is introduced on the top of the anode and self-baked during its movement from top to the bottom with the consumption of the bottom part of the anode. The Söderberg

anode can be used continuously which in principle is an advantage. Compared with the prebaked cells, however, the Söderberg cells are characterized by low current efficiency, high cell voltage, high energy consumption and high emissions (especially carcinogenic polycyclic aromatic hydrocarbons (PAHs)) and therefore are phased out gradually. Today all new built smelters adopt the prebaked anode technology. The reduction cell in this report refers to a prebaked cell. Figure 1.1 shows a schematic illustration of a typical prebaked reduction cell [5].

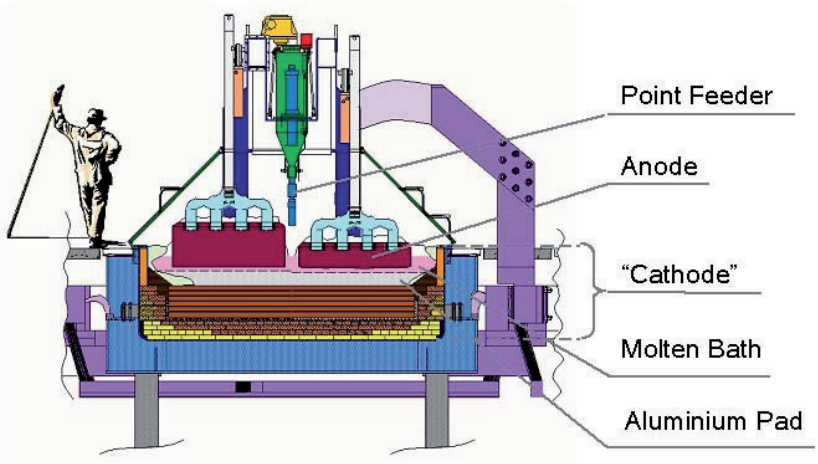

Figure 1.1: Schematic drawing of a typical prebaked reduction cell [5].

Theoretically, the amount of the aluminium produced in a cell is proportional to the potline current [2]. The primary aluminium production is energy demanding and has significant impact on the environment due to the emission of greenhouse gases such as CO_2 and perfluorocarbons (PFCs).

Numerous technical innovations and improvements have been performed in the primary aluminium industry, but several challenges still remain, such as:

- Increased productivity
- Longer lifetime of cells to minimize the significant relining costs
- Increased energy efficiency (reduced energy consumption per kilo aluminium)
- Reduced greenhouse gas emission

In brief the challenges are to produce cheaper aluminium and make the process

environmental friendly. The present thesis is related to the cathode lining materials in the cell. Actually, all the technical innovations and improvements need reliable lining materials as a basis in order to operate the cell for a prolonged time. Although the real working cathode in the aluminium electrolysis is the molten aluminium pad underneath the bath, shown in Figure1.1, the "cathode" in the industry commonly refers to the "container" of the molten metal and electrolyte, including the electrically conducting carbon lining with collector bars, refractories, insulations and sidewall blocks, which are enclosed in a supporting steel shell [3]. The "cathode lining" in this report refers to the carbon cathode, the refractory lining and the sidewall block[1]. A schematic drawing of the cathode lining is shown in Figure 1.2.

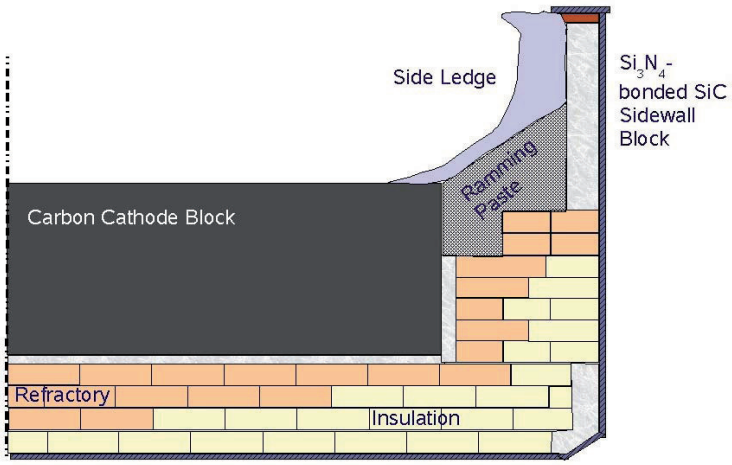

Figure 1.2: Schematic drawing of the cathode lining in a prebaked reduction cell.

The selection of the lining materials is to a large degree limited by the material cost. The materials need to be cheap and at the same time have good performance. To make a long story short, the state-of-the-art cathode lining materials widely used in the industry nowadays are the carbon cathodes based on semi-graphitized or graphitized carbon materials, Si_3N_4-bonded SiC materials for sidewall block and alumino-silicate based materials for refractory lining [6, 7]. The lining materials are inevitably degraded in the cell over time. The significant re-lining cost and requirement of the stable operation of the cell are the motivations for studying the degradation of the cathode lining materials.

[1]Insulation material is not taken into consideration in the present work.

A cell typically operates at a temperature around 955 to 965°C [1]. The molten electrolyte, which mainly contains liquid cryolite and additives such as AlF_3, CaF_2, LiF and MgF_2, is highly reactive. No material other than the frozen bath can withstand the aggressive bath for a prolonged time. The bath components and sodium formed during the electrolysis, act as two "degradation agents", both with a significant impact on the stability and the performance of the cathode lining materials.

Sodium will inevitably infiltrate/diffuse into the cathode carbon materials and form intercalation compounds during cell operation [3]. This causes swelling of the carbon cathode block and changes the bath chemistry. Moreover, it changes the wetting properties of the carbon cathode with respect to the liquid bath [8] and "opens" the way for the molten bath penetration. During operation, sodium followed by bath components will infiltrate downwards through the carbon block and deteriorate the refractory lining over time [9, 10].

Sidewall blocks are designed to be protected by a layer of "frozen bath", called the "side ledge" during operation. Si_3N_4-bonded SiC materials have during the last decades become the state-of-the-art sidewall block material in aluminium electrolysis cells due to its excellent oxidation resistance compared with traditional carbon lining, good cryolite resistance, low electrical conductivity, and high thermal conductivity. Despite their excellent properties, the materials are degradated in the cell over time [7, 11–14]. The development towards high amperage cells with thinner sidewall blocks [15] and the demand for longer pot lifetime call for a better understanding of the chemical stability of Si_3N_4-bonded SiC materials in the cell qualitatively and more important quantitatively. Moreover, the sidewall blocks are designed as "heat windows" in the cells from which around 35% of the heat loss is dispersed to the surroundings [2]. The understanding of the variation in the thermal property of the sidewall block during the cell operation, or say degradation, is important for the cell design and process control in order to keep the heat balance and operation of the cell stable. The possibility to develop cells with heat recovery by cooling the sidewall blocks [16] calls for an improved understanding of the thermal properties of the sidewall block materials and possible aging effects. It is also desired to develop analytical models and to use computer simulations to describe the variation of the thermal conductivity.

Sodium plays a crucial role in the degradation of the entire cathode lining. Sodium diffusion in carbon cathode materials [17, 18], sidewall materials [19] and degradation in the cathode lining have been studied separately, but studies taking into account the role of sodium in the entire cathode lining are lacking. The effort to

stop or hinder the sodium is still a matter of concern. It is helpful and important for both academia and industry to have an overall picture of sodium diffusion and reaction in the whole cathode lining by considering different degradation schemes in the layers and sodium mass balance of the cell.

1.2 Aim of the Work

The present research work has been associated with the project Innovations for High Current Density (PI-HDC) – Sub Project 5: "Develop tools for simulation of the degradation of the cathode linings in aluminium electrolysis cells". The project has been devoted to develop analytical models to describe the rate of aging and/or degradation based on the qualitative understanding of the aging phenomena. The research work in this thesis can be divided into four major topics.

The first part (Chapters 5 and 6) is devoted to the qualitative and quantitative understanding of the degradation mechanism of the cathode lining since it is critical for the development of a mathematical model for the degradation. Here the focus has been on Si_3N_4-bonded SiC sidewall blocks. An associated PhD project has in parallel focused on the refractory lining [20]. A thorough study of Si_3N_4-bonded SiC virgin blocks from different suppliers and spent sidewall blocks from autopsies was performed including quantitative chemical characterization and microstructure investigations. The degradation mechanisms in the bottom and the top part of the spent blocks were proposed based on the experimental observations.

The second part (Chapter 7) is related to the variation in thermal properties of the sidewall block due to aging. The heat balance of an aluminium electrolysis cell is critical to the operation control of the cell. Because of the importance of the sidewall block in keeping the heat balance of the cell, studies of the variation in the thermal conductivity of the sidewall block due to the aging is of great interest. The thermal conductivity of the virgin and spent sidewall blocks was measured using the laser flash method [21] and the data were correlated with the phase composition, apparent porosity and microstructure of both virgin and spent blocks. Analytical models and computer simulation were applied in order to analyze the influence of these factors on the thermal conductivity of the Si_3N_4-bonded SiC porous composite.

The third part (Chapter 8) is concerned with the sodium diffusion in the entire cathode lining including the carbon cathode block, the refractory and the sidewall block. Sodium formed on the carbon surface will diffuse not only into the the bottom lining but also into the sidewall block and cause degradation. Based on the reported material properties, computer simulation was introduced to give a better understanding of sodium diffusion and reaction behavior in the whole cathode lining on the basis of degradation mechanisms in each layer and the sodium mass balance in the cell.

The fourth part (Chapter 9) is related to the bath infiltration in the carbon cathode block. Sodium diffusion rate is reported faster than that of bath infiltration in the carbon cathode [3]. Based on the reported properties of the liquid bath including wetting angle, surface tension and pore size distribution of the carbon blocks, a computer simulation of two-phase flow (bath and air) in capillary pores and the calculation of static capillary force was carried out to explain the bath infiltration phenomenon. Estimation of the rate of sodium diffusion and bath infiltration was further discussed in relation to the sodium diffusion model presented in the second part of the thesis.

Computer simulation and analytical mathematical models were used frequently in the present thesis not only for demonstrating complicated processes as sodium diffusion and reaction in whole cathode lining, but also for fundamental studies like effective thermal conductivity of porous sidewall block materials and bath flow in micro-pores.

Chapter 2

Literature Review

2.1 SiC-based Sidewall Materials

2.1.1 Introduction

The sidewall is typically one layer of ceramic blocks placed around the steel shell. Ramming paste (big joint) is used to fill the gap between the sidewall blocks and the carbon cathode block. In a reduction cell, the sidewall contributes around 35% of the heat loss to the suroundings [2]. The heat flow through the sidewall should be carefully designed and controlled to maintain a stable layer of frozen electrolyte (side ledge), which is critical to maintain heat balance of the cell and protect the sidewall blocks.

The chemical attacks by air and/or other oxidizing gases, gaseous bath components from the pot gas and/or leakage of the cell, sodium penetration and sometimes direct bath infiltration (in case of lack of ledge) are the main reasons for chemical degradation of sidewall block materials. The degradation is expected to reduce the thermal conductivity of the lining over time [22, 23]. The drop in thermal conductivity increase the possibility of the unstable side ledge and the sidewall block will be more often exposed to molten and gaseous bath components. In the extreme case the gaseous components and even the molten bath may directly attack the steel shell. The subsequent metal exfoliation increases the risk of a tap-out of the cell and thereby cell failure.

A good sidewall block material needs to have the following properties [23, 24]:

- High resistance to molten aluminium
- High resistance to molten bath
- High resistance to CO_2/CO, O_2, HF and gaseous bath components
- Low porosity
- High strength
- Reasonably high thermal conductivity
- High bulk density
- High electrical resistivity
- Easy fabrication and jointing

2.1.2 Materials

The state-of-the-art sidewall block materials are SiC based materials. One of the main advantages of these materials over traditional anthracite and graphitized carbon materials is the significant better oxidation resistance. SiC materials can be divided into different groups according to different binding phases: Si_3N_4, silica, Si_2ON_2, Sialon bonded SiC and self-bonded SiC. Experiments have shown that dense self-bonded SiC block did not change at all [25], but it is limited by high fabrication cost [1]. Among all other materials, Si_3N_4-bonded SiC materials are the best due to a combination of good oxidation resistance and good cryolite resistance. They have gradually substituted the conventional carbon materials and have become the state-of-the-art sidewall block materials in the modern aluminium reduction cells due to increased anode size. The properties of Si_3N_4-bonded SiC block in comparison with other materials are listed in Table 2.1 [22].

Si_3N_4-bonded SiC materials are more expensive compared with the traditional carbon materials, but this is compensated by using thinner sidewall block in the cell and by the profits from a high productivity resulting from a higher current load on the pot line. There are several advantages of using these materials [15, 23, 27]:

- Thinner sidewall block can be used in the cell and yields a larger cell space which enables larger anodes
- Maintain a better side ledge and expect a longer pot life
- High amperage load can be introduced because more generated heat can be dispersed through the thin, high thermally conductive sidewall block

[1] Self-bonded SiC block is now appeared in the market with higher thermal conductivity and possibly higher cryolite resistance (Sicatec 95, LIRR, China) [26]. However, a longer evaluation time must be needed to confirm its performance in the industrial cells.

- Low electrical conductivity to avoid polarization during the electrolysis process
- Superior oxidation resistance to avoid air burn of the sidewall block
- Excellent erosion/corrosion resistance when directly exposed to bath or molten metal which occurs in the case of anode effects or unstable side ledges due to high bath temperature

2.1.3 Fabrication of Si_3N_4-Bonded SiC Sidewall Block

Si_3N_4-bonded SiC sidewall blocks are commonly made from a mixture of silicon carbide grains (in mm scale) and finely divided silicon (typically 325 mesh, less than 44μm) and a binder. SiC may have some impurities such as SiO_2, Si, Fe and C coming from the Acheson process. The green blocks are most commonly produced by slip casting, vibratory casting, or by pressing. The green bodies are fired in a furnace in a nitrogen atmosphere at temperatures below the melting point of silicon (1410°C [28]), normally around 1400°C. Beginning at approximately 1100 °C, the nitrogen gas and silicon metal react, forming silicon nitride (Si_3N_4) as a binder phase between large SiC grains. Due to the fact that the bonding phase grows within the existing porosity, there is almost no dimensional change upon firing and a net weight gain occurs. In a final block, the content of SiC is 72-80 wt% and of Si_3N_4 is 20-28 wt%. The material is porous and the porosity is around 13-17 vol%. The typical thickness of the blocks used in aluminium cells is 60-100 mm [7]. The fabrication process is illustrated in Figure 2.1.

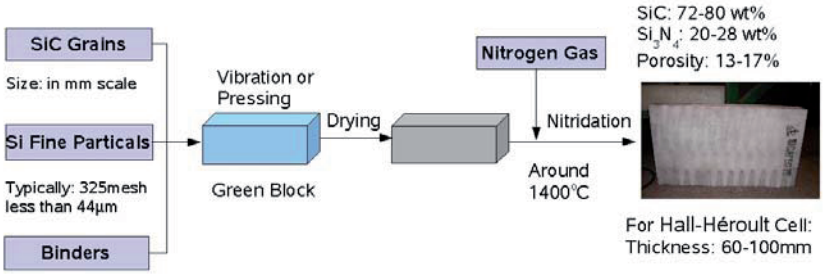

Figure 2.1: Schematic drawing of the fabrication of the Si_3N_4-bonded SiC sidewall block.

Since the nitridation reaction given by Equation (2.1) is strongly exothermic (ΔH°_{1673K} = -731.6 kJ/mol)[2], the reaction might become self-igniting and affect

[2] All thermodynamic calculations are done by using FactSage™ 5.2 [29]

Table 2.1: Composition and properties of SiC and carbon blocks [22].

	Si_3N_4 bonded SiC	**Silica bonded SiC**	**Si_2ON_2 bonded SiC**	**Sialon bonded SiC**	**Graphitized carbon**	**Anthracite carbon**
Composition						
SiC (%)	75-85	85	85	79		
SiO_2 (%)	1	9-13				3
Si_3N_4 (%)	13-23					
$Si_{6-z}Al_zO_zN_{8-z}$ (%)				20		
Si_2ON_2 (%)	0-5		13			
Properties						
Bulk density (g/cm^3)	2.63	2.50-2.55	2.60	2.70	1.6-1.7	1.5
Porosity (%)	17.0	10.0-20.0	15.0	15.0	20-22	16-18
Modulus of rupture at 20 °C (MPa)	35-45	20	24	45-55	10	6
Abrasion resistance	Good	Fair	Good	Very good	Very bad	Bad
Electrical resistivity (Ω cm) at 1000 °C	800	1000		800	0.007	0.05
Thermal conductivity (W/m·K) at 600 °C	16-18	14-16	19	16	80-100	7-10
Oxidation resistance	Good	Good	Very good	Very good	Bad	Bad
Resistance to combined Oxidation+cryolite attack	Very good	Poor	Poor	Fair	Bad	Bad

the furnace temperature dramatically. Industrially, the only realistic means of controlling the nitridation is keeping the N_2 pressure within appropriate limits [30].

$$3Si + 2N_2(g) = Si_3N_4 \tag{2.1}$$

The Si_3N_4 binder is never phase pure, it always consists of α-Si_3N_4 and β-Si_3N_4. The ratio of the two phases will vary according to the fabrication condition.

2.1.4 Formation of α-Si_3N_4 and β-Si_3N_4

The nitridation conditions, growth mechanisms and the properties of the two modifications of silicon nitride α-Si_3N_4 and β-Si_3N_4 have been intensively studied. Moulson [31], Jennings [32] and Wang [33] have given good reviews of the relevant topics.

The formation of the two polymorphs is mainly determined by kinetic factors rather than by thermodynamics. During the nitridation below the melting point of silicon, two reactions occur in parallel, one with volatilized silicon and the other with solid silicon. α-Si_3N_4 grows from the vapour phase reactions and stabilized by a small amount of oxygen. The growth morphology could be "massive" or "whiskers" depending upon the chemical nature of the reactants (Si, SiO, etc.). β-Si_3N_4 grows from direct nitridation of the solid silicon. The presence of liquid silicon, although not necessary, provides an easy diffusion path for atomic nitrogen and results in faster β-Si_3N_4 phase growth. The energetic difference between the two phases is small. α-Si_3N_4 is believed to be an oxynitride and is the low temperature metastable phase of silicon nitride. β-Si_3N_4 is the high temperature phase and is a pure silicon nitride. The two crystallographic structures of silicon nitride are shown in Figure 2.2 [34].

β-Si_3N_4 is the stable phase of silicon nitride at all temperature [35]. The transformation from α to β phase is displacive and depends on a solution - reprecipitation mechanism in a liquid phase. The reverse transformation has never been observed [32].

At the early stage of nitridation at low temperature, the formation of α-Si_3N_4 is extensive due to the oxygen contamination in the raw materials. When Si metal is directly exposed to N_2, especially liquid Si metal, formation of β-Si_3N_4 dominates [36].

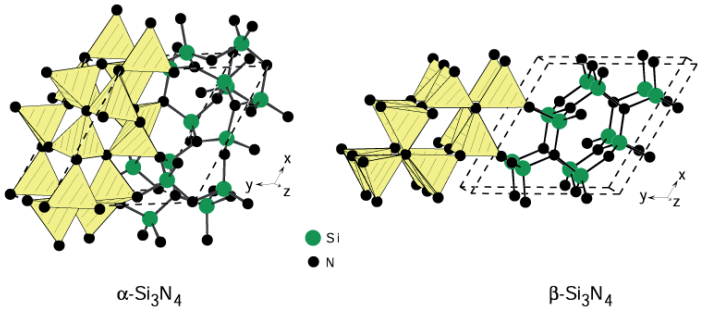

Figure 2.2: Crystal structures of trigonal α-Si_3N_4 (P31c) and hexagonal β-Si_3N_4 ($P6_3/m$), emphasizing the corner-sharing SiN_4 tetrahedra [34].

2.1.5 Degradation of Sidewall Block in Aluminium Electrolysis Cells

Although Si_3N_4-bonded SiC materials are superior to carbon materials with respect to oxidation and cryolite resistance, these materials degradate gradually over time in the cell [7, 11–14, 37].

The degradation of the sidewall block material could be characterized into three regions according to its position in the cell: Gas zone (above the bath level), electrolyte zone/bath zone (between the bath level and metal level) and aluminium zone/metal zone (below the electrolyte level). The chemical conditions are different in each region. Figure 2.3 illustrates the chemical conditions in the different zones [38].

The main attacking agents are $NaAlF_4$(g), oxidizing gases (air, CO(g), CO_2(g)), Na(g), cryolite and aluminium. Sodium is recognized in recent years [11, 38], which is formed on the carbon cathode by reactions (2.2) and (2.3).

Both autopsies and fundamental studies have been performed to investigate the degradation mechanisms in these three regions. It is commonly believed that the Si_3N_4 binding phase is the weak part of the materials and will be attacked more easily than the SiC phase [11, 23, 25]. An overall degradation scheme of the Si_3N_4-bonded SiC sidewall block in the aluminium electrolysis cell is illustrated in Figure 2.4.

Gas Zone: Si_3N_4-bonded SiC sidelining materials show good oxidation resistance due to the passive SiO_2 layer formed during reaction, which can protect the materials from further oxidation. Oxidation is controlled by both reaction at the

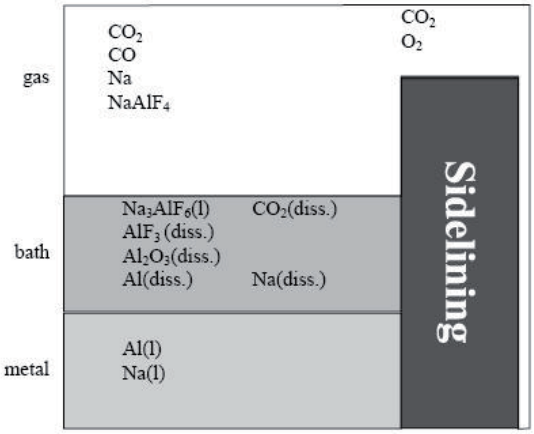

Figure 2.3: A schematic representation of the chemical environment in the surroundings of a sidelining (sidewall block) without the protection of a frozen ledge [38].

.

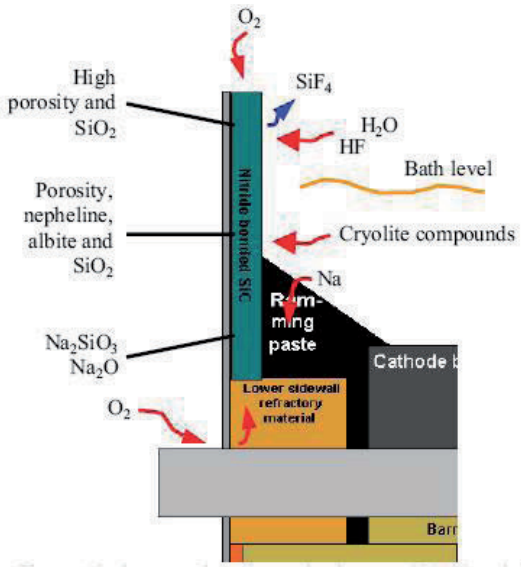

Figure 2.4: Suggested wear mechanism on Si_3N_4 bonded SiC in aluminium electrolysis cells [11].

.

interface and diffusion through the product layer [39]. The oxidation is dependent on the nature of the oxide layer, its density, and thickness. This silica layer is unfortunately easily attacked by cryolite when exposed to the bath. Moreover, both Si_3N_4 and SiC are unstable when CO_2 and $NaAlF_4$ are present (CO_2 is saturated with $NaAlF_4$). In this case $NaAlSiO_4$ and SiF_4(g) might be formed [25].

HF(g) has been also suggested to play a role [11]. HF(g) could be formed by the reaction between the bath and the moisture in the cell, for instance from the alumina feed. It acts as a destructive agent by forming SiF_4(g) from the SiO_2 around SiC grains and causes the detachment of SiC grains as shown in Figure 2.5.

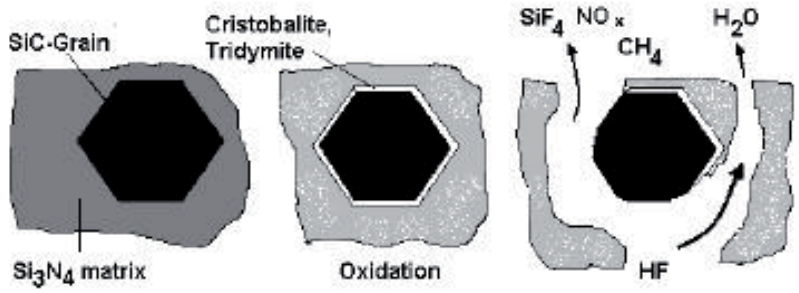

Figure 2.5: HF(g) attack on Si_3N_4 matrix [11].

.

The research related to the oxidation of the porous Si_3N_4-bonded SiC ceramics is not only limited to the aluminium industry. Quite a few fundamental studies have been performed [39–41].

Gao **et** *al.* [40] pointed out that the major cause of oxidation of these materials is the open porosity, which gives access to large internal surface area. The oxidation kinetics of the material can be described by a parabolic law at 1000°C and a asymptotic law at 1200°C in air and wet air environments shown in Figure 2.6(a). The oxidation could be separated into two stages. The first stage is a short linear weight increase since both internal and external surfaces of pores are oxidized. The oxidation rate is low in the second stage, since the pore channels become narrower and the effective area for the reaction is greatly reduced. Furthermore, water vapour is a more reactive oxidizing agent, shown in Figure 2.6(b), resulting from the rapid permeation of the oxide scale by H_2O molecules and devitrification of the amorphous silica is enhanced.

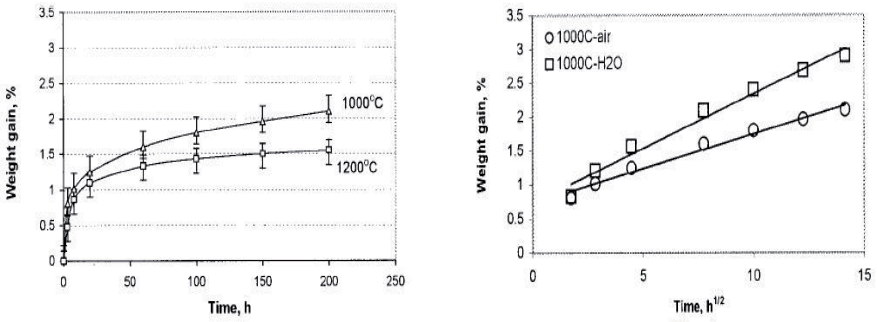

(a) Isothermal oxidation in air.

(b) Oxidation in air and wet air at 1000°C, described by a parabolic law.

Figure 2.6: Oxidation of Si_3N_4-bonded SiC ceramics in air and wet air [40].

Wang **et** *al.* [39] investigated systemically the oxidation reactions of Si_3N_4-bonded SiC ceramics by different oxidants: CO, CO_2 and steam. Oxidation of these materials is classified into passive and active oxidation. The study pointed out that the oxidation mechanism was determined by the chemical potential of oxidants. At high oxidant potential, the materials undergo passive oxidation and the oxidation product is a SiO_2 passive layer. The active oxidation happened at low oxidant potential and the oxidation product is SiO(g). They calculated the transition potential from active to passive oxidation in CO and CO_2 atmosphere as shown in Figure 2.7(a) and 2.7(b) respectively.

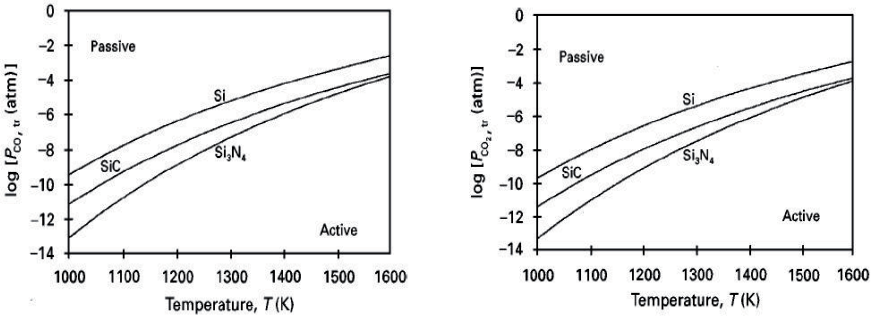

(a) In CO atmosphere.

(b) In CO_2 atmosphere.

Figure 2.7: Transition oxidant potential for oxidation of Si, SiC and Si_3N_4, (p_{N_2}=1atm) [39].

Chollon [41] studied the oxidation behavior of the ceramic fibers from the Si-C-N-O system including the oxidation of Si_3N_4 and SiC by O_2. The research

revealed that the oxidation mechanism for SiC and Si_3N_4 might be related to a complex diffusion/reaction regime via the formation of an intermediate oxide layer like silicon-oxynitride layer for Si_3N_4. The activation energies typically range from 330-490 kJ/mol for Si_3N_4 and 110-140 kJ/mol for SiC . Higher activation energy for Si_3N_4 has been attributed to the slow oxygen transport through the silicon oxynitride layer. Du **et** *al.* [42] proposed a lower permeability to oxygen of this sub-layer than SiO_2. The silicon oxynitride layer acting as a diffusion barrier and gradually increasing in thickness during oxidation would give rise to lower parabolic rates and a higher activation energy than those for SiC. Alternatively, Luthra [43,44] proposed a mixed interfacial reaction and nitrogen diffusion mechanism as rate controlling step.

Electrolyte Zone: The following reaction scheme was proposed in the electrolyte zone [7]:

- Penetration of Na
- Oxidation to Na_2O / formation of $Na_2O{\cdot}xSiO_2$
- Swelling/descaling/dissolution of the reaction products
- New reaction cycle

This reaction cycle is assumed to be especially damaging for materials with high content of oxides. Unpolarised test showed that Si_3N_4-SiC materials did not corrode at all when exposed to aluminium and cryolite at 1000°C for 720 h in argon atmosphere [25], which demonstrated the importance of the sodium in the degradation circle. The secondary phase $Na_2O{\cdot}SiO_2$ and/or $Na_2O{\cdot}2SiO_2$ will be formed around the SiC grains, introducing stress and strain in the grains. The grains may spall off to the bath or the whole SiC grains may be washed into the bath if locally the binder is consumed completely [13].

Pickrell et *al.* [45] showed that alkali corrosion of SiC and Si_3N_4 is surface reaction controlled. The activation energies are around 104 kJ/mol for SiC and 199 kJ/mol for Si_3N_4 respectively. The rate-controlling step in the corrosion process for both materials appears to be the interfacial oxidation of SiC or Si_3N_4 to SiO_2.

Aluminium Zone: Normally, bath/metal interface is the hottest place of the sidewall block and therefore has a thinnest side ledge. Consequently, the local sidewall block is more easy to be attacked by molten bath or aluminium directly. SiC and Si_3N_4 are not stable towards molten aluminium. Si metal and Al_4C_3

were found to be the reaction products according to Hagen **et** *al.* [38]. The product Al_4C_3 was also confirmed by Kvam **et** *al.* [13], besides, they suggested AlN might be another reaction product with Aluminium.

In the author's diploma work [19] a gaseous sodium diffusion route was proposed as shown in Figure 2.8. The author pointed out that it is due to the kinetics, not thermodynamics that Si_3N_4 is the weak part of the Si_3N_4 bonded-SiC sidewall block materials because Si_3N_4 particles have much larger surface area, especially α-Si_3N_4 with needle-like morphology. When exposed to degradation agents such as Na(g), oxidizing gases and fluoride gases these needles will react more easily compared with the large SiC grains.

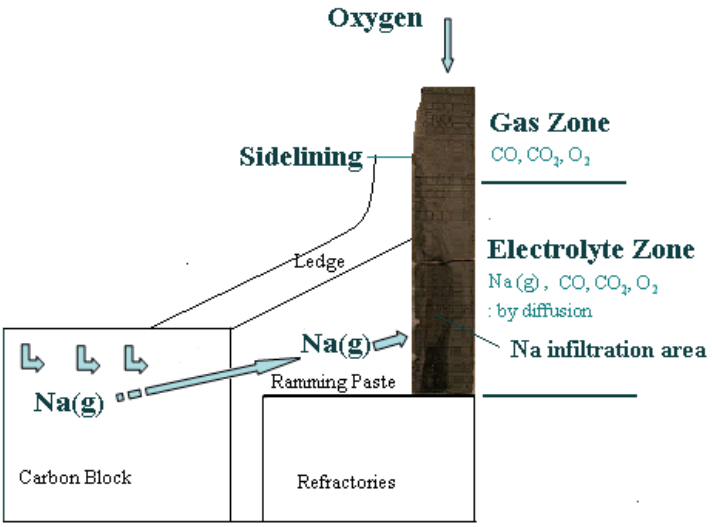

Figure 2.8: The proposed sodium diffusion route in the aluminium electrolysis cell [19].

The proposed degradation mechanisms were different in the gas zone and the electrolyte zone of the block. In the gas zone, the degradation is prefered to α-Si_3N_4, and Si_2ON_2 was found as the main degradation phase instead of SiO_2. Degradation in the infiltration area of the electrolyte zone exhibits Na(g) enhanced oxidation. Reaction product was mainly metasilicate, Na_2SiO_3 (flake like). The deterioration was more severe in the infiltrated area than that in the gas zone.

The mechanism for Na(g) infiltration is proposed to be gaseous diffusion through porous media. Na(g) will diffuse through the carbon block, ramming paste into the sidewall block materials via the pore system and reacts with Si_3N_4 binder

together with oxidizing gases coming from top of the sidelining since the pot is not air-tight. The gradually accumulated solid products will cover the pore surface, narrow the pores channels and fill up most of the open pores and densify the block, which will greatly retard Na(g) diffusion and further reactions.

Although many efforts have been done to describe the degradation of these materials in the aluminium electrolysis cell, the kinetics and the exact reaction mechanism are not well established, especially the quantitative understanding, and more systematic work is needed, especially for the sodium infiltration involved reactions.

To summarize, there are some properties that can affect the oxidation and chemical resistance of Si_3N_4-bonded SiC sidewall block materials:

- The pore size and pore size distribution
- The relative amount of Si_3N_4 and SiC
- The particle size and particle size distribution of SiC
- The amount of free silicon, the degree of nitration
- The amounts of SiO_2, Si_2ON_2 and SiAlON in virgin block
- The amounts and types of impurities
- The type of organic binder used before compression
- The homogeneity of the block

The properties of sidelining materials are important in order to have a good performance. Maintaining a stable side ledge during operation is however most essential for protecting sidewall blocks from chemical attacks.

2.2 Refractory Lining

The bottom lining consists of electrically conducting carbon blocks with current collector bars, refractory and insulation layers [3]. The refractory lining is located underneath the carbon block and usually consists of 2-3 layers of dense firebricks. The insulation layer is below the refractory lining and consists of 2-3 layers of porous insulation bricks or boards (slab) towards the steel shell. The dense refractory layer is used to:

- Protect the underlying porous insulating lining from sodium/molten fluorides infiltration
- Maintain the designed heat balance of the cell and reduce the vertical heat loss downward in the cell
- Keep the lining dimensionally stable and protect the steel shell from high temperature and penetrating bath and/or metal

2.2.1 Materials

The common refractory materials used in aluminum electrolysis cells are listed in Table 2.2. Among those alumino-silicates based materials are most commonly used. Firebricks (chamotte) with relatively high silica content (higher than 53 wt%) have long been the first choice based on their good performance, availability and low cost [9]. The refractory lining material discussed in this work is alumino-silicates based materials.

Table 2.2: Chemical composition and bulk density for the most common refractory materials used in aluminum electrolysis cell lining [46].

Material	**Chemical composition (wt%)**						**Bulk density**
	Al_2O_3	**SiO_2**	**MgO**	**CaO**	**Fe_2O_3**	**Na_2O**	**g/cm^3**
Alumina (powder)	100						1.0
Alumino-silicate							
High-alumina bricks	46-90	10-49					2.3-3.3
Firebricks	18-45	50-75	<0.5	<0.5	1-2	1-3	2.0-2.2
Anorthite							
Chemobar (powder)	3	48		15	1	3	2.1
Olivine							
Forsterite bricks		41	51		7		2.7
Dry Cast (powder)		44	37		5		2.3
Olibar 1901 (powder)	4	44	42		7		2.3

The insulation layer is designed to be protected by the refractory layer. The degradation in this layer has therefore not been a topic in the present project.

2.2.2 Degradation of Refractory in Aluminium Electrolysis Cells

Intensive efforts have been done to investigate the secondary phases formed during degradation [9, 46–49]. Bath components (mainly NaF and cryolite) and sodium are the two important degradation agents. Attack by the bath components was considered more important for the degradation of the refractory lining in most of the previous investigations, while the importance of sodium attack has been stressed in a recent paper by Schøning and Grande [10]. Degradation by pure NaF attack is also called "wet attack" and attacked by pure Na is called "dry attack". The reactions of both dry and wet attack have been summarized in literatures with the support by thermodynamic calculations [50–52]. These calculations showed good agreement with the autopsy findings. In principle, the qualitative understanding of the degradation reactions and the formation of the secondary phase in the refractory lining are satisfied by both thermodynamic calculations and autopsies of shut down cells.

The secondary phases in the reacted refractories can be different from cell to cell, but mainly contain albite (preferably as glass), nepheline, sodium fluoride, β-Al_2O_3 and silicon.

In a shutdown cell, there is always a sharp interface which divides the refractory lining into a reacted part and an intact part. The interface is referred to as the so-called reaction front. At the position close to the reaction front large amount of nepheline ($NaAlSiO_4$) and glassy phase (believed to be albite $NaAlSi_3O_8$) were found, while $\beta-Al_2O_3$ was often found at the top part in the reacted region. This silica rich melt phase towards the reaction front is a highly viscous liquid under the operation condition and can act as a diffusion barrier and strongly retard further Na/NaF infiltration and reaction. Since the barrier consists mainly of sodium-aluminosilicates (Na_2O-Al_2O_3-SiO_2) it is assumed to have a glass like structure. XRD analysis also shows large amount of amorphous phase in the glassy part of the autopsy samples [53, 54]. High silica content will enhance the formation of this glassy barrier [9]. Tan [55] estimated recently the molten fraction, composition of the molten silicate and viscosity of this viscous barrier according to an analysis of an autopsy sample and an analysis of mass balance and chemical reactions. In addition, a significant drop in sodium concentration is observed close to the refraction front, while no fluorine was present at the front. This implies that sodium diffuse faster than NaF [51, 53]. However, the analysis of the autopsy samples might not represent the real situation during the operation because of a reversed heat history during cooling after the cell shuts down [54].

2.3 Sodium Diffusivity in Cathode Lining

2.3.1 Formation of Sodium

Sodium is produced at the carbon cathode surface by chemical Reaction 2.2

$$\frac{1}{3}Al(l) + NaF(\text{in cryolite}) \quad = \quad Na(\text{in C}) + \frac{1}{3}AlF_3(\text{in cryolite}) \quad (2.2)$$

when liquid aluminium, bath and carbon cathode are in contact. Sodium may also be produced by cathodic Reaction 2.3

$$Na^+ + e = Na(\text{in Al}) \quad (2.3)$$

The deposition potential of pure sodium (or saturated Na alloy) is 1.44V, which is higher than that of aluminium (1.20V). Usually sodium does not deposit at the cathode during aluminium electrolysis process. However, the deposition potential will decrease with the decreasing activity of sodium [56]. The low activity of sodium (a_{N_a}) at the early stage of start up leads to a low enough deposition potential. It is suggested that at the early stage of the start up, Reaction 2.3 is the main reason for sodium deposition and penetration afterwards. With the operation going on, the activity of sodium in liquid aluminium builds up gradually, and sodium deposition potential goes up until it becomes higher than that of aluminium. Then Reaction 2.2 becomes the main source for sodium metal. Sodium uptakes in carbon slow down considerably when a metal pad is formed [57].

The Gibb's energy of Reaction 2.2 is positive (ΔG°_{1233K}=68.0kJ/mol). Na is stabilized, however, by the bonding to the carbon either by adsorption or as a defined sodium intercalation compound (Na-GIC) [3]. The bonding would favor the reaction from left to the right.

2.3.2 Sodium Diffusion in the Carbon Cathode

Sodium binary and some ternary intercalation compounds with carbon were summarized in a recent review [58]. In less ordered carbon materials sodium is adsorbed/absorbed between the graphene layers and in micro-pores. The absorption decreases with increasing temperature and crystallinity of the less ordered carbons [59]. The amount of sodium uptakes in amorphous carbon is higher than in graphite. Saturation concentration of sodium in different carbon cathode materials was measured by Lossius et *al.* and summarized in Table 2.3 [60].

"GCA" refers to gas or kiln anthracite plus 30 wt% graphite filler blocks, baked to 1200°C. "ECA" refers to electrocalcined anthracite, partly graphitized, plus 30 wt% graphite filler, blocks baked to 1200°C. "SG" refers to semigraphitic carbon, all aggregate graphitized, baked to 1200°C. "SGZ" refers to semigraphitized carbon, graphitizable filler, whole blocks calcined above 2300°C.

Table 2.3: Density, apparent porosity and sodium saturation level in different industrial carbon materials [60].

Material	**Virgin Density** [kg/m^3]	**Virgin Porosity** [vol%]	**Na Saturation** [wt%]	**Na Saturation** [kg/m^3]
GCA	1530 to 1550	16 to 19	4	60 to 70
ECA	1540 to 1550	16 to 20	4	60 to 70
SG	1590 to 1650	19 to 23	2	30 to 35
SGZ	1620 to 1650	23 to 26	1	15 to 20

The mechanism of the sodium penetration into carbon is not clear. There are two main mechanisms to describe the transport of sodium in carbon cathodes. A vapour diffusion mechanism was suggested by Dell [61] because sodium is above its boiling point at the carbon surface. Dewing [62] argued for a lattice diffusion mechanism which had been supported by other authors [63, 64]. An overview of reported diffusion coefficients for sodium in cathode materials was given by Zolochevsky **et** *al.* [65]. The reported values were rather large for lattice diffusion. Ratvik **et** *al.* [17] also reported diffusion coefficients determined from a modified Rapoport test of different carbon materials at different current density. Some of the reported data are summarized in Table 2.4.

Generally the diffusion coefficients reported are difficult to compare since many factors will influence the measurement. Increasing current density (CD) and temperature will increase the diffusivity. Data in Table 2.4 suggest that at the same CD, temperature, CR ratio[3], the diffusivity is faster in more graphitic materials. The ranking of the sodium diffusivity in different type of carbon materials is likely as follows:

Graphitized > Graphitic > Semigraphitized > Semigraphitic > Amorphous

[3]Cryolite ratio, the molar ratio of NaF and AlF_3 [2].

Table 2.4: Diffusivity of sodium in different carbon materials at different current density, bath ratio and temperature, unit [$10^{-8}m^2/s$].

Temp. [°C]	**Current Density** [A/cm^2]	**CR ratio**	**Amorphous**	**Semi-** Graphitic	**Semi-** Graphitized	**Graphitic**	**Graphitized**	**Graphite**	**Ref.**
	0.05	4	0.4			0.8	2.0		
	0.05	4	0.2			1.0	19		
	0.7	4	2.5			4.6	24	14	
980	0.7	4	3.5			5.3	47	22	[17]
	0.7	4	2.1			8.4	16		
	1	4	4.2			5.7		5.9	
	1	4	4.6			5.5		14	
980	0.98		0.4						[66]
	0.7				5				
980	0.2				2				[59]
	0.06				0.8				
	0.7	4		3.99					
980	0.2	4		1.86					[65]
	0.06	4		1.21					
970	0.7	2.2		0.05-0.12					[67]
920	0.7	2.2		0.04-0.08					

2.3.3 Sodium Diffusion in the Refractory Lining

Diffusion of sodium is assumed to be faster than the bath component in the refractory layer [51, 53]. The diffusivity of sodium in the sodium alumino-silicate viscous diffusion barrier near the reaction front is important to know for predicting the degradation time scale in the refractory layer or say the penetration depth as a function of time. Sodium diffusivity data in the specific material is not available. However, it can be estimated by several ways based on the available material properties and measurements.

In general, the diffusivity in a viscous liquid can be determined based on the available viscosity data using Stokes-Einstein relation as Equation (2.4)

$$D_\eta = \frac{k_B}{6\pi r}\frac{T}{\eta} \tag{2.4}$$

where D_η is the viscosity diffusivity [m^2s^{-1}], k_B is the Boltzmann constant [JK^{-1}], η is the fluid viscosity [Pa·s], T is the temperature [K] and r is the radius of the diffusing species [m]. Alternatively Eyring relation

$$D_\eta = \frac{k_B}{\lambda}\frac{T}{\eta} \tag{2.5}$$

can be used, where λ is the translation distance of the diffusing ion [m].

Viscosity data for some compositions in the Na_2O-Al_2O_3-SiO_2 system which is relevant to the viscous diffusion barrier in the reacted refractories are available [68, 69]. The temperature dependent viscosity was described by the three-parameter Vogel-Fulcher-Tammann Equation (2.6)

$$log_{10}\eta = A_{TVF} + \frac{B_{TVF}}{T - C_{TVF}} \tag{2.6}$$

where η is the fluid viscosity [Pa·s], T is the temperature [K], and A_{TVF}, B_{TVF}, C_{TVF} are constants, or described by the Arrhenius Equation (2.7)

$$log_{10}\eta = -A + \frac{B}{T} \tag{2.7}$$

where A and B are constants.

According to the composition and appearance of the viscous diffusion barrier in the refractory layer, it is assumed to have a glass like structure. It is well established that the mobility of the alkali cations is significantly higher than the glass former cations in such melts [70].

In the Na_2O-Al_2O_3-SiO_2 glass structure, SiO_2 is a network former, Na_2O is a network modifier and Al_2O_3 is a conditional oxide [70]. Network former cations and oxygen atoms are connected irregularly by strong covalent bonds to form a three-dimensional network. In a glass with only network former oxides, all O^{2-} occurs as bringing oxygen with the neighbor cations. The addition of network modifier oxides (can be alkali or earth alkali oxides) reduces the number of the stable bridges in the glass network by introducing nonbridging oxygen adjacent to the modifier cations. The bonds between nonbringing oxygen and alkali ions are ionic bond. It weakens the glass structure and results in the change in the physical properties. Conditional oxides do not form glass but in combination with other oxides, they become a part of the covalent network. A schematic drawing of the glass network is shown in Figure 2.9 [71].

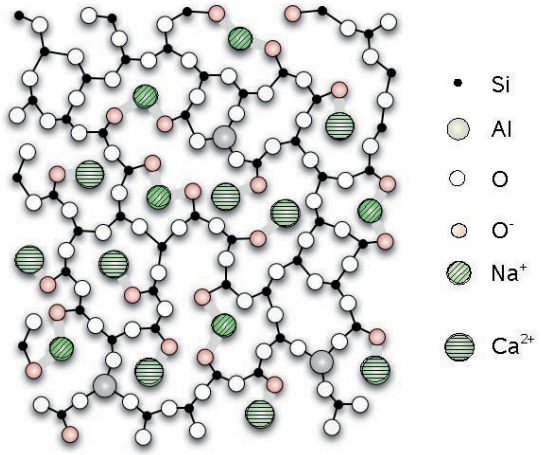

Figure 2.9: A schematic drawing of the glass net work [71].

Due to the nature of the ionic bonds, Na^+ has much higher mobility or say easy to decouple from the structure than other cations Si^{4+} and Al^{3+} who are sitting in the covalent bonds network. The differences between the diffusion of alkalis, alkaline-earths, and network former cations are not anomalous and have been observed repeatedly in diffusion studies on compositions relevant to geochemistry [72, 73]. The diffusivity of one element in a multi-component material can be measured by tracer diffusion. A comparison of tracer diffusion of different ions in basalt melt (CaO-Al_2O_3-SiO_2), albite melt ($NaAlSi_3O_8$), orthoclase melt ($KAlSi_3O_8$) and SiO_2 melt is shown in Figure 2.10.

As can be seen from Figure 2.10, the diffusivity of Si (network former) follows the

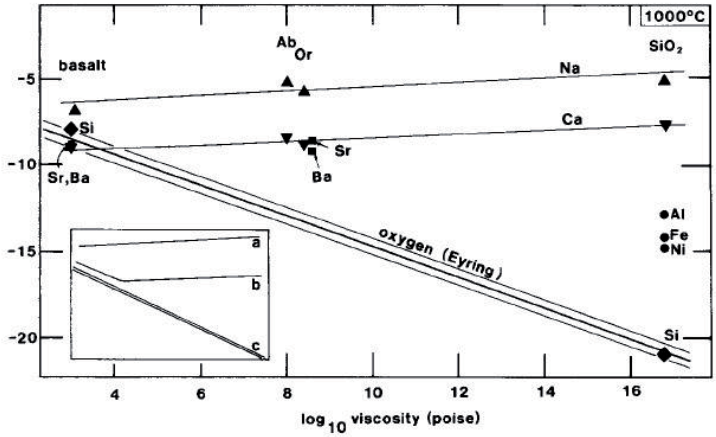

Figure 2.10: Tracer diffusivity data [cm^2/s] vs melt viscosity for basalt, a Ca-Al-Si synthetic oxide melt, albite ($NaAlSi_3O_8$) and orthoclase melts ($KAlSi_3O_8$), and SiO_2 melt at 1000°C [73]. "Ab" represents albite and "Or" represents orthoclase.

Eyring relation Equation (2.5) or say viscous diffusivity. It reduces dramatically with increasing viscosity. Diffusivity of Na (network modifier), on the contrary, is virtually independent of the melt viscosity or melt composition. At the albite composition, the Na diffusivity is close to 1×10^{-9} m^2/s which is around 7-8 orders magnitude higher than the Si diffusivity or viscous diffusivity. The higher diffusion coefficients of Na compared with viscous diffusivity were also confirmed by other authors [74–77]. Moreover, the diffusivity of Na is found close to the conductive diffusivity which is estimated by the Nernst-Einstein Equation (2.8)

$$D_\eta = \frac{\sigma_{dc} k_B T}{q^2 N} \tag{2.8}$$

where q is the charge, σ_{dc} is the DC ionic conductivity [$\Omega^{-1}cm^{-1}$] and N is the number density of Na^+ ions [ions·m^{-3}].

Sodium diffusivity in the Na_2O-Al_2O_3-SiO_2 system can be found in literature [77–80]. Some of the compositions are marked as filled polygons in the Na_2O-Al_2O_3-SiO_2 ternary phase diagram shown in Figure 2.11. Bold line is the sodium attacking path of the refractory materials. The open circle on the bold line is the composition found in a spent pot lining (SPL) with the age of 300 days [53].

The measured diffusivity is temperature dependent following Arrhenius relation-

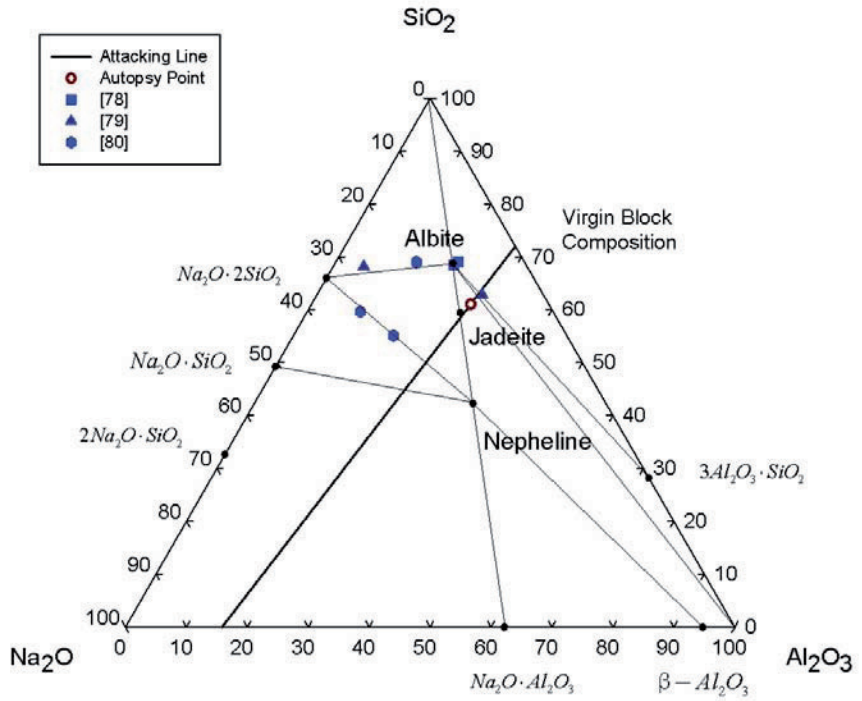

Figure 2.11: Compositions where Na diffusivity data are available. Bold line is the sodium attacking path of the refractory materials. The open circle on the bold line is the composition found in a spent pot lining (SPL) with the age of 300 days [53].

ship as Equation (2.9)

$$D = D_0 exp(-\frac{Q}{RT}) \tag{2.9}$$

where D_0 is pre-exponential factor [m^2/s], Q is activation energy [J/mol], R is gas constant 8.314 [J/(K·mol)] and T is temperature [K].

Pre-exponential factor (D_0) and activation energy (Q) for the 3 compositions close to those found by autopsy of SPL are listed in Table 2.5 [78, 79].

Table 2.5: Arrhenius pre-exponential factor (D_0) and activation energy (Q) for viscous flow of some oxide systems.

	Na_2O [wt%]	**Al_2O_3** [wt%]	**SiO_2** [wt%]	**D_0** [cm^2/s]	**Q** [kcal/mole]	**Temp. Range** [°C]	**Ref.**
1	10.9	18.0	70.6	5.02×10^{-4}	14.5±0.3	352-716	[79]
2	10.9	20.44	69	5.3×10^{-3}	13.5±3	350-795	[78]
3	11.9	19.5	68.4				

The diffusivity of F^- is found much slower than that of the single valence cation like Na^+ in obsidian – a volcano glass (70-75 wt% SiO_2, plus MgO and Fe_3O_4) as shown in Figure 2.12 [81]. At 1000 K the diffusivity of F^- was around 5 orders of magnitude lower than Na^+. The reason for that is probably due to the diffusion of F^- might involve the replacement of the strong network structure. The slower diffusivity of F^- implies that Na may infiltrate faster than NaF in the viscous glassy diffusion barrier in the refractory layer.

2.3.4 Sodium Diffusion in the Sidewall Blocks

The diffusion of sodium in the sidewall blocks was proposed to be gas phase diffusion in the Author's diploma work [19] due to the high temperature of the sidewall block in the cells and the high equilibrium vapour pressure of the sodium. The diffusivity of sodium in nitrogen gas at 773 K was estimated to be 7×10^{-5} m^2/s based on the kinetic gas theory, Chapman-Enskog theory and Knudsen model. The effective diffusion coefficient (D_{eff}) depends on the porosity (ϵ) and tortuosity (τ) of the real material and is determined by Equation (2.10)

$$D_{eff} = D_0 \times \frac{\epsilon}{\tau} \tag{2.10}$$

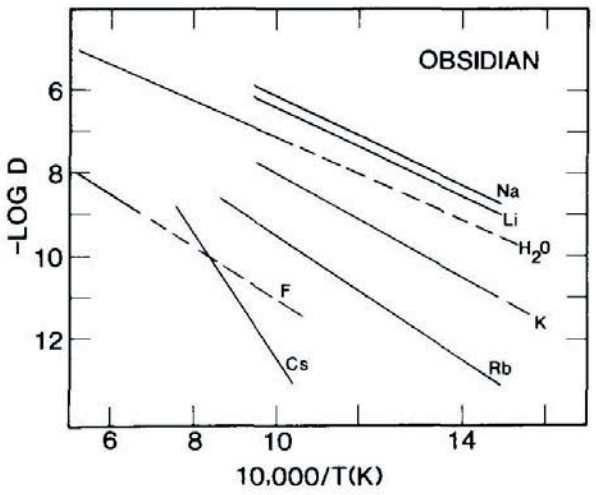

Figure 2.12: Comparison of the chemical diffusivities of fluorine in albite melt and water in obsidian/rhyolite melt with tracer diffusivities of alkalies in obsidian melt [81].

The apparent porosity of the Si_3N_4-bonded SiC sidewall block is around 15%. The tortuosity is not measured in the present work, but normally porosity and tortuosity will lower the diffusivity by 1 or 2 orders of magnitude. Hence, 10^{-7} m^2/s could be a good assumption of the diffusivity of the sodium in the sidewall block.

Chapter 3

Computational Methods for Heat and Mass Transfer

3.1 Thermal Conductivity of Porous Composite Materials

The thermal conductivity of the Si_3N_4-bonded SiC sidewall block is one of the key issues in the present research work. The material consists of coarse SiC grains (mm scale) and a fine grained (μm scale) porous binder, which is a porous material with several solid phases.

Effective thermal conductivity of a composite porous material is known to depend on many factors including phase composition, porosity and microstructure. Numerous theoretical and empirical correlations have been proposed to predicate the effective thermal conductivity of composite and porous materials, such as Series Model, Parallel Model, Geometric Mean Model, Bruggeman Theoretical Model, Maxwell Theoretical Model, Hamilton and Crosser Semi-Theoretical Model, Ratcliffe Empirical Model, etc. Progelhop et *al* [82] have provided an excellent review of these numeric and empirical models and their limitations. However, no single approach can accurately predict the thermal conductivity of all types of composites.

Effective thermal conductivity of an arbitrary two phase composite calculated by different models is shown in Figure 3.1, in which the higher thermal conductivity phase is the continuous phase and the lower thermal conductivity phase is the dis-

crete phase for Bruggeman, Maxwell and "Effective Medium Percolation Theory" (EMPT) model (details of each model will be discussed later in this section). The difference in thermal conductivity of the two phases is 100 W/(m·K). The results calculated by different models have no significant difference.

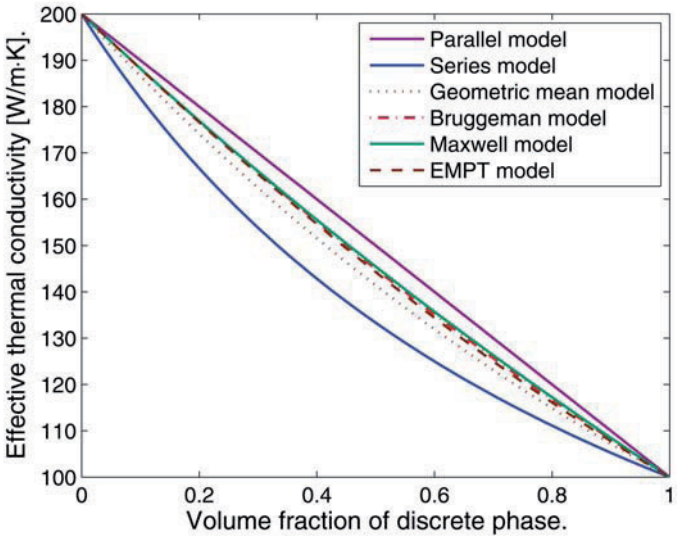

Figure 3.1: Effective thermal conductivity of two phase composite (k_1=100 W/(m·K), k_2=200 W/(m·K)) calculated by different models. Lower thermal conductivity phase is the discrete phase.

In general, the Parallel model (Equation (3.1)) and Series model (Equation (3.2)) can be use as the upper and lower limit of the effective thermal conductivity of the composites

$$k_{eff} = k_1 V_1 + k_2 V_2 \tag{3.1}$$

$$\frac{1}{k_{eff}} = \frac{V_1}{k_1} + \frac{V_2}{k_2} \tag{3.2}$$

where k_{eff} is the effective thermal conductivity of the composite material. k_1, k_2 are the thermal conductivity of the two materials, and V_1, V_2 are the volume fraction of the two materials (based on the relative cross-sectional areas). A schematic drawing of a parallel model and a series model is shown in Figure 3.2.

For a dense solid composite, the estimation by this upper and lower limit describe well the measured thermal conductivity of such composites. However, if one

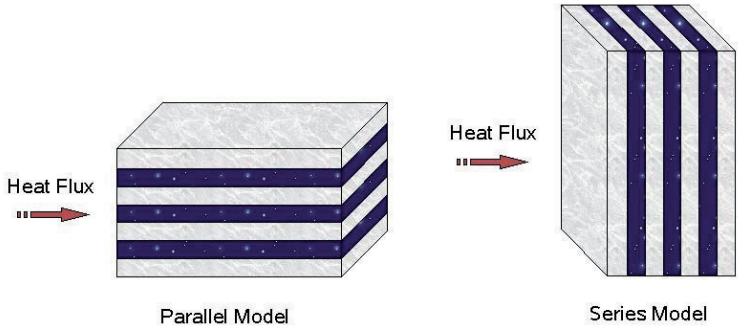

Figure 3.2: A schematic drawing of Parallel and Series Model.

phase is air, the effective thermal conductivity calculated by these different models will vary significantly, but will still have problems to account for measured data (See Figure 3.3).

For a porous material consisting of several solid phases like the Si_3N_4-bonded SiC sidewall block, one single model is inapplicable. Several models need to be combined together to describe its effective thermal conductivity.

The Maxwell theoretical model [83] is used in this work for predicting the properties of solid-solid composite material, where randomly distributed SiC grains are embedded in a homogeneous binder phase of porous Si_3N_4. The thermal conductivity is given as Equation (3.3)

$$k_e = k_c \frac{k_d + 2k_c + 2\phi(k_d - k_c)}{k_d + 2k_c - \phi(k_d - k_c)} \tag{3.3}$$

where k_e is effective thermal conductivity of the composite materials [W/(mK)], k_c is thermal conductivity of the continuous binder phase [W/(mK)], k_d is thermal conductivity of the distributed SiC phase [W/(mK)] and ϕ is volume fraction of the discrete phase.

The nitride binder phase is not phase pure, but contains both α-Si_3N_4 and β-Si_3N_4 and is highly porous. For the mixture of the two nitride phases, geometric mean method is applied, as defined by Equation (3.4) [84]

$$k_e = k_\alpha^{\phi_\alpha} k_\beta^{\phi_\beta} \tag{3.4}$$

where k_α, k_β and ϕ_α, ϕ_β are the thermal conductivity and volume fraction of α-Si_3N_4 and β-Si_3N_4 respectively. The geometric mean method is chosen here

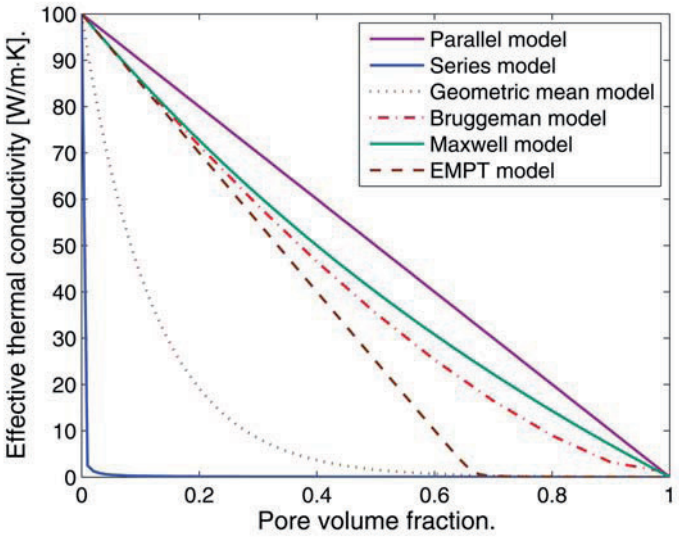

Figure 3.3: Effective thermal conductivity of two phase composite calculated by different models in which one phase is air (k=0.026 W/(m·K)). The thermal conductivity of the other phase is 100 W/(m·K).

because α-Si_3N_4 and β-Si_3N_4 are mixed in such a way that it can not be distinguished by a continuous and a discrete phase.

The "Effective Medium Percolation Theory" (EMPT) [85] is used to describe the thermal conductivity of the porous binder as Equation (3.5)

$$\begin{aligned} k_e &= \frac{1}{4}[k_p(3v_p-1)+k_s(3v_s-1) \\ &+ ([k_p(3v_p-1)+k_s(3v_s-1)]^2+8k_pk_s)^{1/2}] \end{aligned} \tag{3.5}$$

where k_p and v_p are the thermal conductivity and the volume fraction of air and k_s and v_s are the thermal conductivity and the volume fraction of the solid nitride mixture respectively. An increase in the porosity will decrease the effective thermal conductivity of the composite material.

For highly porous materials, like the binder in Si_3N_4-bonded SiC, porosity alone is not sufficient to characterize a composite material. Other microstructure related factors such as pore shape, distribution, connectivity and orientation with respect to heat flux are equally important. The factor is defined in a modified Bruggeman

model [86, 87] as Equation (3.6)

$$\frac{k_e}{k_s} = (1 - v_p)^X \tag{3.6}$$

where *X* is defined by Equation (3.7)

$$X = \frac{1 - cos^2\alpha}{1 - F} + \frac{cos^2\alpha}{2F} \tag{3.7}$$

where *F* is the shape factor of pores and α is the angle between the revolution axis and heat flux. Large amount of elongated pores aligned perpendicular to the heat flux direction results in large *X* factor. With increasing *X* factor the effective thermal conductivity of the composite is reduced.

For non-metallic crystalline solids like ceramics at low and medium temperatures, heat is conducted by lattice vibrations (phonon). Grain boundaries in polycrystalline material will then act as scattering sites and, hence decrease the thermal conductivity. It can be described as the so-called interfacial thermal resistance [88–90], expressed by Equation (3.8)

$$\begin{aligned} \frac{1}{k_{\text{poly crystal}}} &= \frac{1}{k_{\text{single crystal}}} + nR_{int} \\ &= aT + nR_{int} \end{aligned} \tag{3.8}$$

where *n* is the number of grain boundaries per unit length [m^{-1}], and R_{int} is the average interfacial thermal resistance of a grain boundary [m^2KW^{-1}].

According to the above equation, the grain boundary resistance (nR_{int}) can be obtained by extrapolating the inverse thermal conductivity (k^{-1}) versus absolute temperature (K). The interception with the axis at T = 0 K is expected to be the grain boundary resistance. Thermal conductivity of the polycrystalline materials will be reduced with increasing grain boundary resistance and the grain boundary resistance increases with the reduction of grain size (see Figure 3.4). Therefore when the grain size is considerable small, like the nitride grains in the present materials, grain boundary resistance is necessary to be considered.

3.2 Finite Element Method Based Computer Simulation

3.2.1 Finite Element Method

Physical phenomena such as structural mechanics, heat transfer, diffusion, fluid dynamics etc can be described by differential equations, and usually the problem

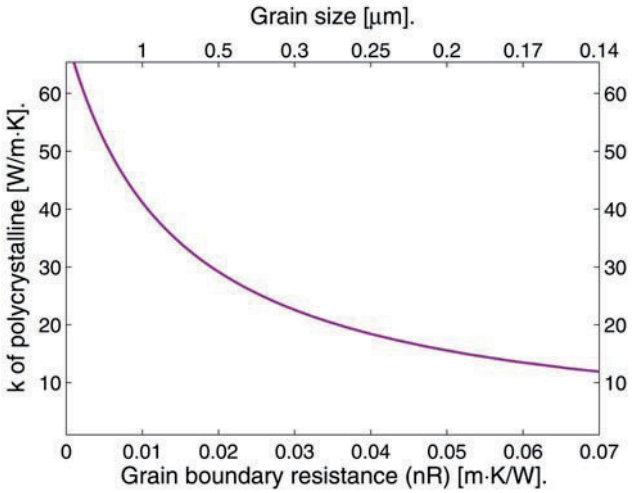

Figure 3.4: Thermal conductivity of polycrystalline materials as a function of grain boundary resistance and grain size. In the calculation, the average grain boundary resistance of 10^{-8} [m^2KW^{-1}] have been used.

is too complicated to be solved by classical analytical methods. The "finite element method" (FEM) is a numerical approach by which differential equations can be solved in an approximate manner.

The term "finite element" was first used by Clough in 1960. Since its inception, the literature on finite element applications has grown exponentially. FEM is, nowadays, a widely used method in solving "partial differential equations" (PDEs) and a powerful numeric technique to evaluate complex chemical and physical processes.

In brief, FEM is a computational method that subdivides an object into very small but finite-size elements [91]. The physics of one element is approximately described by a finite number of unknowns, i.e. "degrees of freedom "(d.o.f.). Each element is assigned a set of characteristic equations (describing physical properties, boundary conditions and imposed forces), which are then solved as a set of simultaneous equations to predict the object's behavior. A system with a finite number of unknowns is called a "discrete system" in contrast to the original continuous system with an infinite number of unknowns. This method is characterized by three features [92]:

- The domain of the problem is represented by a collection of simple subdomains, called finite elements. The collection of finite elements is called the finite element mesh
- Over each finite element, the physical process is approximated by functions of desired type (polynomials or otherwise), and algebraic equations relating physical quantities at selective points, called nodes, of the element are developed
- The element equations are assembled using continuity and/or balance of physical quantities

In the finite element method, in general, we seek an approximate solution u to a PDE in the form of Equation (3.9)

$$u \approx \sum_{j=1}^{n} u_j \varphi_j + \sum_{j=1}^{m} c_j \phi_j \tag{3.9}$$

where u_j are the values of u at the element nodes, φ_j are the interpolation functions, c_j are the nodeless coefficients, and ϕ_j are the associated approximation function.

A real system often involves thousands of unknowns which can not be solved by hands. Therefore, the FEM relies on the efficient computer and modeling software.

In the present research work, all the simulations have been performed by using COMSOL Multiphysics® 3.5a, which is a commercial modeling software based on FEM [93].

3.2.2 Heat Transfer

Heat transfer by conduction is governed by Fourier's law. In 3-dimension, the partial differential equation (PDE) is expressed as Equation (3.10)

$$\rho C_p \frac{\partial T}{\partial t} + \nabla \cdot (-k \nabla T) = Q \tag{3.10}$$

where ρ is density [kg/m^3], C_p is heat capacity [J/(kg·K)], t is time [s], and Q is heat source [W/m^3].

To solve the PDE and investigate the effective thermal conductivity of the composite material, computer simulation based on finite element method is used in this

work. By this way, the effective thermal conductivity of the composite material can be obtained by Equation (3.11) after solving the heat flux ($\mathbf{q}$) by simulation

$$\mathbf{q} = -k\nabla T \tag{3.11}$$

When a thin layer of a material with considerable low thermal conductivity is formed in between two phases in the structure, like sodium silicates layer on SiC grain and Si_3N_4 particles as shown later in Figure 6.11(c) (Page 72), the thin thermal insulating layer mode can be used to predict the effective thermal conductivity. In this mode, two separate but symmetric heat flux boundary conditions are set according to Equation (3.12)

$$\begin{aligned} \mathbf{q}_{down} &= -\mathbf{n}_{down} \cdot (-k\nabla T)_{down} = \frac{k_{res}}{d_{res}}(T_{up} - T_{down}) \quad \text{on } \partial\Omega_{down} \\ \mathbf{q}_{up} &= -\mathbf{n}_{up} \cdot (-k\nabla T)_{up} = \frac{k_{res}}{d_{res}}(T_{up} - T_{down}) \quad \text{on } \partial\Omega_{up} \end{aligned} \tag{3.12}$$

The two boundaries together making up the thin thermal insulating layer here referred to as "up" and "down". $\boldsymbol{n}$ is the normal on the boundary, k_{res} is the thermal conductivity of the thermal insulating layer, d_{res} is the thickness of the layer and Ω represents the boundary.

There is a local temperature drop across the thin thermal insulating layer which is illustrated in Figure 3.5.

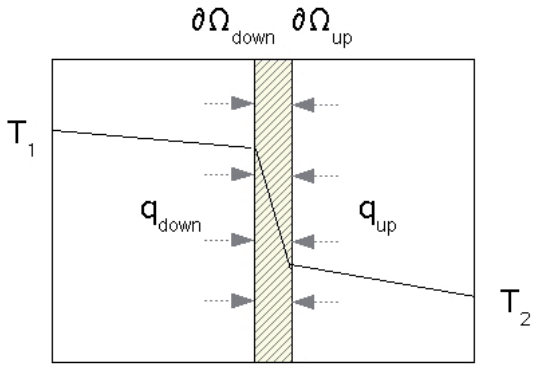

Figure 3.5: A schematic drawing showing an enlarged thermal insulating layer formed between two grains.

3.2.3 Diffusion and Reaction

The governing equation for the diffusion and reaction model is expressed as Equation (3.13) based on Fick's 2nd law

$$\frac{\partial c_i}{\partial t} + \nabla \cdot (D_i \nabla c_i) + R = 0 \tag{3.13}$$

where c_i is the concentration of diffusion species [mol/m^3]. Two degradation agents are considered in this work: sodium and oxidizing gas. R is the reaction rate [mol/(m^3·s)]. D_i is the diffusivity of each species. Besides diffusion coefficients, the reaction rate R in different lining materials varies based on different degradation schemes.

3.2.4 Fluid Flow in Porous Media

Darcy's law is a phenomologically derived constitutive equation that describes the flow of a fluid through a porous medium, which is a simple proportional relationship between the instantaneous discharge rate through a porous medium, the viscosity of the fluid and pressure drop over a given distance. In this case, the flow through porous media is driven by the pressure gradient. The partial differential equation is expressed as Equation (3.14)

$$\frac{\partial(\rho\epsilon)}{\partial t} + \nabla \cdot (\rho(-\frac{\kappa}{\eta})\nabla p) = \mathbf{F} \tag{3.14}$$

where ρ is density [kg/m^3], κ is permeability [m^2], η is dynamic viscosity [Pa·s], ϵ is porosity, and $\boldsymbol{F}$ is body force [kg/(m^{3}s)].

When pressure is determined, COMSOL Multi-physics® solver calculates the superficial velocity $\boldsymbol{U}$ as Equation (3.15) [93]

$$\mathbf{U} = -\frac{\kappa}{\eta}\nabla p \tag{3.15}$$

which is the flux of fluid across a unit area but not the actual velocity of the fluid.

The linear velocity $\boldsymbol{u}$ is then defined from the superficial velocity as expression (3.16)

$$\mathbf{u} = \frac{\mathbf{U}}{\epsilon} \tag{3.16}$$

3.2.5 Two-phase Flow in Capillary Pores

Bath flow in pores is a two-phase flow, the flow speed can be estimated by using Navier-Stokes equations combined with phase field mode in COMSOL Multiphysics®. In the simulation, bath/air interface moving along the pore walls over time can be traced and the moving rate can be derived accordingly.

Navier-Stokes equations describe the momentum transport as Equation (3.17)

$$\begin{aligned} \rho\frac{\partial \mathbf{u}}{\partial t} + \rho(\mathbf{u}\cdot\nabla)\mathbf{u} &= \nabla\cdot[-p\mathbf{I} + \eta(\nabla\mathbf{u} + (\nabla\mathbf{u})^T)] + \mathbf{F}_{st} + \rho\mathbf{g} \\ \nabla\cdot\mathbf{u} &= 0 \end{aligned} \tag{3.17}$$

where **u** is the fluid velocity [m/s], F_{st} is the volume force which is the surface tension force acting at the air/bath interface, p is the pressure [Pa · s], and η is the dynamic viscosity [Nm/s^2]. Surface tension and conservation of mass are considered.

The phase field mode uses a Cahn-Hilliard equation, including a chemical potential to represent a diffuse interface separating the two phase. The equation tracks a diffuse interface separating the immiscible phases. The diffuse interface is defined as the region where the dimensionless phase field variable ϕ goes from -1 to 1. The Cahn-Hilliard equation breaks up into two equations as Equation (3.18) and (3.19) in the simulation

$$\frac{\partial\phi}{\partial t} + \mathbf{u}\cdot\nabla\phi = \nabla\cdot\frac{\xi\lambda}{h^2}\nabla\varphi \tag{3.18}$$

$$\varphi = -\nabla\cdot h^2\nabla\phi + (\phi^2 - 1)\phi \tag{3.19}$$

where ξ is the mobility [m^{3}s/kg], λ is the mixing energy density [N], h is the interface thickness parameter [m], and φ is the phase field help variable.

The following equation relates mixing energy density and the interface thickness to the surface tension coefficient (γ)

$$\gamma = \frac{2\sqrt{2}}{3}\frac{\lambda}{h} \tag{3.20}$$

Chapter 4

Experimental

4.1 Materials

Virgin Si_3N_4-bonded SiC sidewall blocks from different suppliers and spent blocks with different lifetime collected from four autopsies were used to study the chemical stability and the thermal properties of the sidewall blocks. The phase content, apparent porosity and density of the materials from the suppliers' specification are listed in Table 4.1. Virgin blocks were Block A, Block B, Block C and Block D. Block A and Block B are from the same supplier with different thickness. The service lifetime for the four spent blocks was 270 days, 604 days, 1569 days and 1767 days respectively.

Table 4.1: The phase content, apparent porosity and density of the materials.

Block Name	**SiC** [wt%]	**Si_3N_4** [wt%]	**App. Porosity** [vol%]	**Bulk Density** [kg/m^3]
Block A	75	20	15.5	2680
Block B	75	20	15.5	2680
Block C	75	22	14.8	2700
Block D	78	18	17	2650

An overview of the difference characterization techniques applied for each block are summarized in Table 4.2.

Table 4.2: An Overview of the Methods to Characterize the Virgin and Spent Blocks. [1]: Focus on the homogeneity of the virgin block, [2]: Focus on the chemical stability of the blocks, [3]: Focus on the thermal properties of the blocks.

Test Method	Block A[1,3]	Block B[3]	Block C[3]	Block D[3]	270 days[2]	604 days[2]	1569 days[2]	1767 days[2,3]
XRD	X	X	X	X	X	X	X	X
LECO	X				X	X	X	
Bulk Density & App. Porosity	X	X	X	X	X	X	X	X
Pore Size Distribution		X						X
SEM	X	X	X	X	X	X	X	X
TEM		X						X
Therm. Expansion		X						X
Therm. Conductivity	X	X	X	X				X

4.2 Sampling

4.2.1 Homogeneity and Chemical Stability

In order to investigate the homogeneity of the virgin block, samples were cut by using a diamond saw from Block A, a Si_3N_4-bonded SiC sidewall block according to the overview shown in Figure 4.1. As can be seen from the cross section of a virgin block shown in Figure 4.2, the area closed to the block surface has lighter color than the center area, therefore samples from both the interior and surface of the block were taken.

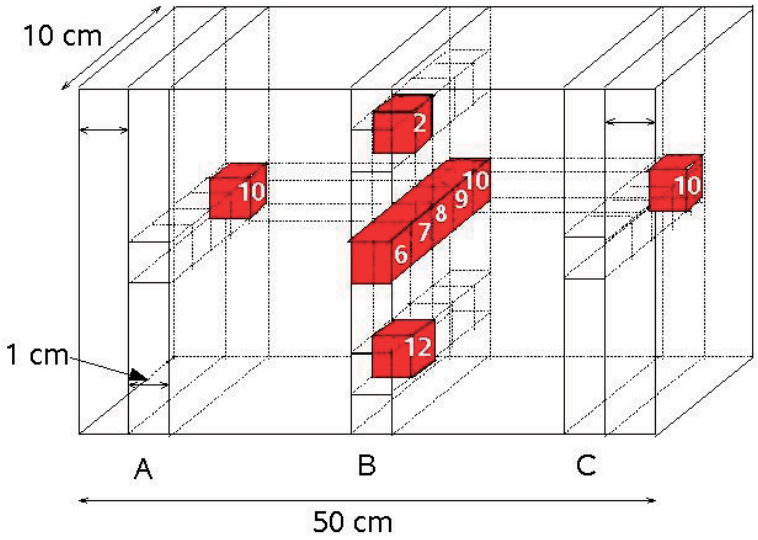

Figure 4.1: The relative positions of the samples used for investigation of the homogeneity of the block. A10, B6, B10, C10 are from peripheral area, and others are from central part (not in scale).

Four different spent sidewall blocks with different ages have been analyzed. The cross section of the spent sidewall block is shown in Figure 4.3.

For convenience the spent sidewall block is divided into two regions the "gas zone" and the "electrolyte zone" defined by the level of the molten electrolyte in the electrolysis cell. The two regions correspond to the two parts of the sidewall block above and under the electrolyte bath level. The darker area in the "electrolyte zone" is labeled "infiltration area". Samples were cut by using a diamond saw, both the electrolyte zone and the gas zone of the blocks as shown in Figure

Figure 4.2: The cross section of virgin Block A. The area closed to the block surface has lighter color than the center area.

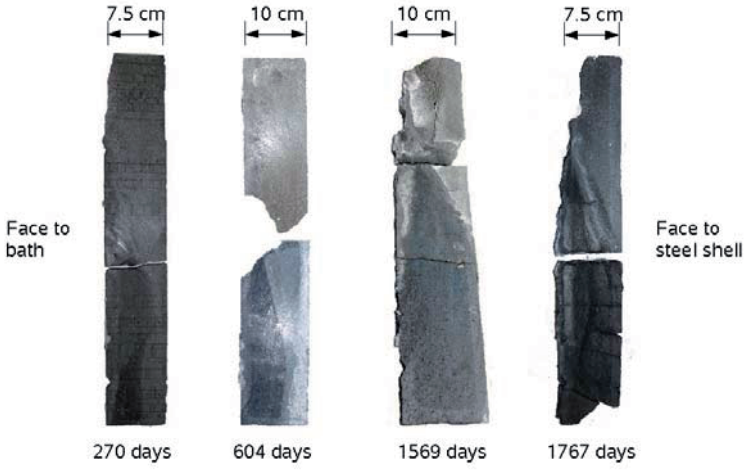

Figure 4.3: The cross section of the spent sidewall block at the age of 270, 604, 1569 and 1767 days.

4.4.

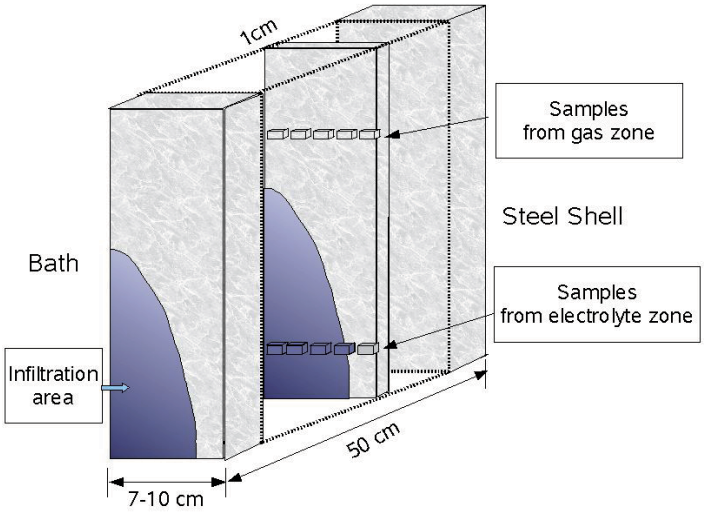

Figure 4.4: The sampling position in the spent sidewall block (not in scale).

4.2.2 Thermal Properties

The thermal conductivity of virgin and spent Si_3N_4-bonded SiC blocks were determined by the laser flash method [21]. Four virgin blocks (A, B, C and D) from different suppliers and one spent block collected during an autopsy of a cell with a lifetime of 1767 days were analyzed. Samples for the thermal conductivity measurement were cylindrical slices around 3 mm thick and 25.4 mm in diameter. Samples were taken from both the area close to the surface of the virgin blocks and from the center.

Samples from the spent block were prepared by drilling parallel to the direction of the heat flux in the cell. A schematic drawing for the sampling procedure is shown in Figure 4.5. Since the degradation of the top part (gas zone) and the bottom part (electrolyte zone) has been proposed to be different by the author [94,95], samples from both parts were analyzed. The labels of the sample are explained in Figure 4.6.

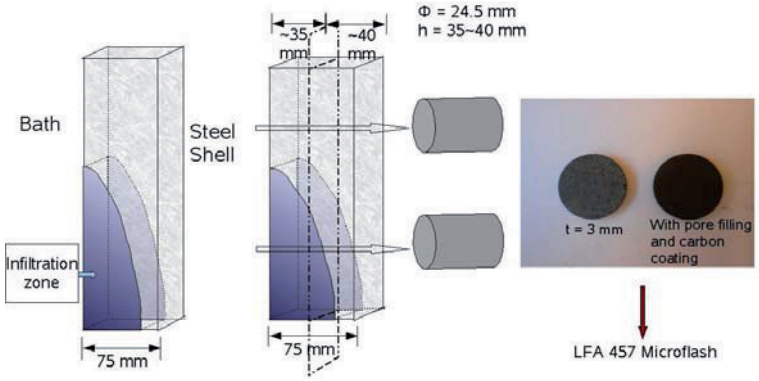

Figure 4.5: Schematic drawing showing the sampling procedure. Cylindrical samples were drilled parallel to the heat flux direction from both the gas zone and the electrolyte zone of the spent block.

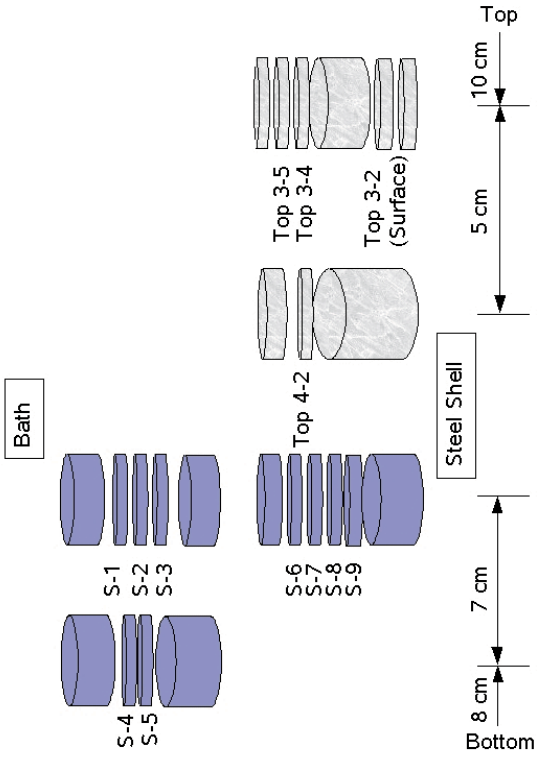

Figure 4.6: Schematic drawing showing the sample labels taken from a spent block with the age of 1767 days.

4.3 Characterization of Materials

Qualitative and Quantitative X-ray Diffraction

Powder X-ray diffraction of the samples powders (ground down to 63 μm) was performed by using a Bruker D8 Advance X-ray diffractometer with a Våntec detector and a Bruker D8 Focus X-ray diffractometer with a LynxEye detector (Bruker AXS, Karlsruhe, Germany). Data for phase identification were collected with a step size of 0.015° and a count time of 0.3 s over the 2θ range 10° to 80°.

Rietveld refinement [96, 97] of the diffractograms was performed by using the DIFFRAC^{plus} TOPAS 4.1 software[1] (Bruker AXS, Karlsruhe, Germany) to give quantitative phase composition for the phases found by qualitative analysis. Phases were identified via the Powder Diffraction File (PDF) database and confirmed via profile fitting with the DIFFRAC^{plus} TOPAS 4.1 software suite. The reference number of PDF and relevant references of the structure file used in DIFFRAC^{plus} TOPAS 4.1 for the various phases are listed in Table 4.3 [98–105]. Due to the polymorphism of SiC and the large grain size of SiC relative to the other phases, the absolute amount of the phases from the Rietveld refinement is expected to be uncertain, while the relative amount of the product phases determined by the analysis is reliable and essential for the work.

Table 4.3: References for the phase used in the Rietveld refinement.

Composition	PDF	Space Group	Reference
α-Si_3N_4	00-041-0360	P31C	[98]
β-Si_3N_4	00-033-1160	$P6_3$	[99]
Si	00-027-1402	$Fd\bar{3}m$	
SiC(3C)	01-075-0254	$F\bar{4}3m$	[100]
SiC(4H)	00-029-1127	$P6_3mc$	[100]
SiC(6H)	00-029-1131	$P6_3mc$	[100]
Si_2ON_2	01-083-1852	$Cmc2_1$	[101]
Cristobalite Low	01-076-0935	$P4_12_12$	[102]
Na_2SiO_3	00-016-0818	$Cmc2_1$	[103]
α-$Na_2Si_2O_5$	01-076-0767	Pcnb	[104]
β-$Na_2Si_2O_5$	01-076-0784	$p2_1/a$	[105]

[1] A new generation of profile and structure analysis software.

Chemical Analysis

Total oxygen and nitrogen element content in the samples were determined by LECO TC-436DR (LECO, St. Joseph, MI, USA) by using a selective hot gas extraction method. The total carbon element content was found by LECO CS230 (LECO, St. Joseph, MI, USA). Powder samples with the same size as for XRD were used for the analysis.

4.4 Density, Porosity and Microstructure

Bulk Density and Apparent Porosity

Bulk density and apparent porosity of the samples were measured according to standard ISO5017 based on Archimedes' principle. Isoproponal was used for the samples from the bottom part of the spent block to avoid the loss of water soluble phases. Distilled water was used for the samples from the virgin and the top part of the spent block.

The bulk density ρ and the apparent porosity ϵ were calculated based on Equation (4.1) and (4.2)

$$\rho = \frac{D}{W - S} \times \rho_{lig} \tag{4.1}$$

$$\epsilon = \frac{W - D}{W - S} \tag{4.2}$$

where *D* is the dry weight [g], *W* is the wet weight [g], *S* is the suspending weight in the liquid [g] and ρ_{lig} is the density of liquid [g/cm^3].

Pore Size Distribution

The mercury intrusion method was applied for the determination of the pore size distribution of the virgin and spent materials using Carlo Erba Porosimeter 2000 and Carlo Erba Macropores Unit 120 (Italy). Sample size for the measurement was 1cm$\times$1cm$\times$1cm.

Scanning Electron Microscopy

The microstructure of the materials was observed by field emission scanning electron microscopy (FE-SEM, Zeiss Ultra 55 Limited Edition, Germany), point analysis was performed by electron microprobe analysis (EMPA) using JXA-8900 Superprobe (JEOL, Tokyo, Japan), equipped with wavelength dispersive X-ray Spectrometer (WDS). All samples for SEM/EMPA analysis were collected with fracture surface to give good images of the microstructure.

Transmission Electron Microscopy

The crystal structure of the needle nitride phase in the virgin block was investigated by transmission electron microscopy (TEM, JEM-2010, Japan). The Needle samples were taken from the fractured surface by using the sharp tip of the operating knife under a light microscope.

4.5 Thermal Conductivity

The laser flash method [21] was used to determine the effective thermal conductivity *k* of the samples via thermal diffusivity measurement using Equation (4.3)

$$k(T) = \alpha(T) \times \rho(T) \times c_p(T) \tag{4.3}$$

where *k* is the thermal conductivity [W/(m·K)], α is the thermal diffusivity [m^2/s], ρ is the density [kg/m^3], and c_p is the heat capacity [J/(kg·K)].

Thermal diffusivity was measured using MicroFlashTM LFA 457 (Netzsch, Germany) in N_2 atmosphere. The temperature range for virgin materials was from 25 up to 1000°C, for the top part of the spent block from 25 to 900°C and for the bottom part of the spent block from 25 to 500°C. The heating rate was 2 K/min up to 100°C and 10 K/min from 100°C and up. To avoid any unexpected damage to the instrument, all samples were heat treated up to the determined upper limit temperature before the thermal diffusivity measurement.

Thermal conductivity was calculated by data post processing after the measurements which was performed by NETZSCH LFA Analysis, a software associated with MicroFlashTM LFA 457. Thermal expansion for the virgin and spent materials was determined by using a dilatometer (Netzsch 402E, Germany) in N_2

atmosphere with the same temperature range as thermal diffusivity measurement, from which the density of the samples as a function of temperature was obtained. $c_p(T)$ for each sample was calculated by the program by measuring the diffusivity of a alumina standard (99.8%, NETZSCH, Germany, thickness: 3.008 mm, diameter: 25.37mm) at the same conditions as for the samples.

Chapter 5

Investigation of the Virgin Sidewall Blocks

5.1 Phase Composition

The main phases found by X-ray diffraction (XRD) in the virgin Si_3N_4-SiC blocks (Block A, B[1]) were SiC (3C, 6H, 4H), α-Si_3N_4, β-Si_3N_4 and trace amounts of elemental silicon. The total content of SiC and Si_3N_4 were 72-76 wt% and 28-23 wt% respectively. The quantitative Rietveld refinement of the XRD data is summarized in Table 5.1. Table shows that the relative concentration of total SiC and total Si_3N_4 does not change significantly across the block except for the α/β ratio.

A higher content of α-Si_3N_4 was evident near the surface of the virgin block. In the center, α-Si_3N_4 was still the dominant phase, while the content of β-Si_3N_4 increased in the center compared to that in the surface. Correspondingly a higher α/β ratio was found near the surface.

The variation of α/β ratio is due to the fabrication conditions, heating temperature and rate, and the material properties, like oxygen impurity and moisture in nitrogen gas, oxygen and cation impurity in raw materials etc. During nitridation, the oxygen content is expected to be higher near the surface of the block due to the oxygen content in N_2, which leads to a higher O_2 activity at the surface dur-

[1]Block C and D were used for investigating the thermal properties of the sidewall block which will be discussed in Chapter 7.

Table 5.1: Quantitative Analysis (wt%) by the Rietveld Refinement of XRD Data of the Virgin Blocks.

Sample Label			α-Si_3N_4	β-Si_3N_4	**Si**	Si_3N_4 **Total**	**SiC Total**	α/β **Ratio**
Block A1	Surface	B6	20.8	5.8	0.4	26.7	73.0	3.57
	Surface	B10	22.2	5.6	0.5	27.9	71.6	3.95
	Surface	A10	22.5	5.1	0.4	27.6	72.1	4.41
	Surface	C10	20.6	7.0	0.4	27.6	72.0	2.95
	Center	B2	16.5	10.6	0.5	26.2	72.4	1.56
	Center	B7	17.0	6.8	0.4	23.8	75.8	2.50
	Center	B8	17.6	7.4	0.3	25.0	74.7	2.37
	Center	B9	17.2	9.3	0.5	26.4	73.1	1.86
	Center	B12	16.2	11.5	0.3	27.8	71.9	1.41
Block A2	Surface		22.2	4.0	0.4	26.1	73.4	5.57
	Center		15.3	11.0	0.4	26.2	73.4	1.39
Block A3	Center		18.0	7.2	0.4	25.2	74.4	2.50
Block B	Surface		19.7	7.0	0.4	26.8	72.9	2.80
	Center		0.5	25.4	0.4	26.0	73.6	0.02
Block C	Surface		10.0	13.9	0.5	23.9	75.4	0.72
	Center		8.7	13.1	0.3	21.8	77.7	0.66
Block D	Surface		18.3	1.1	0.4	19.4	80.2	17.3
	Center		12.9	6.9	1.9	19.9	78.3	1.9

ing nitridation. On the other hand, the temperature varies across the block during nitridation. The temperature is higher near the surface initially, but the temperature becomes higher in the center due to the nature of the exothermic nitridation reaction since the generated heat is trapped and difficult to be transported outwards [106]. Liquid phase (Si melt, T_{melt}=1410°C [28]) might be present in this case especially with Fe impurity which lowers the melting point of Si. $FeSi_x$ can be present at above 1207°C [31]. High temperature and the presence of the liquid phase favor the formation of β-Si_3N_4, which explains the higher content of β-Si_3N_4 in the center than its content at the surface. Figure 5.1 illustrates a proposed profile of the O_2 partial pressure and temperature across the block. In brief, it is propsed that the high oxygen activity and low temperature results in a higher content of α-Si_3N_4 near the surface of the block, and the high temperature results in a relatively higher content of β-Si_3N_4 in the center.

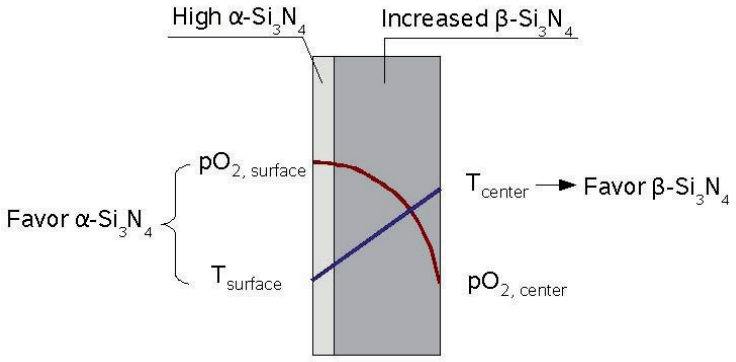

Figure 5.1: Hypothesis O_2 partial pressure and temperature distribution across the block. Transport of O_2 is assumed to be diffusion controlled and the transport of heat is by conduction.

5.2 Microstructure

The apparent porosity of the virgin blocks is around 13-15 vol% and the density is around 2.7 g/m^3 for Block A and Block B. The porosity in the center part is around 1 vol% higher than the area close to the block surface. The lower porosity and the higher density at the surface were observed in all the virgin blocks. The measured data are listed in Table 5.2.

Table 5.2: The apparent porosity and bulk density of the virgin blocks.

Sample		Apparent Porosity [vol%]	Bulk Density [kg/m^3]
Block A1	Surface	13.9	2.73
	Center	14.6	2.71
Block B	Surface	13.0	2.77
	Center	14.2	2.75
Block C	Surface	13.0	2.78
	Center	13.7	2.76
Block D	Surface	15.0	2.69
	Center	16.5	2.65

The nitridition reaction, Equation (2.1), gives theoretically 21.9% or 21.2% volume increase in the solid state when considering all the nitride is α-Si_3N_4 or β-Si_3N_4 respectively[2]. The nitride phase fills up the pores in the green body, so that the shape and the volume of final block does not change from the green body. The lower porosity in the area close to the surface of the block might imply a higher α-Si_3N_4 contenct or a higher nitridation level at the surface. Alternatively, it can result from a high green packing density near the surface.

The microstructure of the Si_3N_4-bonded SiC materials is shown in Figure 5.2. Large SiC grains, which vary from tens of micrometers to a millimeter in size, are dispersed in the fine grained Si_3N_4 binder phase.

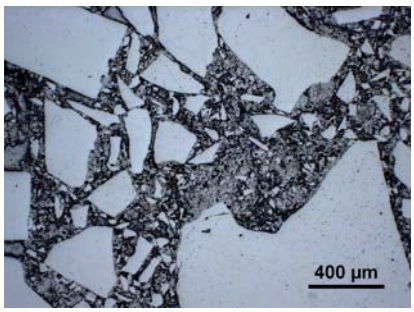

Figure 5.2: Microstructure of Si_3N_4-bonded SiC materials consists of large SiC grains and fine Si_3N_4 binder (Optical image).

[2]The calculation is based on the theoretical crystaline density of each phase from the PDF data base (DIFFRAC^{plus}Maint, Bruker AXS, Germany). Si: 2.329 g/cm^3, α-Si_3N_4: 3.183 g/cm^3 and β-Si_3N_4: 3.20 g/cm^3.

The Si_3N_4 binder consists of sub-micrometer α-Si_3N_4 and β-Si_3N_4 particles. The microstructure of the area close to the surface of the block differs from the center part as shown in Figure 5.3 and Figure 5.4 respectively.

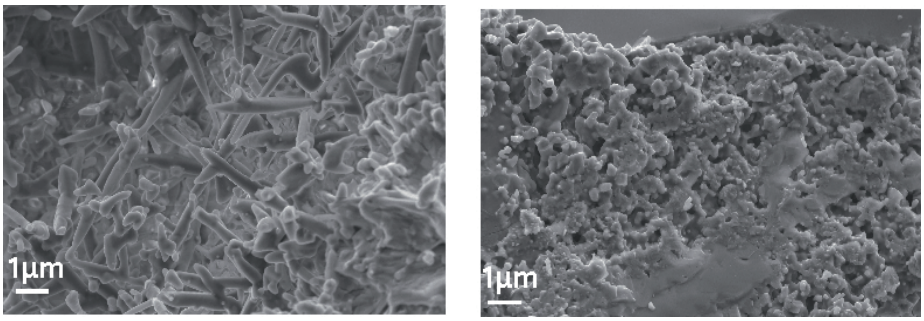

(a) Needle like α-Si_3N_4. (b) Background matte α-Si_3N_4.

Figure 5.3: SEM images of the sample from the area close to the surface of the virgin block.

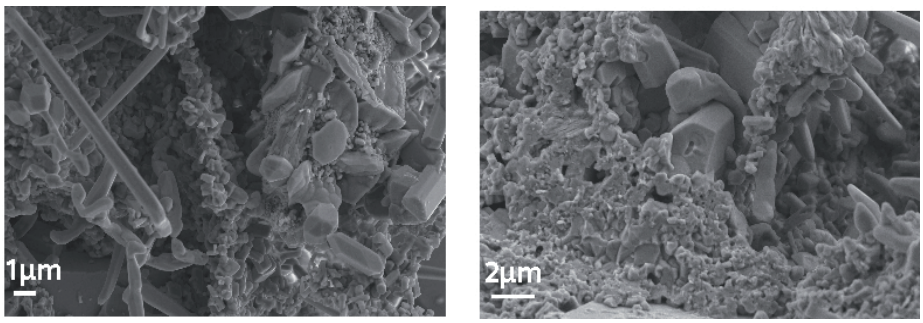

(a) Hexagonal rod β-Si_3N_4. (b) Granular β-Si_3N_4 growth from molten Si.

Figure 5.4: SEM images of the sample from the center part of the virgin block.

The area close to the surface of the virgin block contains more needles and most of the needles grow in the pores, while the center of the block contains more hexagonal rods. The needle and the hexagonal granular are proposed to be α-Si_3N_4 and β-Si_3N_4 according to the nature of their formation mechanism. The formation of α-Si_3N_4 needles could be the reaction between the N_2 and Si vapor and/or SiO(g). A higher content of α-Si_3N_4 needles is in agreement with the phase composition obtained by Rietveld refinement. Moreover, the needle grains which are shown in Figure 5.3(a) were confirmed to be α-Si_3N_4 by calculating the unit cell parameters from the electron diffraction pattern shown in Figure 5.5. The

high resolution TEM image and its diffraction pattern are also shown in Figure 5.5.

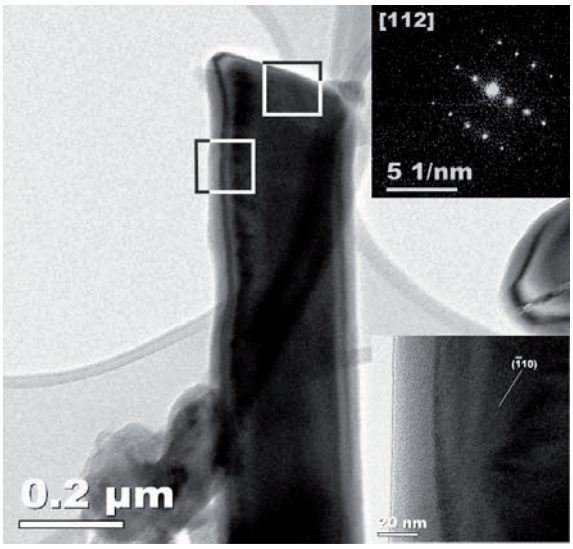

Figure 5.5: High resolution TEM image and diffraction pattern of the needle phase from the area close to the surface of the virgin block.

The needle like α-Si_3N_4 particles were typically in the range of 0.1 to 0.6 μm in width and a few micrometers in length. The β-Si_3N_4 rods were well formed and found generally thicker than the α-Si_3N_4. Similar structures were found in the other virgin Si_3N_4-bonded SiC blocks. The Si_3N_4 particles are significantly smaller than the SiC grains and thereby have significantly higher surface area and are more vulnerable when exposed to degradation agents, such as Na vapor, oxidizing gases and fluoride gases as discussed further below. The high surface area explains why the Si_3N_4 binder matrix is the weakest part of the materials. In addition, needle like α-Si_3N_4 particles have even larger surface area compared to β-Si_3N_4, and α-Si_3N_4 particles are expected to be kinetically more unstable during degradation.

5.3 Discussion

Under the normal industrial fabrication condition, the nitride binder can not be phase pure. It always contains α-Si_3N_4 and β-Si_3N_4. α-Si_3N_4 forms at the early stage when the nitridation temperature is low and has a higher content near the

surface of the virgin block due to a higher oxygen potential resulted from the oxygen content in the suppling nitrogen gas. The morphology of α-Si_3N_4 can be needle like (Figure 5.3(a)) or exist as background matte (Figure 5.3(b)). In the later stage of nitridation when the temperature is high, the formation of β-Si_3N_4 is favored, especially when liquid phase (Si or $FeSi_x$ melt) has been present. The granular β-Si_3N_4 is well formed crystal and has a hexagonal morphology. The higher content of α-Si_3N_4 or a higher level of nitridation at the area close to the surface of the virgin block results in a lower porosity compared with the center part. In the fabrication, a low temperature initially is necessary to avoid an early formation of the liquid phase before the Si_3N_4 skeleton is built. Otherwise, the Si melt might flow out of the green body [107]. In addition, a higher content of α-Si_3N_4 near the surface of the virgin block is believed to be the reason for the lighter color layer near the surface which was often observed in the virgin blocks shown in Figure 4.2 in Chapter 4. The α-Si_3N_4 needles appear white in an optical microscope.

The significant size difference between the Si_3N_4 (sub-micrometer) and SiC grains (mm) points out that kinetically Si_3N_4 is the weaker part of the materials. Meanwhile, the microstructure evolution also has significant influence on the thermal property of the blocks. The chemical stability and thermal property of the block will be discussed in the following chapters.

Chapter 6

Degradation Mechanisms of the Sidewall Block

6.1 Autopsies

6.1.1 Mineralogical and Chemical Analysis

The phase composition of spent sidewall blocks can be different from cell to cell based on the operation conditions even with similar materials. The phase composition of the spent blocks at the age of 270 and 604 days were similar. The main degradation products detected by XRD were Si_2ON_2 in the gas zone at the top and Na_2SiO_3 in the electrolyte zone at the bottom. The XRD patterns are shown in Figure 6.1. The content of β-Si_3N_4 was more pronounced in the gas zone than that in the electrolyte zone.

For the spent block from an older cell at the age of 1569 days, Si_2ON_2 was found further down to the electrolyte zone near the bottom of the block in addition to the main degradation phase Na_2SiO_3. In the gas zone, chiolite ($Na_5Al_3F_{14}$) and AlF_3 were identified in addition to Si_2ON_2. The fluoride phases are proposed to be formed by the condensation reaction (6.1) of the volatized bath content $NaAlF_4$ in the pot gas. Moreover, the presence of β-Si_3N_4 phase was more pronounced and α-Si_3N_4 phase was hardly detected in the gas zone. The corresponding XRD diffractograms are shown in Figure 6.2.

$$5NaAlF_4(g) \rightarrow Na_5Al_3F_{14}(s) + 2AlF_3(g/s) \tag{6.1}$$

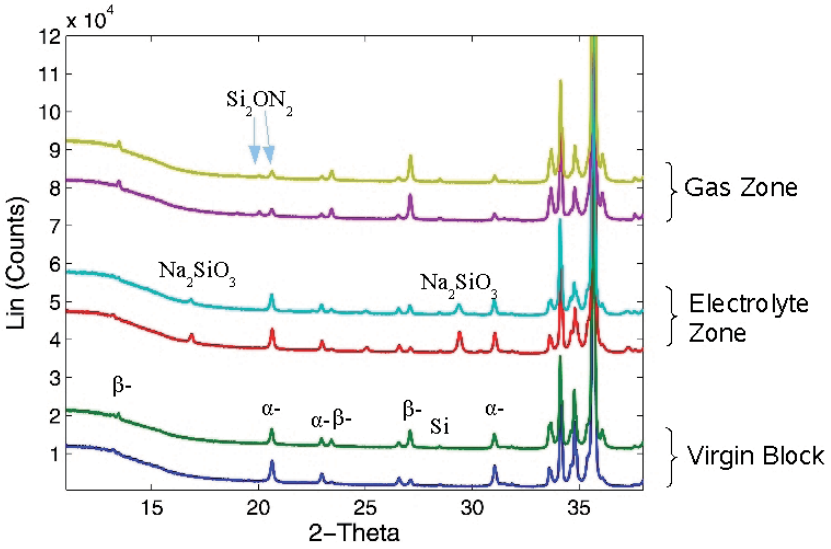

Figure 6.1: XRD profiles for samples from the electrolyte zone, gas zone of the spent block at the age of 270 days together with 2 samples from the virgin block for comparison. α- represents α-Si_3N_4; β- represents β-Si_3N_4. Un-labeled reflections are for SiC.

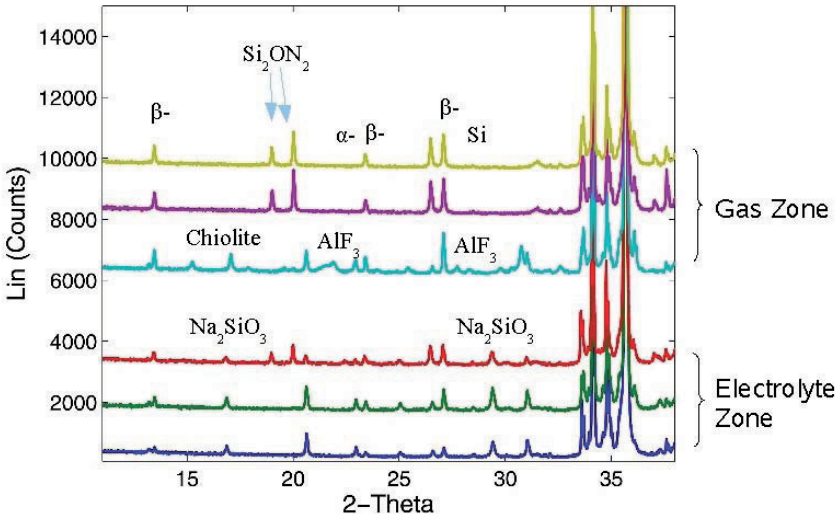

Figure 6.2: XRD profiles for samples from the electrolyte zone, gas zone of the spent block at the age of 1569 days. α- represents α-Si_3N_4; β- represents β-Si_3N_4. Un-labeled reflections are for SiC.

The Si content in these three blocks were in the range of 0.2-0.7 wt% and had no significant change with age. The content of α-Si_3N_4, β-Si_3N_4, SiC and the degradation phases present in the three spent blocks at the age of 270, 604[1] and 1569 days is summarized in Table 6.1. The data were obtained by quantitative Rietveld refinement of the XRD patterns.

For the younger cell (270 days), the content of reaction products in the electrolyte zone was much higher than in the gas zone. For the older cell (1569 days), the oxidation in the gas zone was more severe and Si_2ON_2 was found down to the electrolyte zone. In all three blocks, Na_2SiO_3 was restricted to the electrolyte zone. This means that sodium diffusing from the carbon cathode into the sidewall block does not penetrate much further upwards in the vertical direction. This phenomena is not expected by the fast diffusion rate of sodium gas. It is proposed that oxygen containing species diffusing downwards from the top of the sidewall blocks condenses the sodium gas and retards further diffusion and reaction of sodium. Finally, it should be noted that the amount of the degradation phase Na_2SiO_3 in the older cell is not higher than that in the younger cell, which implies that age is not the only factor influencing the degradation.

The α/β Si_3N_4 ratio varied significantly in the gas zone after degradation. α-Si_3N_4 was dominant in the binder phase of the virgin block and α/β ratio was higher than one. In the gas zone after oxidation, the ratio reduced due to the reduction of the α-Si_3N_4 content. The ratio was even less than one in the block at the age of 270 and 1569 days meaning that β-Si_3N_4 dominated in the gas zone after degradation. This indicates that α-Si_3N_4 is more reactive and also suggests the possibility of α to β-Si_3N_4 transformation. The phenomenon was more pronounced in the cell at the age of 1569 days: α/β ratio reduced to 0.03 and α-Si_3N_4 content was as low as 0.5 wt%. α/β ratio seems to have a relationship with the amount of Si_2ON_2 as shown in Figure 6.3. With increasing amount of Si_2ON_2, the α/β ratio decreases accordingly. It implies that α-Si_3N_4 is preferably oxidized to form Si_2ON_2 and the α to β-Si_3N_4 transformation may be related to the formation of Si_2ON_2. In any case, α/β ratio correlates well with the degree of oxidation in the gas zone.

The chemical analysis (LECO) gives the concentration of the total nitrogen and oxygen in the samples. The increase in oxygen content is always accompanied by a decrease in the nitrogen content as shown in Figure 6.4. The nitride binder phase is clearly the chemically degraded part of the sidewall block materials.

[1] XRD raw data for the spent block at the age of 604 days were collected by CERAM Research Ltd, UK.

Table 6.1: Quantitative Analysis (wt%) by the Rietveld Refinement of XRD Data of the Spent Blocks at the Age of 270, 604* and 1569 Days. [1]: close to the surface to the frozen bath, [2]: close to the surface to the steel shell. *: XRD raw data were collected by CERAM Research Ltd, UK.

Sample Label		α-Si_3N_4	β-Si_3N_4	Si_3N_4 Total	SiC Total	α/β Ratio	Na_2SiO_3	Si_2ON_2	Age
Electrolyte Zone	C1[1]	19.6	3.5	23.0	64.5	5.68	12.1		270 days
	C2	15.9	6.4	22.3	63.1	2.24	14.2		
	C3	16.3	6.1	22.5	67.8	2.66	9.2		
	C4[2]	21.5	4.1	25.6	72.6	5.32	1.2		
Gas Zone	D1	6.5	15.5	22.0	76.7	0.42		0.8	
	D2	5.0	18.8	23.8	74.4	0.26		1.2	
	D3	6.2	15.9	22.1	76.9	0.39		0.5	
	D4	3.0	15.1	18.1	80.4	0.20		1.0	
Elec. Zone	E1[1]	25.4	2.3	27.7	71.3	10.94	0.6		604 days
	E2	21.0	5.0	26.0	67.1	4.17	6.5		
	E3	17.0	7.7	24.6	65.0	2.19	9.8		
	E4	23.5	4.6	28.1	69.5	5.16	1.9		
	E5[2]	26.0	2.0	27.9	70.4	13.30	1.2		
Gas Zone	F2	16.3	9.6	25.9	72.8	1.70		0.9	
	F3	16.5	10.0	26.6	72.2	1.65		0.9	
	F4	20.7	8.1	28.7	70.8	2.56		0.1	
	F5[2]	21.0	7.0	28.0	71.6	2.99		0.1	
Elec. Zone	G1[1]	8.0	2.6	10.5	84.2	3.10	5.7		1569 days
	G2	11.0	6.7	17.7	73.8	1.62	2.2		
	G3	3.9	6.4	10.4	79.9	0.61	2.7	4.1	
	G4	3.7	9.2	12.8	78.9	0.40	5.3	2.2	
	G5[2]	12.0	4.5	16.5	78.0	2.68	2.87	0.7	
Gas Zone	H3	0.3	10.2	10.5	81.4	0.03		7.9	
	H4	0.7	10.4	11.1	82.0	0.07		6.7	
	H5[2]	0.8	10.2	11.0	85.1	0.08		3.7	

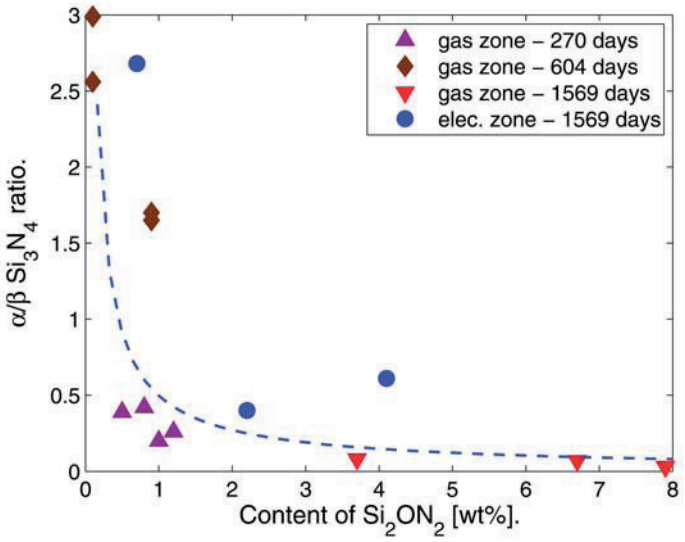

Figure 6.3: α/β ratio as a function of Si_2ON_2 amount. The dashed line is the guide to the eyes.

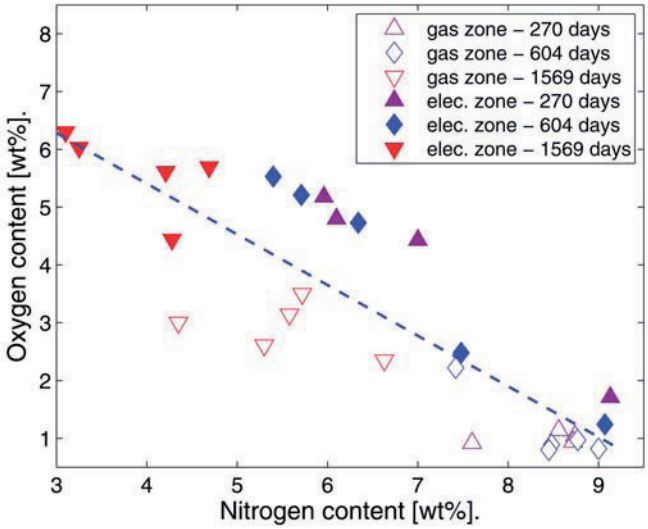

Figure 6.4: Oxygen content as a function of nitrogen content in the spent sidewall blocks. The dashed lines are the guide to the eyes.

The oxygen content variation across the three spent blocks is plotted in Figure 6.5. For the younger cell, only the area close to the bath was oxidized, while for the older cell, the oxidation area extended further towards the steel shell. Generally, the oxidation in the electrolyte zone is more severe than the oxidation in the gas zone. In the old cell operated for 1569 days, the oxidation in the gas zone increases significantly and the oxygen content in the two regions are more comparable.

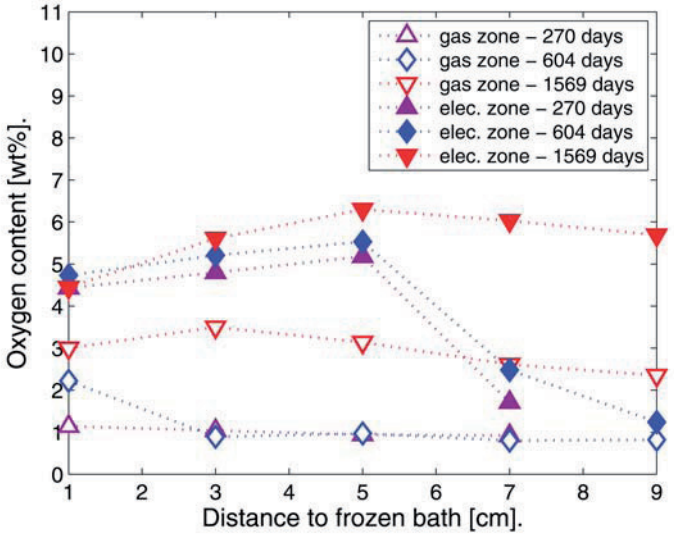

Figure 6.5: Oxygen content vs. distance to the frozen bath for the spent sidewall blocks at the age of 270, 604 and 1569 days.

For the spent block at the age of 1767 days, the degradation phases were different compared to the three spent blocks shown above. The secondary phase observed was cristobalite (low) in the gas zone and a mixture of Na_2SiO_3 and $Na_2Si_2O_5$ in the electrolyte zone. The corresponding XRD diffractograms are shown in Figure 6.6. The difference in the type of degradation phase of this block implies differences in the operation condition of the cell, which will be discussed in Section 6.2. The amount of α-Si_3N_4, β-Si_3N_4, SiC and the degradation phases present in the spent block at the age of 1767 days is summarized in Table 6.2. The data were obtained by quantitative Rietveld refinement. The presence of α-Si_3N_4 and β-Si_3N_4 was similar in the gas zone and the electrolyte zone, which was also different compared to the above mentioned three blocks.

Table 6.2: Quantitative Analysis (wt%) by the Rietveld Refinement of XRD Data of the spent blocks at the age of 1767 days. [1]: close to the surface to the frozen bath, [2]: close to the surface to the steel shell.

Sample Label		α-Si_3N_4	β-Si_3N_4	Si_3N_4 Total	SiC Total	α/β Ratio	Na_2SiO_3	$Na_2Si_2O_5$	Cristobalite Low
Electrolyte Zone	S1	17.4	2.3	19.7	69.1	7.53	10.9		
	S2	14.8	3.3	18.1	68.5	4.54	13.1		
	S3	14.7	3.3	18.0	69.4	4.49	12.5		
	S7	13.9	4.9	18.8	67.6	2.84	8.1	5.3	
	S9	15.6	2.6	18.3	65.3	5.95	6.7	9.6	
Gas Zone	Top 3-5	19.5	2.5	22.1	73.9	12.90			4.3
	Top 3-4	18.6	2.4	20.9	74.4	7.90			4.5
	Top 3-2[2]	18.4	1.4	19.9	75.6	7.69			3.8
	Top 4-2	18.8	2.3	21.1	73.6	8.33			5.1

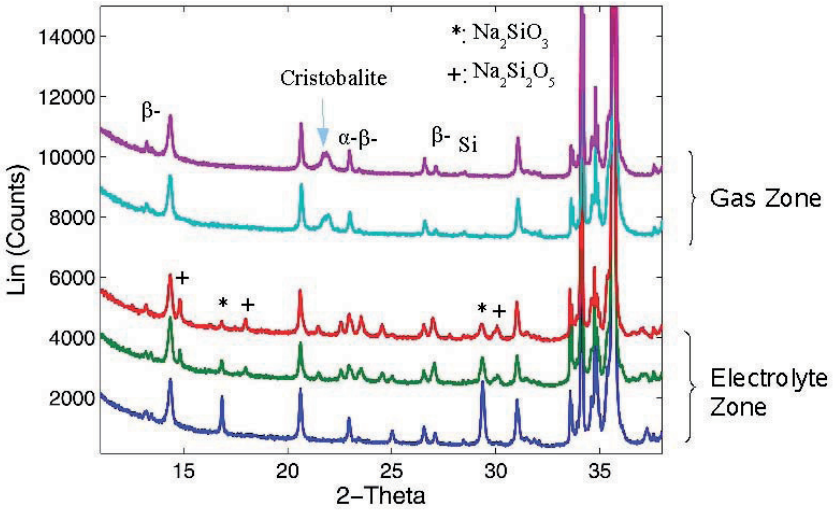

Figure 6.6: XRD profiles for samples from the electrolyte zone, gas zone of the spent block at the age of 1767 days. α- represents α-Si_3N_4; β- represents β-Si_3N_4. Un-labeled reflections are for SiC.

6.1.2 Microstructure

Bulk Density and Apparent Porosity During cell operation, the degradation products (Na_2SiO_3 and/or $Na_2Si_2O_5$) fill up the pores in the electrolyte zone at the bottom part of the block and densify the block correspondingly. The porosity variation across the spent block with different ages is shown in Figure 6.7. In the infiltration area, the porosity reduced dramatically and could be as low as 1 vol%. Correspondingly, the density was increased up to 2.9 g/cm^3. In the gas zone at the top, the porosity remained high around 9-16 vol%, and in most cases the porosity was even higher than for the virgin materials. The density did not change significantly. At the region close to the surface towards the ledge in the gas zone, the material disintegrated and the density/porosity could not be measured. The porosity in this area is proposed to be significantly higher than the collected data since the material disintegrated easily and appeared as porous.

The reduction in the porosity reflects the extent of oxidation and the porosity to some degree correlates with the oxygen content. The porosity as a function of oxygen content for the blocks aged 270, 604 and 1569 days is shown in Figure 6.8. The porosity decreases with the increasing oxygen amount. The correlation is more evident in the electrolyte zone than that in the gas zone. The explanation for

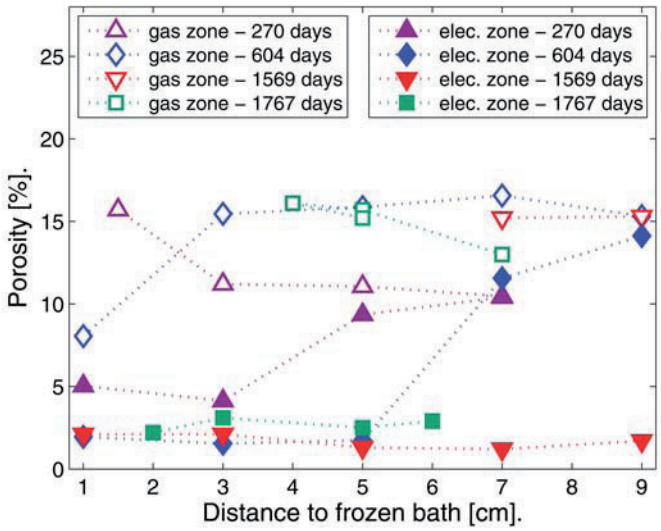

Figure 6.7: The porosity vs. distance to the bath for the spent sidewall blocks at the age of 270, 604, 1569 and 1767 days. The measured porosity for virgin materials is 13.9 to 14.6 vol%.

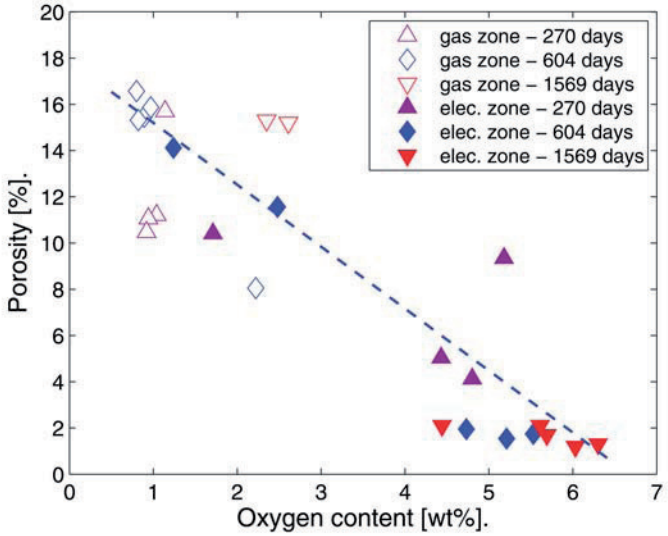

Figure 6.8: The porosity as a function of oxygen content for the blocks aged 270, 604 and 1569 days. The dashed line is the guide to the eyes.

this is that the oxygen content exactly reflects the the amount of the degradation phase sodium silicates in the electrolyte zone, but can not reflect accurately the amount of the oxidation product Si_2ON_2 or cristobalite in the gas zone due to the influence of the fluoride gas. Details will be discussed in Section 6.2.

Pore Size Distribution The pore size distribution of the virgin and the spent block at the age of 1767 days is shown in Figure 6.9 and 6.10. In agreement with the measured apparent porosity, the sample from the gas zone of the spent block had the highest pore volume, while there was almost no pore left in the sample from the electrolyte zone. The sequence in the pore volume is:

$$V_{spent-gas\ zone} > V_{virgin-surface} > V_{virgin-center} >> V_{spent-electrolyte\ zone}$$

The pore size was smaller in the region close to the surface of the virgin block where more α-Si_3N_4 needles were present than at the center. Pore size distribution was narrower in the gas zone of the spent block than in the virgin block.

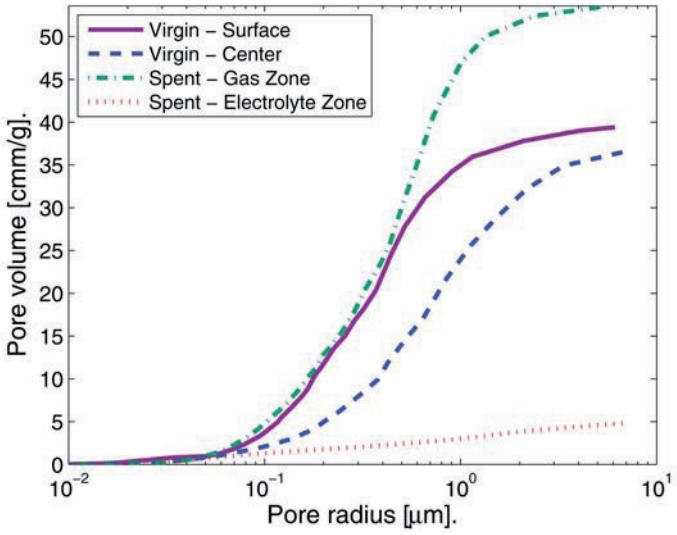

Figure 6.9: Pore size distribution of the virgin and the spent blocks at the age of 1767 days. Accumulated pore volume.

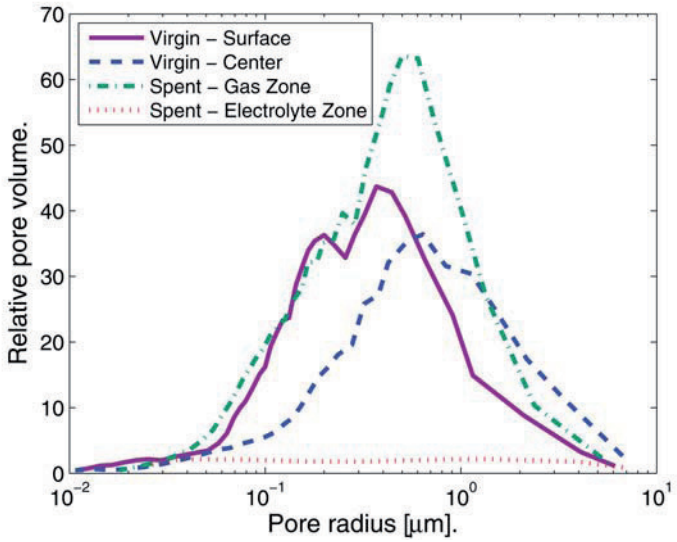

Figure 6.10: Pore size distribution of the virgin and the spent blocks at the age of 1767 days. Relative pore volume.

Morphology of the Degradation Phase in the Spent Block The microstructure of the material in the electrolyte zone of the spent block (1767 days) is shown in Figure 6.11. The sodium silicates crystal morphology is shown in Figure 6.11(a) and 6.11(b), resulted from the reaction with the Si_3N_4 binder. Sodium silicate flake-like crystals are evident in Figure 6.11(b). In addition, a sodium silicate layer surrounding the remaining large SiC grain is shown in Figure 6.11(c) and 6.11(d). Clearly, both Si_3N_4 and SiC were attacked by the sodium and the oxidizing gases in the electrolyte zone. However, due to the significant difference in the grain size of the two phases, Si_3N_4 is attacked more severly by the degradation agents. Hence, in macro-scale, Si_3N_4 is the weak part of the Si_3N_4-bonded SiC materials.

The microstructure of the gas zone of the spent block is shown in Figure 6.12(a) and 6.12(c). After degradation, the amount of the needles present in the binder were increased and the needles were thinner than those found in the virgin block shown in Figure 6.12(b) and 6.12(d). The thinner needles, or fibers are in line with the increase in the apparent porosity (Figure 6.7) and pore volume (Figure 6.9 and 6.10) in the gas zone of the spent block.

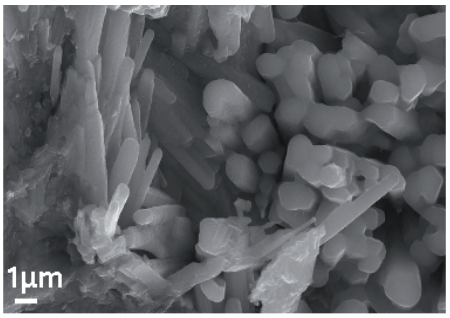

(a) Sodium silicate reacted from nitride binder.

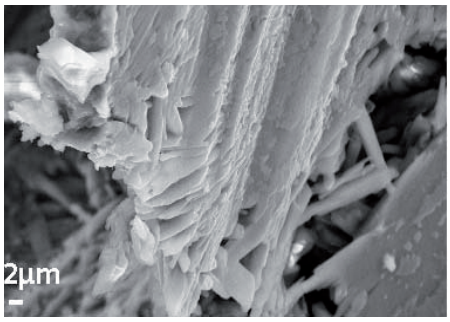

(b) Sodium silicate flakes.

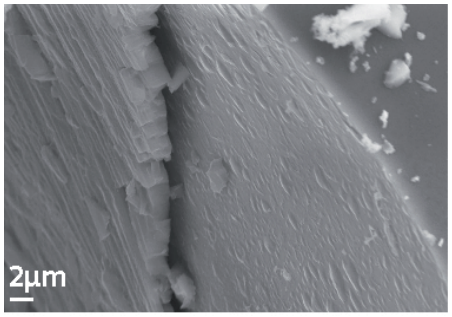

(c) Clear layer structure an surrounding un-reacted SiC particles.

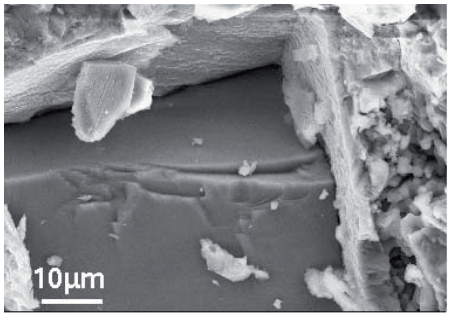

(d) Sodium silicate surrounding an un-reacted SiC particles.

Figure 6.11: SEM images of the electrolyte zone of the spent block (1767 days).

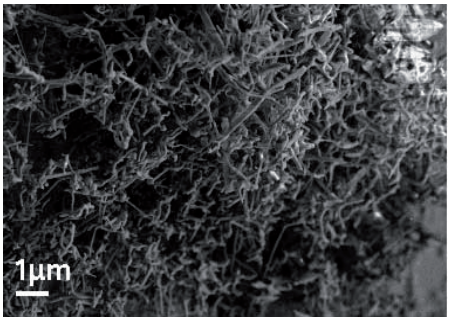

(a) Thinner needles from the top (1767 days.

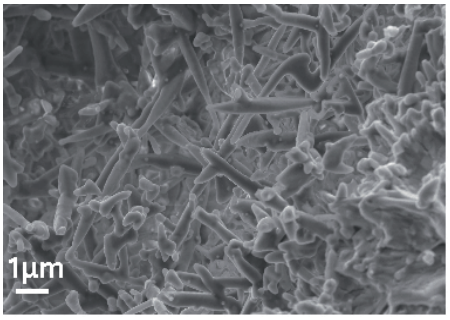

(b) Needles from the virgin surface (Block B).

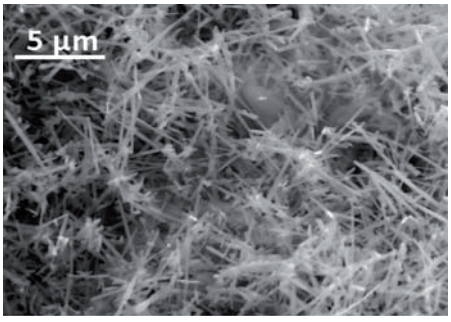

(c) Thinner needles from the top (270 days).

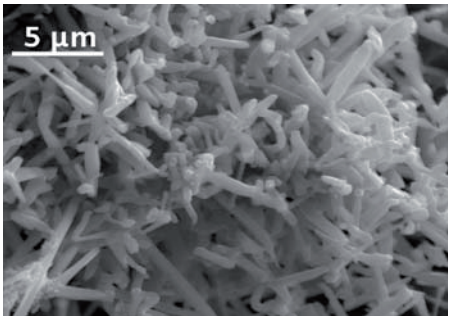

(d) Needles from the virgin surface (Block A).

Figure 6.12: SEM images of the gas zone of the spent block showing finer needles compared with virgin samples.

A high resolution TEM image of the thinner needles in the gas zone is shown in Figure 6.13. There are two kinds of needles, or fibers. One kind is relatively thicker and has a smooth surface, and the other kind is thinner in tens of nanometers and has rough surface and "bamboo" structure. The former was confirmed to be α-Si_3N_4 by calculating the unit cell parameters from the electron diffraction pattern, but the latter was not able to be identified accurately because of the difficulties in getting good low index diffraction pattern due to its tiny structure and the surrounding "large" needles.

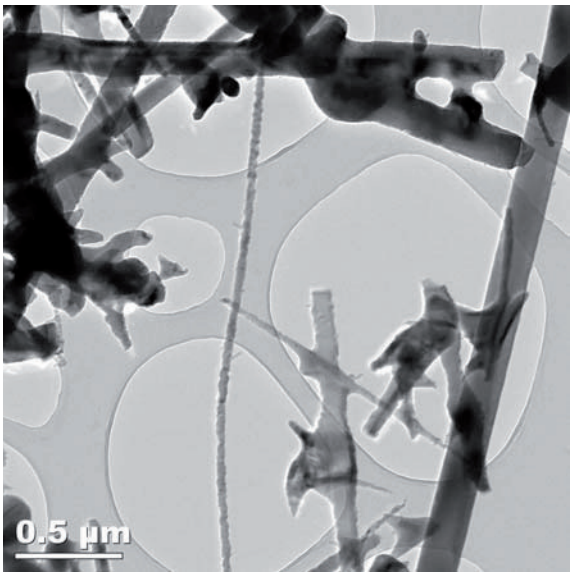

Figure 6.13: High resolution TEM image and diffraction pattern of the needle phase from the area close to the surface of the virgin block.

6.2 Degradation Mechanisms

6.2.1 Thermodynamics and Proposed Degradation Reactions

Thermodynamic data[2] for reactions (6.2) to (6.5), demonstrate that SiC is more unstable due to a more negative Gibbs energy for the reactions with Na(g), O_2(g)

[2] All thermodynamic calculations are done by using FactSage™ 5.2 [29].

and HF(g)[3]. The data given below are normalized to 1 mole Na(g) or HF(g).

$$\begin{aligned} Na(g) + \frac{1}{6}Si_3N_4(s) + \frac{3}{4}O_2(g) &= \frac{1}{2}Na_2SiO_3(s) + \frac{1}{3}N_2(g) \\ \Delta G^{\circ}(850K) &= -591.7kJ/mol \end{aligned} \tag{6.2}$$

$$\begin{aligned} Na(g) + \frac{1}{2}SiC(s) + \frac{3}{4}O_2(g) &= \frac{1}{2}Na_2SiO_3(s) + \frac{1}{2}C(s) \\ \Delta G^{\circ}(850K) &= -635.7kJ/mol \end{aligned} \tag{6.3}$$

$$\begin{aligned} HF(g) + \frac{1}{12}Si_3N_4(s) + \frac{1}{4}O_2(g) &= \frac{1}{4}SiF4(g) + \frac{1}{2}H_2O(g) + \frac{1}{6}N_2(g) \\ \Delta G^{\circ}(850K) &= -157.3kJ/mol \end{aligned} \tag{6.4}$$

$$\begin{aligned} HF(g) + \frac{1}{4}SiC(s) + \frac{1}{4}O_2(g) &= \frac{1}{4}SiF_4(g) + \frac{1}{2}H_2O(g) + \frac{1}{4}C(s) \\ \Delta G^{\circ}(850K) &= -179.7kJ/mol \end{aligned} \tag{6.5}$$

In contrast to the thermodynamic data, the experimental observations have demonstrated that Si_3N_4 binder is more reactive. In fact, both SiC and the Si_3N_4 were attacked by the degradation agents, but since Si_3N_4 binder has much higher surface area relative to the coarse SiC grains, considerable higher amount of Si_3N_4 binder was reacted during degradation. Hence, Si_3N_4 is the weak part of the Si_3N_4-bonded SiC materials due to kinetics and not thermodynamics. In the following section, only reactions related to Si_3N_4 are discussed.

6.2.1.1 Reaction in the Electrolyte Zone

In the electrolyte zone the main degradation phases were Na_2SiO_3 for the spent blocks with the age of 270, 604, 1569 days, and a mixture of Na_2SiO_3 and $Na_2Si_2O_5$ for the spent block with the age of 1767 days. The different secondary phases imply different reaction environments, like oxygen potential and temperature.

The calculation of chemical equilibrium when sodium reacts with SiO_2 by minimizing the Gibbs energy is shown in Figure 6.14. The calculation demonstrates

[3]Due to the protection of side ledge, molten bath does not likely infiltrate into the sidewall block to cause degradation, therefore the reactions related to the bath components will not be discussed in this section.

that $Na_2Si_2O_5$ is more favorable by thermodynamics, but sodium is coexisting with only one of the sodium silicates Na_2SiO_3 (sodium metasilicate) and not $Na_2Si_2O_5$ (sodium disilicate). Sodium is not stable with the other sodium silicates, and it will be consumed as long as the other sodium silicates are present in the block. Therefore, the presence of only Na_2SiO_3 in the spent blocks at the age of 270, 604 and 1569 days suggests that sodium is in excess. This demonstrates that there were reducing conditions (high Na activity or low O_2 activity) in the sidewall block close to the cathode. The presence of $Na_2Si_2O_5$ in the spent block at 1767 days implies less reducing conditions in the sidewall during operation and that no excess free sodium was present.

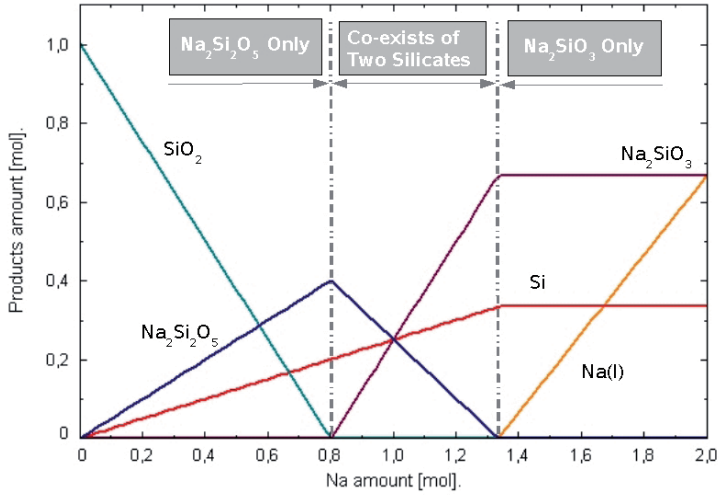

Figure 6.14: The amount of compounds present at equilibrium when SiO_2 is exposed to increasing amount of Na(g) at 850 K. Calculate by using FactSage™ 5.2.

Based on the chemical environment in the cell, the possible reactions between Si_3N_4 binder, Na(g) and oxidizing gases (O_2, CO or CO_2) could be reaction (6.6) to (6.8) [4]

$$\begin{aligned} \frac{1}{6}Si_3N_4(s) + Na(g) + \frac{3}{4}O_2(g) &= \frac{1}{2}Na_2SiO_3(s) + \frac{1}{3}N_2(g) \\ \Delta G^\circ(850K) &= -591.7kJ/mol \end{aligned} \tag{6.6}$$

$$\begin{aligned} \frac{1}{6}Si_3N_4(s) + Na(g) + \frac{3}{2}CO(g) &= \frac{1}{2}Na_2SiO_3(s) + \frac{1}{3}N_2(g) + \frac{3}{2}C(s) \\ \Delta G^\circ(850K) &= -311.3kJ/mol \end{aligned} \tag{6.7}$$

[4]The reactions related to the formation of $Na_2Si_2O_5$ are similar and are not given.

$$\begin{aligned} \frac{1}{6}Si_3N_4(s) + Na(g) + \frac{3}{2}CO_2(g) &= \frac{1}{2}Na_2SiO_3(s) + \frac{1}{3}N_2(g) + \frac{3}{2}CO(g) \\ \Delta G^{\circ}(850K) &= -278.5kJ/mol \end{aligned} \quad (6.8)$$

Estimations of the theoretical change in porosity due to the chemical reactions can be helpful to identify the possible reactions in the sidewall block. By assuming the total volume of the block to be constant, the theoretical change in the porosity can be estimated according to the proposed stoichiometric reactions taking the density of the reactants and products into account. Figure 6.15 illustrates the reduction in porosity (solid lines in figure) due to the sodium deterioration in the electrolyte zone by theoretic calculations according to reactions (6.6) to (6.8) proposed above[5]. The experimental data are also plotted in the figure, which shows relatively good agreement with the prediction based on reactions (6.6) and (6.8). Reaction (6.7) is therefore less likely, and the only solid product of the oxidation is Na_2SiO_3 and formation of carbon is not very likely.

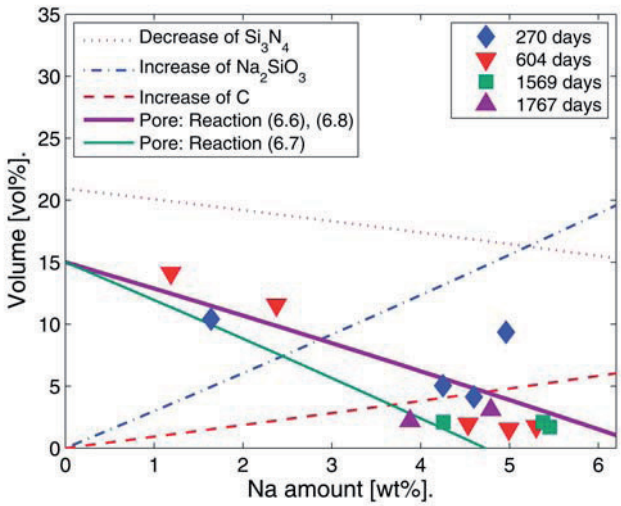

Figure 6.15: Porosity change by Na deterioration. Straight lines are the porosity reduction estimated from the stoichiometric reactions. Filled markers are the experimental data for apparent porosity correlated with sodium content. Na amount for the samples from the spent block at the age of 270, 604 and 1569 days waw derived by LECO(O) analysis, and that for 1767 days was obtained by the refinement of the XRD data.

[5]The calculations consider the formation of Na_2SiO_3, not $Na_2Si_2O_5$. Theoretical crystalline density of each phase is: Si_3N_4: 3.2 g/cm^3 (PDF data base, DIFFRAC^{plus}Maint, Bruker AXS, Germany), Na_2SiO_3: 2.4 g/cm^3 [108] and C: 2.3 g/cm^3 [108].

6.2.1.2 Reaction in the Gas Zone

In the gas zone a larger amount of fibers were observed and the fibers were thinner than the needles in the virgin materials. The thin fiber suggests that the degradation phase might be formed by gas phase reactions. Based on the observation, two degradation schemes are proposed: the formation of Si_2ON_2 and HF involved oxidation.

Formation of Silicon Oxynitride In order to evaluate the thermodynamics of the reactions related to Si_2ON_2, thermodynamic data for the Si_2ON_2 reported by Fegley [109] were incorporated into FactSage database. An error in the equation for c_p° (heat capacity) [110] was discovered, and a new regression was done based on the experimental data from [109][6].

The possible reactions of the formation of Si_2ON_2 could be through gas-solid reactions (6.9 and 6.10) and gas phase reaction (6.11). The gas phase reaction is supported by the fiber morphology of the degradation phase.

$$\begin{aligned} \frac{2}{3}Si_3N_4(s) + \frac{1}{2}O_2(g) &= Si_2ON_2(s) + \frac{1}{3}N_2(g) \\ \Delta G^\circ(850K) &= -396.0kJ/mol \end{aligned} \tag{6.9}$$

$$\begin{aligned} \frac{1}{2}Si_3N_4(s) + \frac{3}{4}SiO(g) + \frac{1}{4}CO(g) &= Si_2ON_2(s) + \frac{1}{4}SiC(s) \\ \Delta G^\circ(850K) &= -311.3kJ/mol \end{aligned} \tag{6.10}$$

$$\begin{aligned} 2SiO(g) + CO(g) + N_2(g) &= Si_2ON_2(s) + CO_2(g) \\ \Delta G^\circ(850K) &= -563.6kJ/mol \end{aligned} \tag{6.11}$$

Formation of Si_2ON_2 points to the low partial pressure of O_2 in the system because Si_2ON_2 is only stable under reducing conditions. A predominance diagram of the Si-N-O system at 850 K and 1500 K is shown in Figure 6.16. The diagram shows the stability field of each phase as a function of chemical potential at a specific temperature. The figure shows that with decrease in the temperature, Si_2ON_2

[6]The data used were $\Delta H^\circ_{f,298}$=-947.7±5.4 kJ/mol, S°_{298}=45.35±0.4 J/mol [109], and new fitting for c_p° value based on the experimental data [109] is $c_p^\circ = 139.3 - 0.0581 \times T + 4.767 \times 10^{-5} \times T^2 - 5.388 \times 10^6/T^2$ $(298 < T < 700K)$, $c_p^\circ = 110.8 + 0.01221 \times T - 1.987 \times 10^{-8} \times T^2 - 4.082 \times 10^6/T^2$ $(700 < T < 1500K)$, $c_p^\circ = 110.8 + 0.01219 \times T - 1.156 \times 10^{-8} \times T^2 - 4.081 \times 10^6/T^2$ $(1500 < T < 2500K)$.

will be stabilized at a more reducing condition or a lower oxygen potential environment. A potential Si-N-O phase diagram is shown in Figure 6.17. In the figure, Si_2ON_2 is stable at p_{O_2} = 10^{-48} to 10^{-33} bar at 850K, which is strongly reducing conditions. The stable region of Si_2ON_2 moves to lower the oxygen potential part with reducing temperature. Hillert **et** *al.* also proposed a potential Si-N-O phase diagram in equilibrium with pure Si shown in Figure 6.18 [111]. By exploiting their data, Si_2ON_2 is stable at p_{O_2} = 10^{-32} to 10^{-27} bar at 850K. Despite the difference between these two calculations[7], the formation of Si_2ON_2 in the spent block at the age of 270, 604 and 1569 days implies strong reducing conditions in the gas zone of the sidewall block. Such reducing conditions can be achieved by a CO/CO_2 buffer [112] in the system with a high partial pressure of CO(g). This is relevant to the environment in the pot gas. At these reducing conditions, the gas transportation in the sidewall block as well as in the cell might be important, since the temperature gradient may cause the precipitation of C(s) from CO(g). This might contribute to the transportation of C(s) in the sidewall block and in the cell as well.

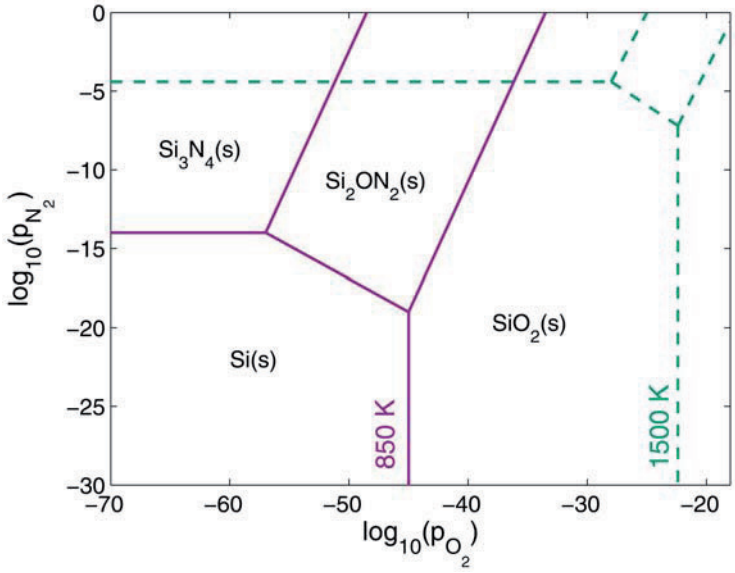

Figure 6.16: Predominance diagram of Si-N-O system at 850 K. Calculated by using FactSage™ 5.2.

[7]The difference between the two calculations might be due to they used different thermal data. By comparing to the Ellingham diagram [112], O_2 potential calculated by FactSage in the present work is more reliable.

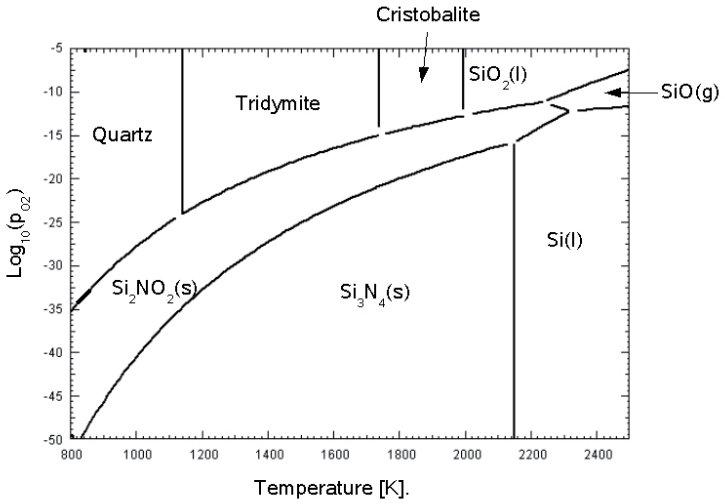

Figure 6.17: Potential Si-N-O phase diagram at p_{N_2}=1 atm. Calculated by using FactSage™ 5.2.

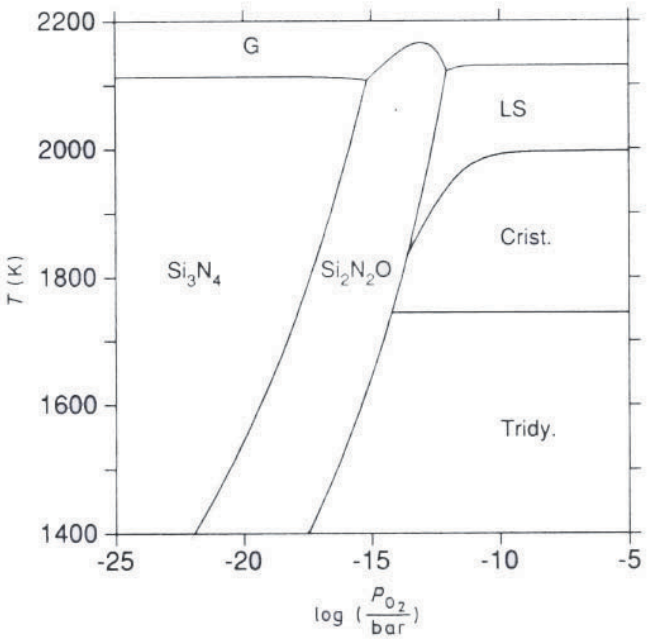

Figure 6.18: Potential Si-N-O phase diagram at a total pressure of 1 bar and in equilibrium with pure Si, solid below 1678 K and liquid above [111].

For the spent block at the age of 1767 days, the oxidation phase is cristobalite, which implies less reducing condition. This condition is similar to what was derived from the degradation phase in the electrolyte zone of the same block. It could also be due to the temperature in this block was so low that the Si_2ON_2 was more difficult to stabilize and cristobalite was formed instead.

HF Involved Oxidation The formation of Si_2ON_2 or cristobalite will fill up the pores and reduce the porosity, which is in opposition to what was observed by the porosity measurement. HF(g) is believed to be another degradation source in the gas zone. It will react with oxides [11] formed during oxidation and Si_3N_4 grains to produce SiF_4(g) and other gaseous products by reactions (6.12) to (6.14).

$$\begin{aligned} \frac{1}{4}SiO_2(s) + HF(g) &= \frac{1}{4}SiF_4(g) + \frac{1}{2}H_2O(g) \\ \Delta G^\circ(850K) &= -6.7kJ/mol \end{aligned} \tag{6.12}$$

$$\begin{aligned} \frac{1}{8}Si_2ON_2(s) + HF(g) &= \frac{1}{4}SiF_4(g) + \frac{1}{8}H_2O(g) + \frac{1}{8}N_2(g) + \frac{3}{8}H_2(g) \\ \Delta G^\circ(850K) &= -32.5kJ/mol \end{aligned} \tag{6.13}$$

$$\begin{aligned} \frac{1}{12}Si_3N_4(s) + HF(g) &= \frac{1}{4}SiF_4(g) + \frac{1}{6}N_2(g) + \frac{1}{2}H_2(g) \\ \Delta G^\circ(850K) &= -56.9kJ/mol \end{aligned} \tag{6.14}$$

The reactions may explain why α-Si_3N_4 needles become thinner over time as illustrated in Figure 6.19. It will "eat away" the Si_3N_4 binder gradually from the surface and cause the detachment of the large SiC grains as illustrated in Figure 6.20. Material loss could be observed at the top part of the gas zone facing the ledge, which is pointing to reaction (6.14).

Possibility of α to β Transition Based on the XRD data for the spent blocks at the age of 270, 604 and 1569 days it can also be suggested that α-Si_3N_4 may have transformed to β-Si_3N_4. The phase transition is suggested to go through a solid-gas-solid mechanism. This also points to a low p_{O_2} in the upper part of the sidewall block. The transformation is likely only at very reducing conditions, but not in the spent block at the age of 1767 days where the conditions were less reducing.

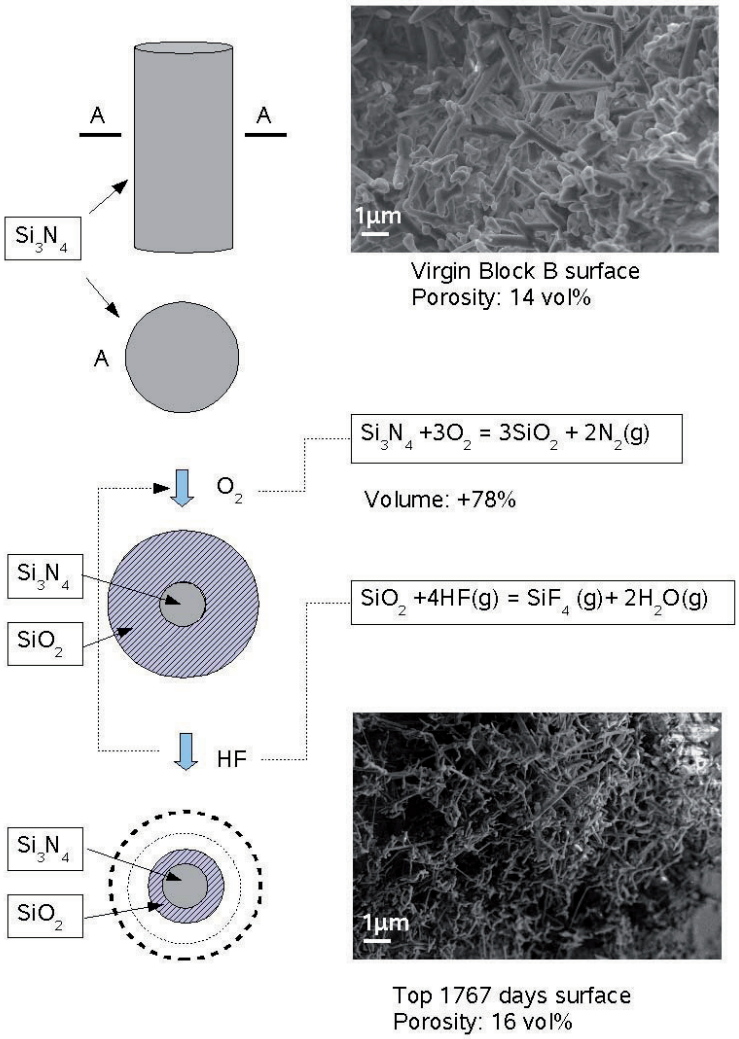

Figure 6.19: Illustration of HF involved oxidation in the gas zone which thiner the nitride needles.

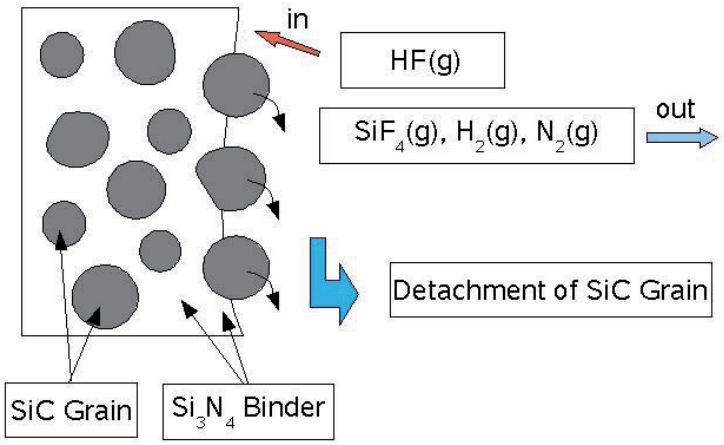

Figure 6.20: Illustration of HF involved oxidation in the gas zone which causes the material loss at the block surface.

6.2.2 Proposed Degradation Mechanisms

During normal operation, the sidewall block is almost always covered by a frozen electrolyte layer (ledge) or crust [3]. Normally the sidewall block is not exposed to the aluminum pad and the molten electrolyte directly. However, the lining materials still deteriorate gradually over time. The chemical degradation is due to the sodium diffusing through the carbon cathode and the accompanied reactions leading to deterioration. The degradation mechanisms are different in the gas zone, the top part of the block and in the electrolyte zone, the bottom part of the block.

A proposed path for diffusion of sodium into the sidewall block is shown in Figure 6.21[8]. Sodium will diffuse through the carbon block, ramming paste (big joint) into the sidewall block materials and reacts with the Si_3N_4 binder together with oxidizing gases coming from the pot and the top of the sidewall block since the pot is not air-tight. The degradation product is Na_2SiO_3 at reducing conditions with the excess sodium, or a mixture of Na_2SiO_3 and $Na_2Si_2O_5$ at less reducing conditions and a lower activity of Na. The gradually accumulated solid products will cover the pore surface, narrow the pores channels and fill up most of the

[8]As demonstrated in Section 8, the dominant diffusion process of sodium in the whole lining structure is the solid phase diffusion in the carbon cathode, ramming paste (big joint) and gas phase diffusion in the sidewall block.

open pores and reduce the open porosity of the sidewall block. The reduction in porosity will retard the sodium gas diffusion further into the sidewall block. The autopsies of the spent sidewall block demonstrated that the sodium did not diffuse through the whole sidewall block and was only infiltrated in a limited area after long time operation. It is proposed that this is due to the chemical reactions, and the transport mechanism in the electrolyte zone is reaction controlled diffusion. The reactions significantly reduce the diffusion rate of sodium gas. Finally, the pot gas consisting of oxidizing gases (CO_2, CO), fluoride gases ($NaAlF_4$, HF) and water steam (H_2O), as well as the air from the leakage on the top, could react with the sidewall block to produce Si_2ON_2 at highly reducing conditions and cristobalite at less reducting conditions, and SiF_4(g) and N_2(g) at the top. The reaction undergoes active oxidation. The oxidation in the gas zone is preferred to α-Si_3N_4 since the needle structure of α-Si_3N_4 has higher surface area compared to β-Si_3N_4 rods. The reaction between HF and the Si_3N_4 binder as well as the oxide products will over time destroy the binder and cause detachment of the large SiC grains as observed in the gas zone of the sidewall blocks.

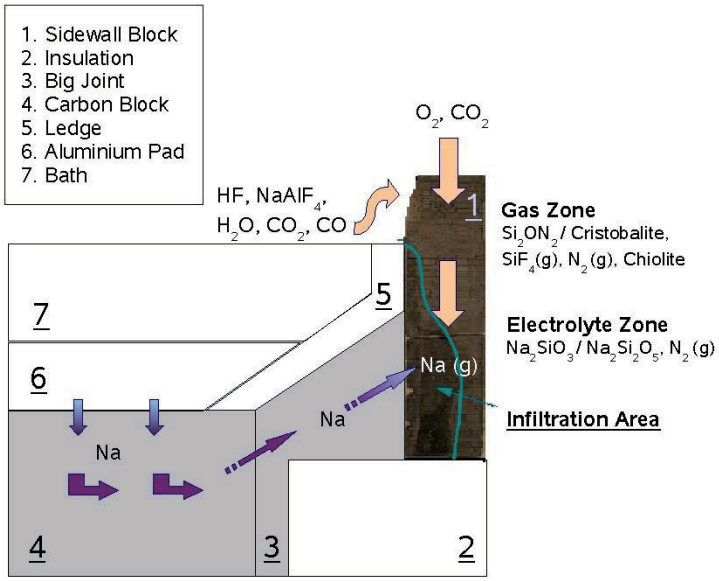

Figure 6.21: A schematic overview of proposed route of gases diffusion (not in scale).

The amount of the degradation phases does not follows the sequence of the age. That means other factors like operation condition and cell design have also an influence on the degradation. The thermal history in the cell is therefore proposed

to be important for the aging.

6.3 Conclusion

The present study has demonstrated that Si_3N_4 bonded-SiC sidewall block materials in aluminum electrolysis cells are chemically degraded due to oxidation of the fine grained Si_3N_4 binder. Degradation in the upper part (gas zone) can be described as selective oxidation, preferentially the needle-like α-Si_3N_4, by oxidizing gases (air or CO/CO_2) resulting in the formation of Si_2ON_2 or cristobalite. In the lower part of the sidewall block oxidation was observed to be influenced by the presence of sodium and the products were Na_2SiO_3 or a mixture of Na_2SiO_3 and $Na_2Si_2O_5$. The formation of the sodium silicates reduced the open porosity and increased the density accordingly. The formation of Si_2ON_2 and Na_2SiO_3 and the possible transformation of α-Si_3N_4 to β-Si_3N_4 in the spent block at the age of 270, 604, 1569 days all point to reducing conditions in the sidewall block. The formation of cristobalite and $Na_2Si_2O_5$ in the spent block at the age of 1767 days points to less reducing conditions or a higher oxidation potential.

Chapter 7

Thermal Properties of the Virgin and Spent Sidewall Block

7.1 Measurements

7.1.1 Thermal Expansion

The thermal expansion of the virgin and spent Si_3N_4-bonded SiC materials are shown in Figure 7.1. There was almost no difference between the sample from the area close to the surface of the virgin block and that from the center. The thermal expansion of the sample from the gas zone of the spent block was slightly higher compared to the virgin samples, while that from the electrolyte zone was considerably higher. The mismatch of the thermal expansion of the gas zone and the electrolyte zone of the block may contribute to the formation of cracks in the middle part of the block during the cooling after the cell shuts down, which is often observed in autopsies [113].

7.1.2 Thermal Conductivity

Virgin Block

The thermal conductivity of the virgin blocks can vary as shown in Figure 7.2. It is evident that the thermal conductivity of the center part material is higher than the material close to the surface of the block. The surface of the blocks with

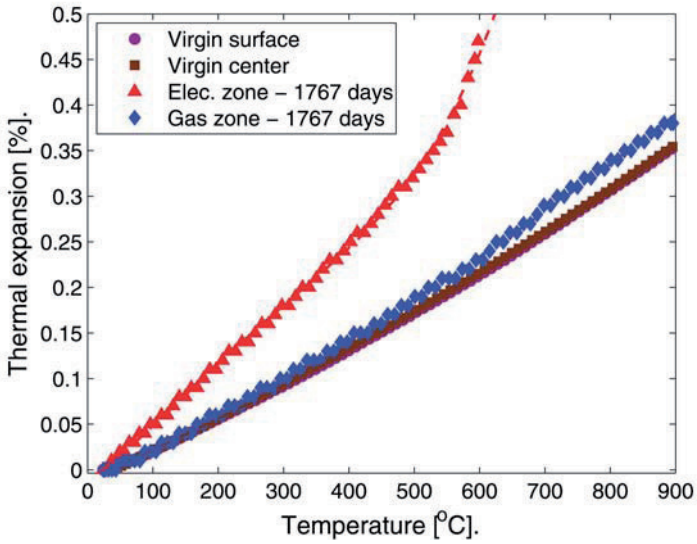

Figure 7.1: Thermal expansion of the virgin and the spent Si_3N_4-bonded SiC materials as a function of temperature. The dashed lines are curves fitted to the data using the 2nd polynomial function.

lower apparent porosity and higher density (Table 5.2) has around 10 W/(mK) lower thermal conductivity than their bulk counterpart. Generally the decrease in porosity will increase the thermal conductivity of the material. This implies that the apparent porosity is not the most important factor for the thermal conductivity of the Si_3N_4-bonded SiC materials. The variation of the thermal conductivity among the virgin blocks can neigher be explained by the variation in the phase content of α-Si_3N_4, β-Si_3N_4, SiC, nor the α/β ratio.

Spent Block

The thermal conductivity of the samples from the electrolyte zone of a spent sidewall block at the age of 1767 days is depictured in Figure 7.3. The thermal conductivity of a virgin material from the same supplier is shown for comparison. The measurements demonstrate that the thermal conductivity of the electrolyte zone of the spent sidewall had decreased significantly due to the degradation, despite a reduction of the porosity from 13-16 vol% down to 2-3 vol%. At room temperature, the thermal conductivity was reduced by 33% from 36 to 24 W/(mK), while at 500 °C the reduction was 52% from 23 to 11 W/(mK).

The thermal conductivity of the samples from the gas zone of the spent sidewall

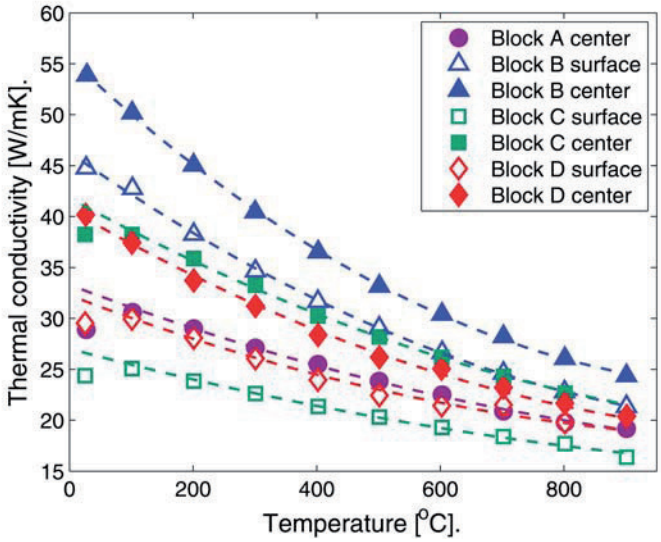

Figure 7.2: Thermal conductivity of the virgin sidewall block up to 900 °C. The dashed lines are curves fitted to the measured data using the equation k=a/(T+b).

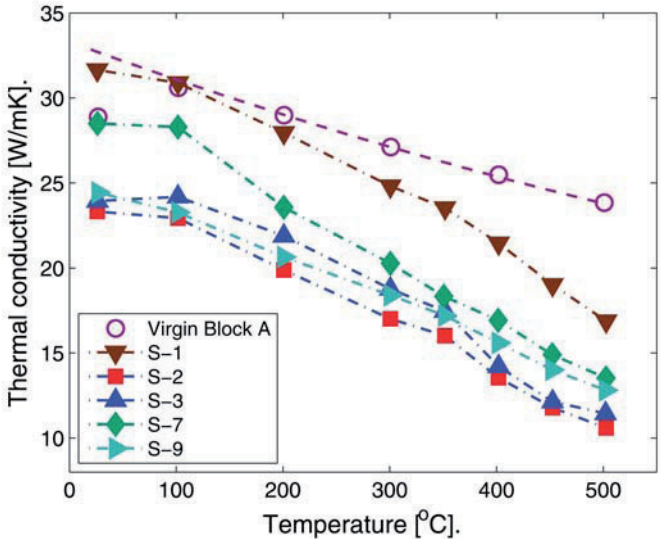

Figure 7.3: Thermal conductivity of samples from the electrolyte zone of the sidewall block at the age of 1767 days up to 500 °C. Measurement for a virgin sample is included for comparison.

block is shown in Figure 7.4. It can be seen that the thermal conductivity decreased dramatically as well, and was as low as 13 W/(mK) at room temperature and 10 W/(mK) at 500 °C. The reduction relative to the virgin material was 64% and 72% respectively. It was difficult to prepare a sample from the region close to the surface of the block towards the ledge where SiC grain detachment was observed. The thermal conductivity of this part is expected to be considerably lower than the value measured above due to the anticipated high porosity and lack of physical contact between the coarse SiC grains.

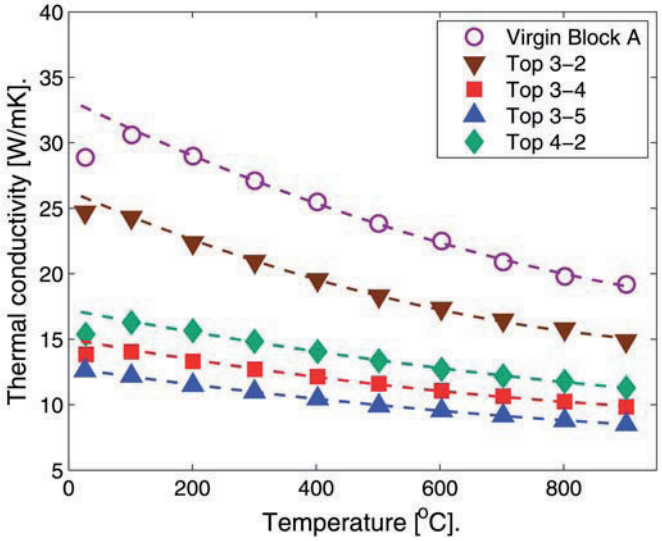

Figure 7.4: Thermal conductivity of samples from the gas zone of the spent sidewall block at the age of 1767 days up to 900 °C. Measurement for a virgin sample is included for comparison. The lines are curves fitted to the data using the equation k=a/(T+b).

The variation of the thermal conductivity with respect to the amount of the degradation phase and the apparent porosity in the electrolyte zone and the gas zone of the spent block is shown in Figures 7.5 and 7.6 respectively. The thermal conductivity in both regions was clearly reduced with increasing porosity.

In the electrolyte zone, as shown in Figure 7.5, the thermal conductivity seems to decrease with increasing amount of the degradation phases sodium silicates. In the gas zone, as shown in Figure 7.6, the relation between the amount of the degradation phase cristobalite and thermal conductivity is not evident.

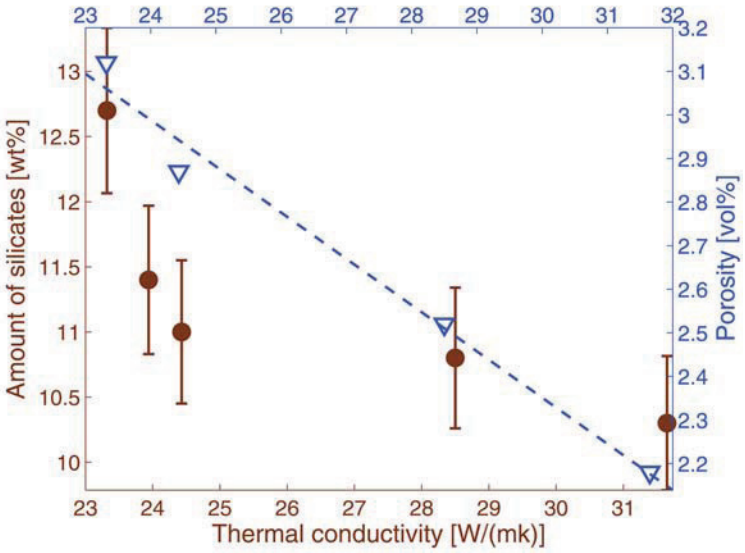

Figure 7.5: Thermal conductivity variation with respect to amount of sodium silicates and apparent porosity in the electrolyte zone of the spent block at the age of 1767 days. The dashed line is the curve fitted to the data using linear relation.

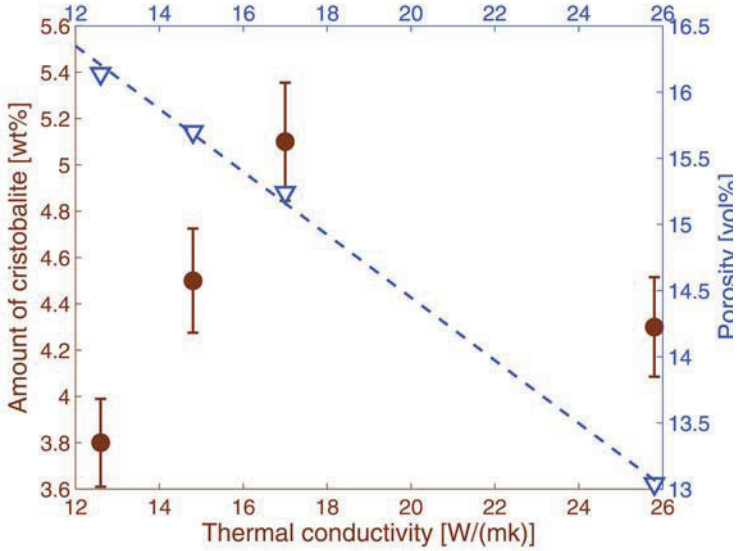

Figure 7.6: Thermal conductivity variation with respect to amount of cristobalite and apparent porosity in the gas zone of the spent block at the age of 1767 days. The dashed line is the curve fitted to the data using linear relation.

7.2 Discussion

7.2.1 The Effect of the Microstructure of the Silicon Nitride Bonded Silicon Carbide Composite

Si_3N_4-bonded SiC sidewall blocks consist of coarse SiC grains (mm scale) and a fine grained (submicro scale) porous binder which contains two polymorphs of Si_3N_4 (α-Si_3N_4 and β-Si_3N_4). The content of SiC and the porous binder is 63-69 vol% and 37-31 vol% respectively in block A to D. In the binder, the content of the nitride phase and the pore is 49-61 vol% and 51-39 vol% respectively. In the nitride phase, α/β ratio varies from 0.02 to 19.3. The α/β ratio is clearly not detrimental for the thermal conductivity of the sidewall blocks. This is also expected since the thermal conductivity of both phases is high.

Compared with the high intrinsic thermal conductivity of α-Si_3N_4, β-Si_3N_4 and SiC single crystal shown in Table 7.1, the bulk composite has a low effective thermal conductivity. The measured thermal conductivity of the virgin block is 27 to 55 W/(mK)[1].

Table 7.1: Intrinsic thermal conductivity of single crystal materials and the value used in the analytical calculation and simulation. Unit: [W/(mK].

Phase		Intrinsic therm. conductivity	Ref.	Value applied in calculation
SiC	3C	360	[114]	407 (average)
SiC	4H	370		
SiC	6H	490		
Si_3N_4	α	70	[115]	70
Si_3N_4	β	250		250

Since the thermal conductivity of the SiC grains are high, the thermal conductivity of the Si_3N_4 porous binder should be considerably lower in order to explain the measured low thermal conductivity of the sidewall block material. The calculated effective thermal conductivity as a function of the amount of different binders performed by a computer simulation is shown in Figure 7.7[2].

The 3D geometry is given in Figure 7.7(a), where SiC grains are embedded in a homogeneous binder. In the simulation, the thermal conductivity of the binder has been chosen as equal to the thermal conductivity of α-Si_3N_4, β-Si_3N_4, and

[1] Thermal conductivity in this section refers to the thermal conductivity at room temperature.
[2] All the computer simulations are done by using COMSOL 3.5a.

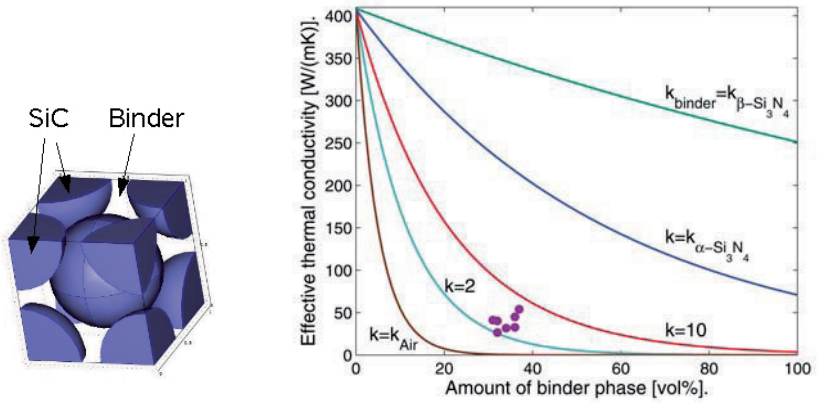

(a) 3D geometry. (b) Effective thermal conductivity of bulk material.

Figure 7.7: Effective thermal conductivity of bulk material as a function of the amount of different binders with different thermal conductivity. Calculated by a computer simulation using COMSOL 3.5a [93]. The filled circles are the measured thermal conductivity of the virgin materials.

air[3]. In addition, two simulations using the thermal conductivity of the binder equal to 10 and 2 were also performed. According to the simulation, thermal conductivity of the binder was estimated to be 2-10 W/(mK). It is proposed that such low thermal conductivity is explained by the influence of the microstructure, such as grain boundary resistance and pore shape and orientation (X factor) of the pores, and not by only consideration of the phase composition and the apparent porosity.

To calculate the effective thermal conductivity of the Si_3N_4-bonded SiC porous material analytically, one single model or equation is not sufficient. The principle for the analytical calculation and the geometrical model of the material in different scales are illustrated in Figure 7.8. kI, kII, kIII and kV are 3 calculation routes, in which kIII and kV are similar in principle. Detailed descriptions are as follows.

The thermal conductivity of α- and β-Si_3N_4 nitride mixture in the binder is estimated by the geometrical mean method as Equation (3.4), that for the mixture of SiC grain and the porous binder is calculated by the Maxwell model as Equation (3.3). For better understanding, an estimation of the thermal conductivity of the sample from the center area of Block B is shown in Figure 7.9 as an example. kI to kIV in Figure 7.9 represent the estimation illustrated in Figure 7.8. The intrinsic

[3]Thermal conductivity of air is 0.0026 W/(mK) [69].

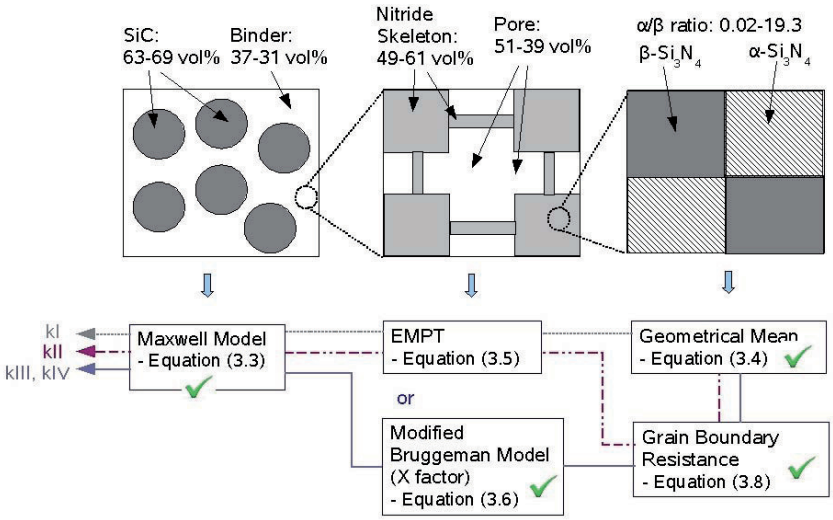

Figure 7.8: Simplified geometrical model of the composite material and the principle of the thermal conductivity calculation. kI, kII, kIII and kV are 3 calculation routes.

thermal conductivity of each phase was used in the calculation.

Referring to the figure, by considering only the porosity using effective medium percolation theory (EMPT) as Equation (3.5), which is the curve kI in the Figure 7.9, the calculated effective thermal conductivity is far too high compared with the measurement. Hence, other microstructure related factors must be taken into consideration, which are grain boundary resistance (gb) and pore shape, orientation (X factor).

For ceramic materials with small grain size like nitride grains in the binder of Si_3N_4-bonded SiC material, the grain boundary resistance could be relatively high. The overall grain boundary resistance (nR_{int}) of the samples from virgin blocks can be estimated from the interceptions of the curves in Figure 7.10 according to Equation (3.8). By taking into account grain boundary resistance, see curve kII in Figure 7.9, the effective thermal conductivity can be reduced significantly. However, it is still not low enough to describe the measured thermal conductivity.

For the porous binder, characterized by the complex pore system, the influence of pore shape and its orientation towards the heat flux (X factor), as shown in Equation (3.6) and (3.7), can not be neglected . The calculations in Figure 7.9 (curve kIII and kIV) demonstrate that increasing the X factor will reduce the effective

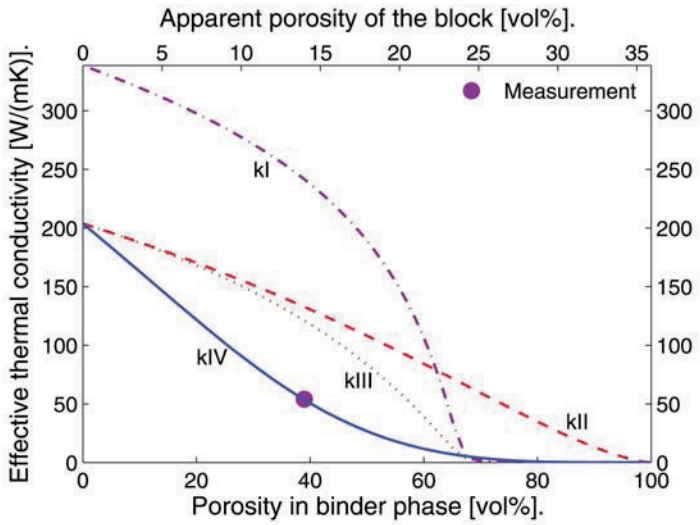

Figure 7.9: The effective thermal conductivity of the sample from center part of Block B as a function of porosity, kI: only porosity (EMPT), kII: porosity and grain boundary resistance (gb), kIII, kIV: pore shape and orientation (X factor equal to 1.5 and 3.9 respectively) and grain boundary resistance (gb).

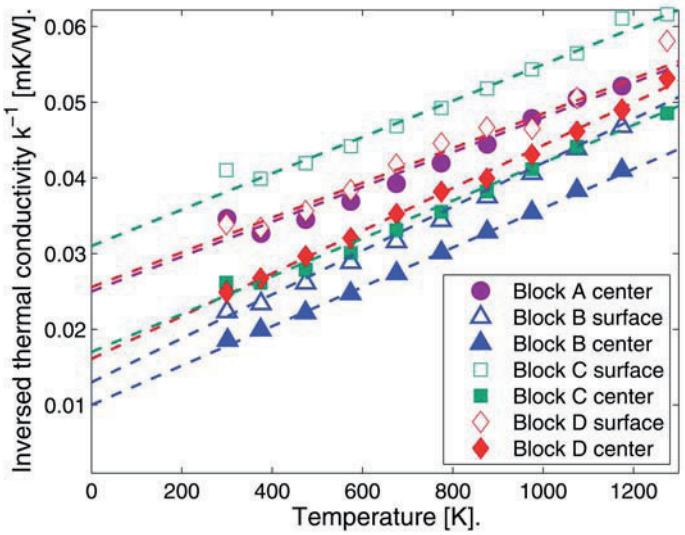

Figure 7.10: Inverse thermal conductivity of samples from virgin blocks as a function of temperature. The lines are curves fitted to the data using linear relation.

thermal conductivity correspondingly. For this material, the X factor is found to be close to 3.9 (curve kIV). According to Cernuschi **et.** *al* [87], this value is corresponding to a pore system with randomly oriented lamellae pores or cylindrical pores oriented perpendicular to the heat flux.

The effective thermal conductivity of the samples from all the virgin blocks and the gas zone of the spent block can be calculated by the same principle as route kIII and kV in Figure 7.8. The calculations show good fit to the measurement. The grain boundary resistance and X factor calculated for the samples from all the virgin blocks and the gas zone of the spent block are summarized in Table 7.2. The calculated thermal conductivity of the porous binder is between 2-10 W/(mK).

Referring to Table 7.2, the grain boundary resistance varies significantly among the samples, while that of the samples from the area close the surface of the virgin blocks is always higher than that from the center. The samples from the gas zone of the spent block have even higher grain boundary resistance than those from the virgin blocks. The measured thermal conductivity data and its relation to the overall grain boundary resistance are shown in Figure 7.11. The increasing grain boundary resistance will reduce the thermal conductivity of the Si_3N_4-bonded SiC materials and it follows the same trend as expected theoretically, see Figure 3.4. Since the reduction in the grain size will increase the number of grains per unit length and hence the overall grain boundary resistance nR_{int}, the reduction in the thermal conductivity of these materials can reflect the reduction in the grain size. The grain size in the gas zone of the spent block might be smaller than that in the virgin block, and the grain size in the surface of the virgin block is smaller than in the center. That is in agreement with the microstructure found by SEM, see Figure 6.12. The sample from the area close to the surface of the virgin block has finer needle crystals than those from the center. Moreover, from the gas zone of the spent block, even thinner fibers were observed.

To conclude, due to the variation in microstructure, the area close to the surface of the virgin blocks has lower thermal conductivity than that from its center. Furthermore, the top part of the spent block has lower thermal conductivity than the virgin blocks. The effective thermal conductivity of the Si_3N_4-bonded SiC materials is highly dependent on the microstructure evolution both during fabrication of virgin block and also due to the degradation of the materials during the operation of the cell.

Table 7.2: Grain boundary resistance (gb), X factor and calculated thermal conductivity of the Si_3N_4-bonded SiC materials and its binder phase. [1]: Surface towards the steel shell. [*]: extrapolated data from Figure 7.2 and 7.4.

Sample		**k_measured**	**gb resistance ($\times 10^{-2}$)**	**X facor**	**k_binder calculated**	**k_eff calculated**
		[W/(mK)]	[(mK)/W]		[W/(mK)]	[W/(mK)]
Block A	Center	32.7*	2.5	3.2	5.7	32.7
Block B	Surface	44.8	1.3	3.8	8.0	45.0
	Center	53.9	1.0	3.9	10.0	52.6
Block C	Surface	26.6*	3.1	3.6	3.9	26.8
	Center	41.0*	1.7	3.4	6.0	41.1
Block D	Surface	31.7*	2.6	2.8	5.1	31.6
	Center	40.1	1.6	2.6	6.1	40.0
1767 days	Top 3-2[1]	25.8*	3.0	3.6	4.5	26.5
- gas zone	Top 3-4	14.8*	5.9	3.2	2.8	14.8
	Top 3-5	12.6	6.6	3.3	2.4	12.5
	Top 3-4	17.0*	5.1	3.3	3.4	17.8

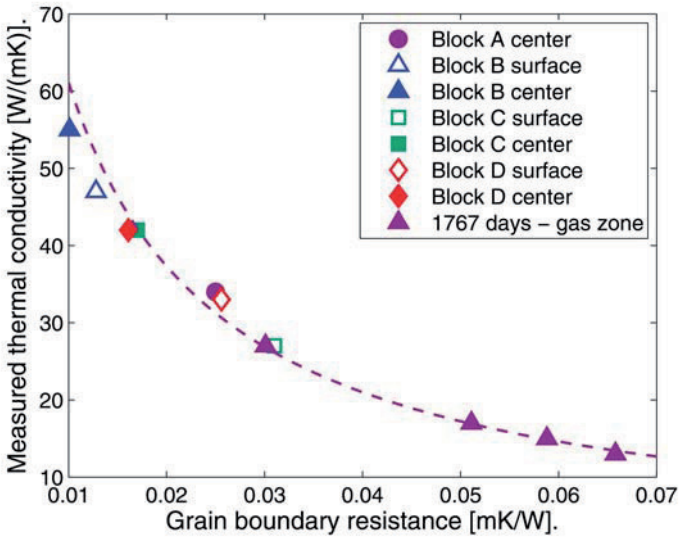

Figure 7.11: Thermal conductivity variation with grain boundary resistance. The dashed line is the curve fitted to the data using relation y=1/(a×nR+b).

7.2.2 Thermal Insulating Layer in the Spent Block

The large reduction in the thermal conductivity in the electrolyte zone of the spent block is unexpected since the apparent porosity was reduced significantly by the formation of sodium silicates. This can neither be explained by grain boundary resistance.

It is proposed that the reduction in the thermal conductivity is due to another microstructure related phenomenon: thermal insulating layer covering the grains. As can be seen from SEM-image (Figure 6.11(c)), a thin layer of silicate surrounds the SiC grains and the reduction in the thermal conductivity is shown to be related to the increasing amount of sodium silicates (see Figure 7.5). It is proposed that this thin layer with low thermal conductivity, shown in Table 7.1, can act as a thermal insulating layer which blocks the heat transfer path and reduces the effective thermal conductivity of the sidewall blocks.

If there is no resistant silicate layer, the thermal conductivity of the binder will decrease slightly when part of Si_3N_4 is consumed to form sodium silicate and the pores are filled by sodium silicate, called volume effect. However, the decrease is not large enough to explain the low thermal conductivity in the electrolyte zone. The thermal conductivity of the virgin Block A3 is 32.7 W/(mK), while that of

S3 in the electrolyte zone is 23.9 W/(mk), for example. To meet this change, the thermal conductivity of the binder phase should be reduced from 5.7 to 3.8 W/(mk) estimated by the Maxwell model. The reduction is around 33%. The volume effect can give only around 10% reduction in the thermal conductivity estimated by computer simulation using the geometry in Figure 7.12. The thermal conductivity of sodium silicate is 0.5 W/(mK) [116].

Computer simulation was used to demonstrate the influence of the thermal insulating layer. A 3D geometry representing the porous binder is shown in Figure 7.12 together with temperature distribution and heat flux stream line calculated by the computer simulation. The simulation demonstrates that most of the heat is conducted through the solid Si_3N_4 skeleton simply because air has considerably lower thermal conductivity and acts as a thermal insulator.

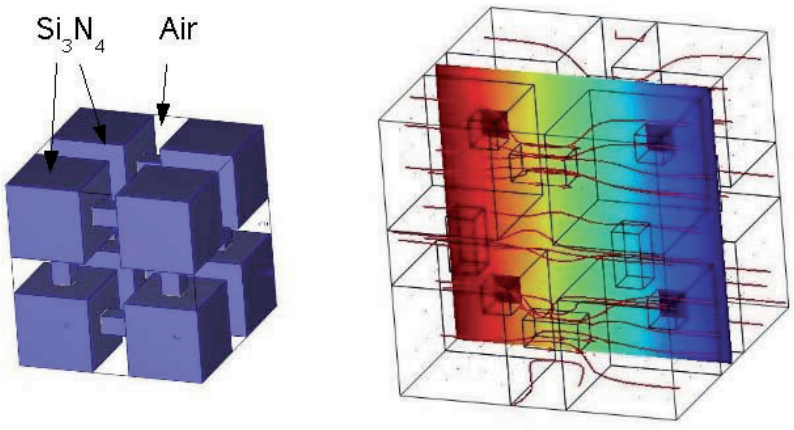

Figure 7.12: 3D geometry of the binder phase, temperature distribution and heat flux stream line by computer simulation by using COMSOL 3.5a [93].

To evaluate the influence of the thermal insulating layer, a 3D geometrical model of the binder after degradation was constructed as shown in Figure 7.13, where pores were filled with sodium silicate and sodium silicate layers were formed at the interface of the nitride skeleton joins.

The influence of the thickness of the thermal insulating silicate layer on the thermal conductivity of the binder is shown in Figure 7.14. When the silicate layer is formed on the skeleton joins the thermal conductivity of the binder reduces with increasing thickness of the layer. The resistance layers, which are perpendicular to the heat flux, block the heat transfer path and will have significant influence

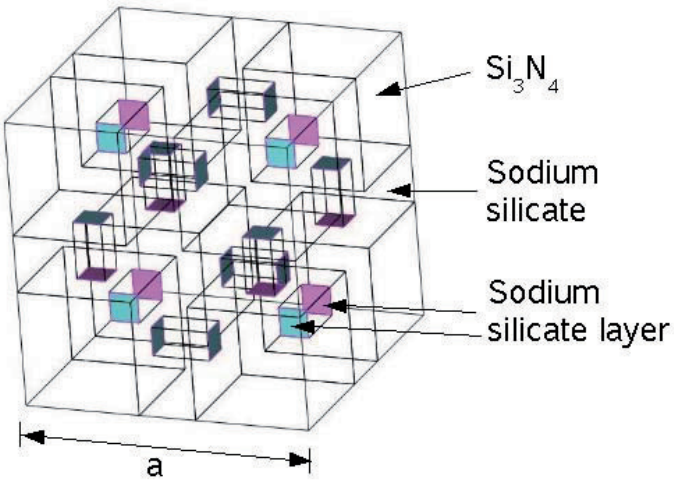

Figure 7.13: 3D geometry showing the binder after degradation where pores were filled with sodium silicate and sodium silicate layer formed on the interface of the nitride skeleton joins.

on the effective thermal conductivity of the composite materials. The thickness of the resistant layer will increase with increasing amount of silicate phase and hence reduce the thermal conductivity of the composite material significantly.

To conclude, the reduction in the thermal conductivity in the electrolyte zone is due to both the volume effect and the sodium silicate thermal insulating layer and the latter is dominant.

7.2.3 The Influence of the Variation of the Thermal Conductivity on the Side Ledge

The reduction in the thermal conductivity of the spent sidewall block will have an impact on the thickness of the side ledge. The heat flux and temperature distribution in the cell is shown in Figure 7.15[4]. The figure demonstrates that the heat is

[4]The parameters used in the simulation are as follows. The heat transfer coefficient between the ledge and liquid bath is 780 W/m^{2}K [117]. k$_{Carbon}$=70 W/(mK), k$_{Insulation}$=0.19 W/(mK), k$_{Refractory}$=1.5 W/(mK), k$_{Ramming}$=10 W/(mK), k$_{Ledge}$=1.36-2.94 W/(mK) from 573K to 1173K [20], k$_{Mortar}$=0.4 W/(mK) [118] and k$_{SiC}$=23.84 W/(mK).

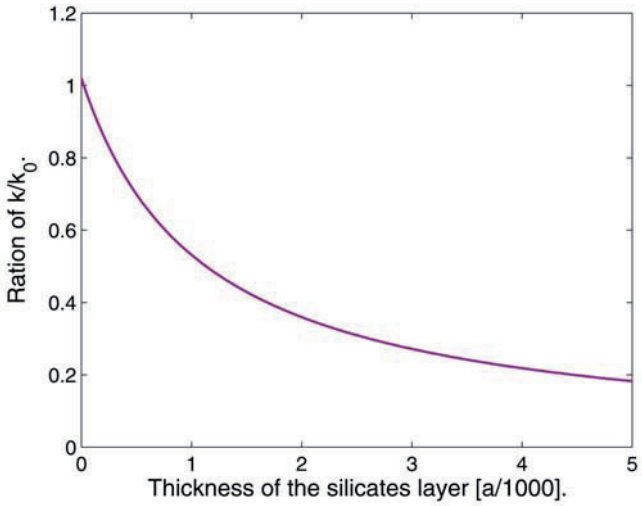

Figure 7.14: Effective thermal conductivity of the binder phase as a function of the thickness of the sodium silicate layer. *a* refers to the length in Figure 7.13. Calculated by computer simulation using COMSOL 3.5a [93].

traveling mostly through the sidewall block through the ramming paste (big joint). The thermal conductivity of the ramming paste (big joint) will have an influence on the heat flux through the sidewall block. When the thermal conductivity increases from 6 to 20 W/mK, the heat flux through the sidewall block can increase 26%.

Since less heat will transfer directly from the side ledge into the sidewall block, the influence of the thermal conductivity of the sidewall block is expected not to be significant. From the measurement the thermal conductivity of the sidewall block will reduce from 23.8 to 10 W/(mK) at 500 °C. In this case the heat flux through the sidewall block will be reduced by 6%. Assuming the total heat loss of the cell to remain unchanged, the thickness of the ledge reduces from 15 to 12 cm[5]. The thinner side ledge might increase the risk of exposure of sidewall block to molten bath or pot gas.

The reduction in the thermal conductivity of the sidewall block will also change the temperature distribution in the block. The simulated vertical temperature distribution along the sidewall block is shown in Figure 7.16. After degradation, the

[5]Due to the limitation of the calculation, the possibility of the change in super heat of the bath is not taken into condideration.

temperature along the surface of the sidewall block towards bath will increase by 50 °C.

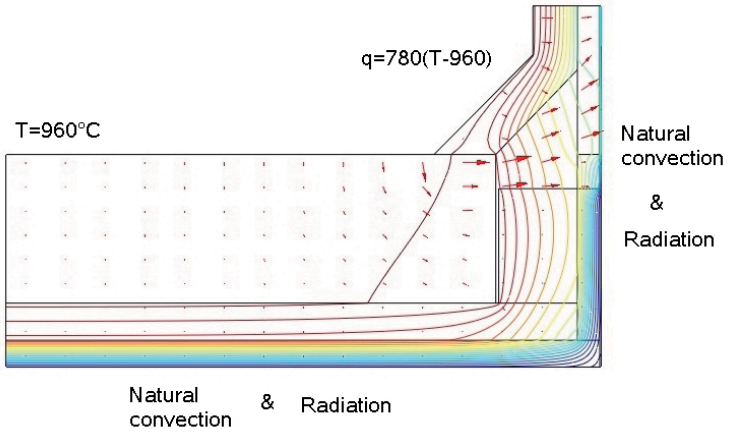

Figure 7.15: Heat flux in a half cell with ledge. Calculated by computer simulation using COMSOL 3.5a.

7.3 Conclusion

The area close to the surface of the virgin Si_3N_4-bonded SiC blocks with lower porosity and higher density was found to have around 10 W/(mK) lower thermal conductivity than their bulk counterpart. The thermal conductivity of the spent block was decreased significantly due to the degradation in the cell. At room temperature the thermal conductivity of the electrolyte zone of the spent block was reduced by 33% from 36 to 24 W/(mK), while at 500 °C the reduction was 52% from 23 to 11 W/(mK), despite the significant reduction in the porosity. The thermal conductivity of the gas zone of the spent block was decreased dramatically as well and below 15 W/(mK) at room temperature and 10 W/(mK) at 500 °C. Analytical models and computer simulation were applied to estimate the thermal conductivity of the Si_3N_4-bonded SiC porous composite materials. It is proposed that the low thermal conductivity of the Si_3N_4-bonded SiC blocks compared with the high intrinsic thermal conductivity of the single crystal materials is due to the influence of microstructure factors such as grain boundary resistance and pore shape and orientation and not only by consideration of the phase composition and the apparent porosity. The grain boundary resistance and pore complexity explain well the variation in the thermal conductivity of the virgin materials and

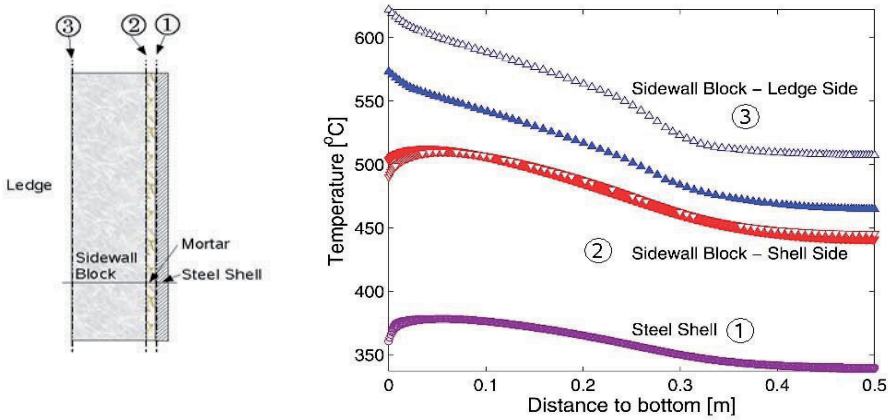

(a) Sidewall structure.

(b) Vertical temperature distribution along the sidewall layers. Open markers: k=10 W/(mK), filled markers: k=23.84 W/(mK).

Figure 7.16: Vertical temperature distribution along the sidewall layers. Calculated by computer simulation using COMSOL 3.5a.

the materials in the gas zone of the sidewall block. In the electrolyte zone of the spent sidewall block, the sodium silicate layers, which formed at the surface of the grains during the degradation, will act as the thermal insulating layer blocking the heat transfer path. This is proposed to be a main reason for the reduction in the thermal conductivity in this part. Finally, the effective thermal conductivity of the Si_3N_4-bonded SiC materials is highly dependent on the microstructure evolution both during fabrication of virgin blocks and the degradation of the materials during the operation of the cell. The reduction in the thermal conductivity of the sidewall block will cause a hotter surface of the block towards the bath and decreas the thickness of the side ledge.

Chapter 8

Sodium Diffusion in Cathode Lining

8.1 Sodium Mass Balance in the Cell

The amount of sodium accumulated in the lining materials should be equal to the total amount of sodium added to the cell subtracting the amount of sodium removed from the cell. A simplified sodium mass balance chart is shown in Figure 8.1. Here, only the contribution by metallic sodium is taken into account (neglecting the influence of the bath). The sodium mass balance in reality is in fact much more complicated. For example, ledge formation, emission, dust formation etc. will all influence the mass balance which is neglected. However, to a first approximation the simplified sodium mass balance is outlined and the main sources of sodium are believed to be included in this simplified consideration.

8.1.1 Source of Sodium

Soda ash Soda ash is added to the cell to compensate for the sodium loss into the lining materials and to maintain the optimal bath chemistry. The addition of soda is not a daily activity. The addition is intensive at the starting period. In a modern cell with graphitized cathode blocks, typically 1200 kg Na_2CO_3 (521 kg Na) is added during the first month [119]. In average, 300 kg Na_2CO_3 (130 kg Na) is added per year but this may vary [120].

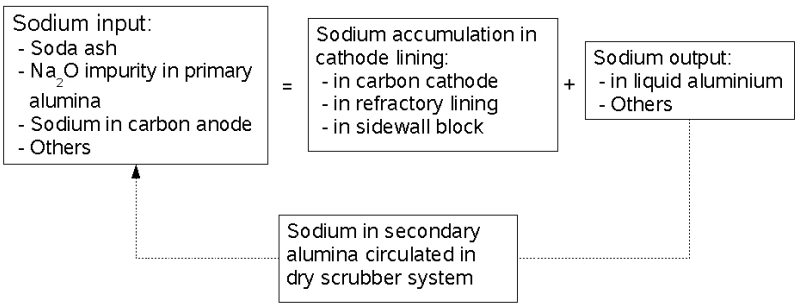

Figure 8.1: Simplified sodium mass balance in cell.

Primary Alumina Na_2O is supplied to the cell as the main impurity in primary alumina. The impurity level is about 0.3-0.45 wt% [1]. Considering a cell with 315 kA amperage load, 94% current efficiency (daily production of around 2.4 ton aluminium), the alumina addition is around 4579 kg/day according to Equation (8.1)

$$315 \times 0.94 \times 8.055 \times 1.92 = 4579 kg/day \tag{8.1}$$

where: 315 is amperage [kA], 0.94 is current efficiency, 8.055 is the maximum amount of aluminium produced per kilo amperage current [2], 1.92 [120] is 1.015×1.89 where 1.89 is the theoretical amount of Al_2O_3 needed to produce one unit aluminium, the factor 1.015 compensates the moisture and impurity in the primary alumina powders.

Setting the impurity level to 0.41 wt%, 18.8 kg Na_2O (13.9 kg Na) will be added to a cell per day. After significant time of operation, alumina is in fact the main sodium source in the cell.

Carbon Anode The carbon anode contains also around 25-250 ppm sodium [2]. During operation, carbon anodes are consumed and sodium is added to the bath. Anode carbon consumption is around 400-500 kg/ton aluminium [2]. Considering a cell with daily production around 2.4 ton aluminium, maximum 0.3 kg Na will be added to a cell per day.

Other Sources Additional sodium originating from secondary alumina, where sodium is absorbed from pot gas (bath evaporation) through the dry scrubbing system, can be neglected since the secondary alumina will be recycled back to the cell. There is also sodium impurity in AlF_3 (0.10-0.15 wt%) [1], but compared to other sodium sources, this source is quite small.

8.1.2 Sodium in Metal and Accumulation in the Cathode Lining

Molten Aluminium During operation, small amounts of sodium will be taken out of the cell with liquid aluminium, anode butts and dust. The sodium impurity in aluminium is between 60-130 ppm. For modern well-compensated cells having low flow rates, the sodium amount in aluminium is 100-200 ppm [1]. For a cell with daily production of 2.4 ton, 0.14-0.74 kg sodium will be removed from the cell per day.

Carbon Cathode For a semi-graphitic or a semi-graphitized cathode carbon, the saturation concentration of sodium is around 1-2 wt% [60]. The maximum sodium amount in the carbon cathode is estimated to be 545 kg (considering a cell size of 4m $\times$ 12m).

Refractory The sodium content in the refractory lining (contribution only from sodium penetration, neglecting bath) can be estimated based on the sodium element concentration at the reaction front. For example, in a cell operated for 300 days, the sodium penetration depth in the refractory layer is around 6 cm[1]. The sodium element concentration at the reaction front is around 9 wt% [55]. If only sodium (no fluoride) is present at the reaction front [51, 55], 9 wt% can be treated as the average sodium concentration in the reacted region of the refractory layer, which is contributed by the metallic sodium infiltration. In this case the sodium amount in the refractory layer is 524 kg[2].

Sidewall Block In the sidewall block, sodium reacts with oxidizing gases and the Si_3N_4 binder to form Na_2SiO_3. As presented in Chapter 6, the concentrations of Na_2SiO_3 are related to the operation condition or cell design instead of operation time only. In the later simulation, 10 wt% Na_2SiO_3 at the position close to the frozen bath is used, which is close to the data from the cell at the age of 604 days. The consentration is used to evaluate the reaction rate in the model and to estimate the amount of sodium diffusing into the sidewall block.

To summarize, considering a cell with daily production 2.4 ton aluminium, the sodium mass balance for the first year's operation can be estimated according to all the considerations mentioned above and is shown in Figure 8.2.

[1]The depth is for "lens-material", including "build-up" and reacted refractory [52].

[2]This number might be over estimated since the depth "lens-material" is the upper limit of the sodium penetration depth and the true depth might be shorter. In addition, the penetration depth is much less in the side where the temperature is colder than in the middle.

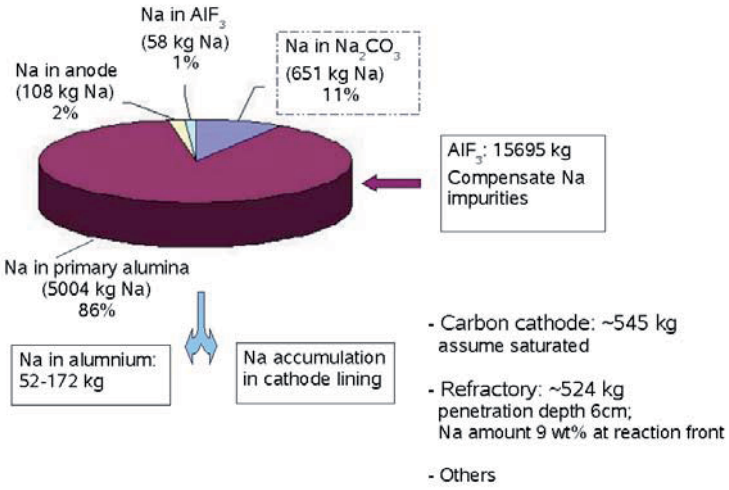

Figure 8.2: Sodium sources calculated for the first year's operation for a cell with the daily production of 2.4 ton aluminium and the dimension of 4m$\times$12m. Here the total Na_2CO_3 addition is considered as 1500 kg.

Although the Na_2O impurity in the primary alumina is the main source of sodium added to the cell (86 wt%), it will be compensated by the regular addition of AlF_3. With a daily addition of 43 kg AlF_3 per cell [120], 5380 kg Na will be compensated per year if the CR ratio is kept as 2.2. Therefore, sodium penetrating down to the cathode lining materials is compensated by the soda ash addition. The accumulation of sodium in the lining materials should be in the order of the magnitude of the amount of the soda ash added to the cell. From the second year, the soda addition will decrease due to the saturation of the sodium in the carbon cathode, which is confirmed by the simulations presented below.

8.2 Model Description and Boundary Conditions

8.2.1 Model Description

Due to symmetry, a half cell 2D transient diffusion and reaction model is applied in the simulation. The governing equation is expressed as Equation (3.13) based on Fick's 2nd law. The model geometry is shown in Figure 8.3. In the model, sodium formed at the carbon surface diffuses downwards through the carbon cathode into the refractory lining and also through the ramming paste (big joint) into

the sidewall block. Oxidizing gas diffuses from the top of the sidewall block. The diffusion process is accompanied by reactions in each layer. Therefore, in addition to the diffusion coefficients, the reaction rate in each lining material is also important to be implemented in the model, which is defined by taking into consideration the different degradation mechanisms in each layer according to the following arguments.

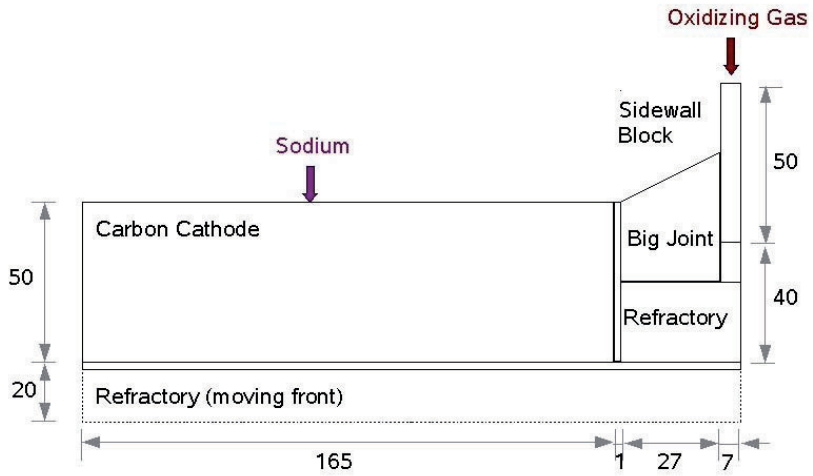

Figure 8.3: Half cell 2D geometry (short cross section), units in cm.

Sidewall Block

In the sidewall block, the sodium diffusion is to some degree governed by chemical reactions (Chapter 6). Sodium diffusing from the cathode reacts with Si_3N_4 binder together with oxidizing gases coming from top of the sidewall block. Sodium diffusion will slow down greatly by the comprehensive influences of the reactions. Reaction (6.8) is taken as the basis of the simulation. CO_2(g) in the reaction represents the oxidizing gases.

Assuming first order reaction, the reaction rate *R* can be defined by reaction rate constant *k*, and transient concentration of Na(g) and CO_2(g) as expressed by Equation (8.2)

$$R = -k \cdot c_{Na(g)} \cdot c_{CO_2(g)} \tag{8.2}$$

The concentration of the reaction product Na_2SiO_3 can be further calculated by

Equation (8.3)

$$c_{Na_2SiO_3} = \int_0^t \frac{1}{2} R dt = -\frac{1}{2} \int_0^t k \cdot c_{Na(g)} \cdot c_{CO_2(g)} dt \tag{8.3}$$

In the model, *k* is assumed to be constant and independent of temperature.

Carbon Cathode

In the carbon cathode, the Gibbs energy of the formation of intercalation compound C_xNa is small or positive [121]. The reaction can therefore be neglected and the infiltration of sodium in the carbon materials is diffusion controlled.

Refractory Layer

In the refractory lining, a sharp reaction front has been observed by autopsies. The reaction front divides the refractory layer into two parts: reacted part and intact part. The degradation process is diffusion controlled and reactions occur at the reaction front [9, 55]. A schematic drawing of the reaction front is shown in Figure 8.4. The reaction front is moving downwards over time.

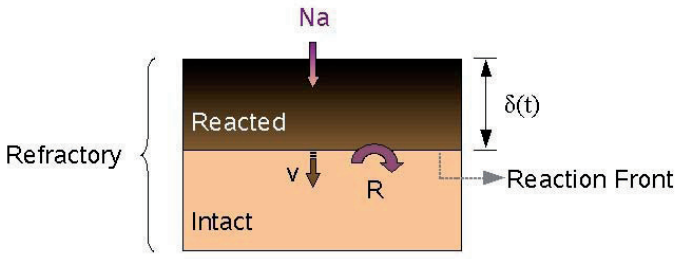

Figure 8.4: Moving reaction front in the refractory layer. *R* refers to the surface reaction.

In the simulation a moving boundary is introduced to represent the moving reaction front. The reaction taking place at the interface is assumed to be instantaneous meaning that the reaction rate is considerable faster than the diffusion rate, and diffusion is the rate limiting step. Assuming the molar amount of the reaction products is equal to the molar amount of sodium coming through the interface, the moving speed of the reaction front can be derived by Equation (8.4), which is

related to the sodium flux N_{Na}

$$\frac{d\delta}{dt} = \frac{N_{Na} \times M_{Na}}{f_{Na} \times \rho \times 1000} \tag{8.4}$$

in which δ is penetration depth [m], N_{Na} is the transient molar flux through the reaction front [mol/m^{2}s], f_{Na} is the mass fraction of sodium in the reacted refractory layer, set to 9 wt% in the present model [55], M_{Na} is the molar weight of sodium [g/mol], and ρ is the density of reaction product [kg/m^3]. Here the density used for the spent refractory block was 2623 kg/m^3 [20]. The calculation is based on the principle introduced by Slattery [122].

The diffusivity of sodium in the refractory layer is difficult to quantify due to the complex involvement of both diffusion and reaction. The diffusion constant depends strongly on both the temperature and the composition of the sodium aluminosilicate viscous melt formed in the refractory layer. Here sodium self-diffusion data in albite melt is used [78, 79]. Moreover, the temperature dependence of the diffusivity is applied to describe the slow down of the sodium diffusion at the colder region further down. The diffusion constant is assumed to be 1×10^{-9} m^2/s at the refractory upper surface (δ=0 m, temperature around 900 °C) and 1×10^{-10} m^2/s at the refractory bottom (δ=0.2 m, temperature around 800 °C). The diffusivity in between is calculated by the relation

$$log_{10}D = -5\delta - 9. \tag{8.5}$$

The presence of fluoride compounds would lower the viscosity of the sodium aluminosilicate significantly [123] and in such a way increase the diffusion rate. However, since no fluorine element was detected at the reaction front [51, 55], the above arguments for the diffusion constant in the refractory layer is believed to be reliable, and the sodium diffusion in the viscous melt is the rate limiting step.

8.2.2 Boundary Conditions

According to the two mechanisms describing the transportion of sodium in the carbon cathodes [61, 62], two sets of boundary conditions are implemented in the simulation accordingly. *Model 1* is based on gas phase diffusion in the carbon cathode and *Model 2* is based on solid state diffusion. In the sidewall block, gas diffusion is applied in both models, and in the refractory layer liquid diffusion is applied.

Model 1 Gas Phase Diffusion in Carbon Cathode:

Solheim **et** *al*. [124] reported that the partial pressure of sodium over the carbon surface was around 0.02 -0.03 atm. Sodium concentration can be calculated according to the ideal gas law. Boundary conditions and material properties for Model 1 are summarized in Table 8.1.

Model 2 Solid Phase Diffusion in Carbon Cathode:

Due to the fact that a concentration (atoms/molecules per unit volume) in the solid phase will be several orders of magnitude higher than that in the gas phase, the boundary condition, i.e. sodium concentration at carbon surface, will be different in the solid phase diffusion model. Here the sodium concentration has been set to 2 wt% (1435 mol/m^3), correcponding to the saturation concentration of sodium in the semi-graphitized materials [60].

Another factor which is important for Model 2 is the discontinuity in the sodium concentration at the ramming paste (big joint) - sidewall block interface due to the transition from solid to gas. It is assumed that the chemical potential of sodium in the solid phase is equal to that in the gas phase. At 850 K, which is the approximate temperature at this interface, the ratio of the sodium concentration in solid phase to gas phase is calculated to be 3×10^3. This means that at the ramming paste (big joint) - sidewall block interface the sodium concentration in the gas phase is around 3 orders of magnitude lower than in the solid phase.

The boundary conditions and materials properties for the two diffusion models are summarized in Table 8.1.

8.3 Results and Discussion

Influence of Reaction Rate on Diffusion

The simulation demonstrates that when the reaction rate in the sidewall block is high enough compared to the diffusion rate, the infiltration process can be slowed down by the chemical reaction. Referring to Figure 8.5, it is clear that with increasing reaction rate constant, the amount and the speed of sodium diffusing into the sidewall block is reduced.

Table 8.1: Boundary conditions and material properties for the models with gas phase diffusion and solid phase diffusion.

	Model 1	**Model 2**
Diffusion Type in Carbon Cathode	Gas Phase	Solid Phase
Diffusion Type in Sidewall Block	Gas Phase	
Diffusion Type in Refractory Layer	Liquid Phase	
Sodium Concentration at Carbon Surface [mol/m^3]	0.1994	1435
Concentration Discontinuity at Ramming Paste (Big Joint) - Sidewall Block interface ($c_{Na,s}/c_{Na,g}$)	/	3×10^3
CO_2 Concentration on top of Sidewall Block [mol/m^3]	7.8	
Density of Carbon Cathode [kg/m^3]	1650 [60]	
Density of Refractory after Degradation [kg/m^3]	2623 [20]	
Diffusivity in Carbon [m^2/s]	1×10^{-6} (fitting data)	1×10^{-8} (Table 2.4)
Diffusivity in Sidewall Block [m^2/s]	1×10^{-7} [19]	
Diffusivity in Refractory [m^2/s]	1×10^{-9} at δ=0 m 1×10^{-10} at δ=0.2 m $\log_{10}$D=-5$\times\delta$-9	
Moving Speed of the Reaction Front [m/s]	$N_{Na}\times9.74\times10^{-5}$	

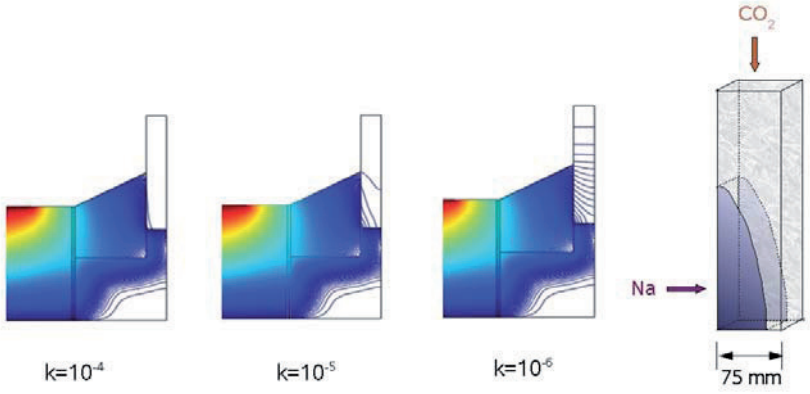

Figure 8.5: The influence of the reaction rate constant in the sidewall block on the sodium concentration profile. Simulation by using COMSOL 3.5a [93].

Mass Balance

In order to reproduce the Na_2SiO_3 concentration in the sidewall block observed in the autopsy (mentioned in Chapter 8.1.2), for Model 1 (gas phase diffusion in carbon) the parameters giving the best fit were a diffusion constant equal to 1×10^{-6} m^2/s in carbon and reaction rate constant equal to 4.8×10^{-4}. The diffusion constant was two orders of magnitude higher than reported data (see Table 2.4). For Model 2 (solid phase diffusion in carbon), the diffusion constant in carbon was taken from the report data (Table 2.4), and reaction rate constant found by simulation was 2.2×10^{-5}.

The sodium mass balance calculated by these two models is shown in Figure 8.6(a) and 8.6(b) respectively, where the amount of the total incoming sodium is equal to the amount of the sodium accumulated and reacted in all the layers.

Known from the aforesaid calculation for the sodium mass balance in the cell, the sodium addition is around 651 kg for the first year (365 days), which is several orders of magnitude higher than the amount found by the simulation using Model 1. Especially the sodium content in the carbon cathode is underestimated. It can therefore be concluded that the model with the gas diffusion in the carbon cathode is not realistic. The process for the sodium transportation in the carbon cathode is proposed not to be dominated by sodium vapor transport in the open porosity.

The sodium mass balance obtained by Model 2 is close to the estimated mass balance of the cell. Both the sodium supply and the sodium content in carbon cathode and refractory layer are in the same order of magnitude as the sodium

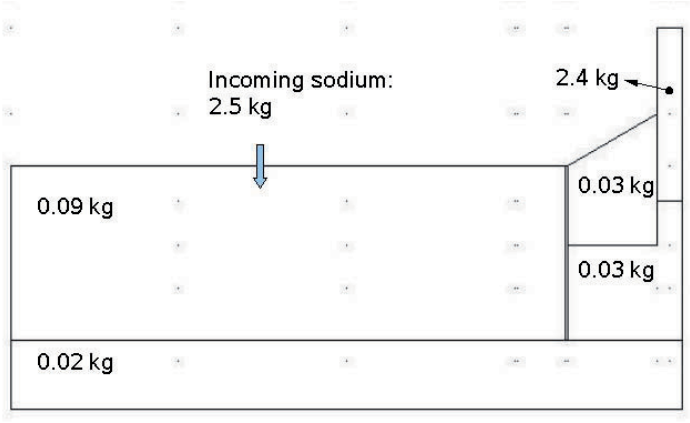

(a) Model 1.

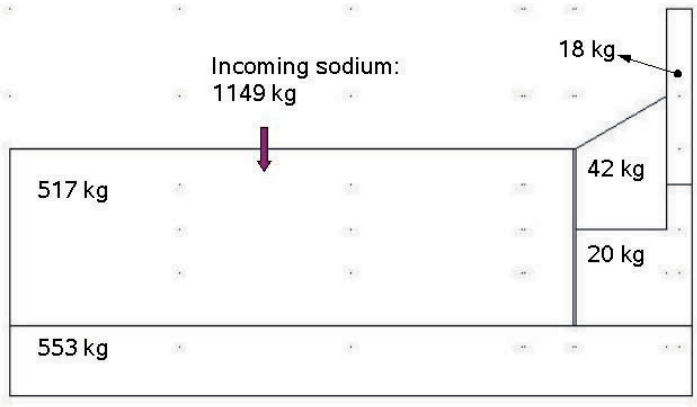

(b) Model 2.

Figure 8.6: Sodium mass balance after 604 days. Simulation by using COMSOL 3.5a [93]. Sodium amount is calculated by using a cell dimension of 4m $\times$ 12m.

mass balance estimated for an industrial cell. The concentration of the sodium silicate in the sidewall block is also in reasonable agreement with the autopsies (mentioned in Chapter 8.1.2). The diffusion process in the refractory layer is simplified, but still the simulated sodium content in the refractory is relatively realistic. Moreover, most of the sodium is accumulated in the carbon cathode and in the refractory. A relatively small amount of sodium goes to the sidewall block since the transport in the sidewall block is by gas phase diffusion.

Sodium Transportation in the Cathode Lining Materials

The sodium concentration distribution over the whole cathode lining obtained by Model 2 is shown in Figure 8.7. The concentration of sodium in the carbon cathode is 3 orders of magnitude higher than that in the sidewall block due to the transition from solid to gas at the interface.

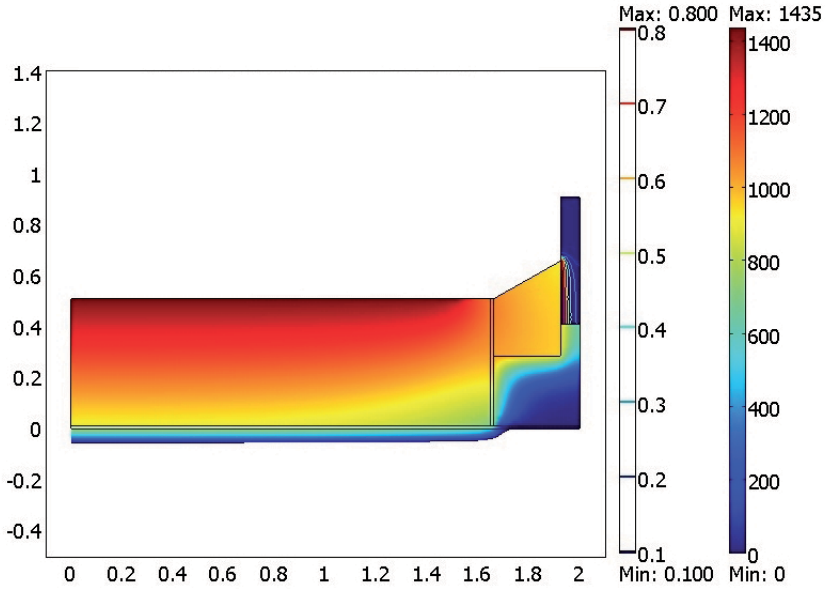

Figure 8.7: Sodium concentration surface/contour plot at 604 day. The scale bar for the sidewall block resulting from the gas phase diffusion is around 3 orders of magnitude lower than for the rest of the cathode lining where the solid/liquid phase diffusion is applied. Simulation by using COMSOL 3.5a [93].

The accumulation of the sodium content in the carbon cathode and the refractory layer versus time together with the total amount of the incoming sodium is shown

in Figure 8.8. During the first 2 months, the accumulation of sodium in the carbon cathode is fast and it slows down gradually when approaching saturation. After the first month, there is almost no sodium in the refractory layer, and it starts to build up gradually later on. After 550 days, the amount of sodium in the refractory layer is higher than that in the carbon cathode. Referring to the figure, the addition of sodium is intensive in the first two months, especially in the first month, which is in the agreement with the action in the industry [119,120]. The addition is mainly to compensate the sodium "loss" into the carbon cathode. The amount of sodium addition reduces significantly after 100 days, and most of the sodium addition is to compensate the sodium "loss" into the refractory layer. Therefore, in principle, by recording the amount of sodium (soda ash) added to the cell, it is possible to estimate how deep the sodium penetrates over time if the saturation concentration of sodium in the carbon cathode and the average sodium concentration in the refractory layer are known.

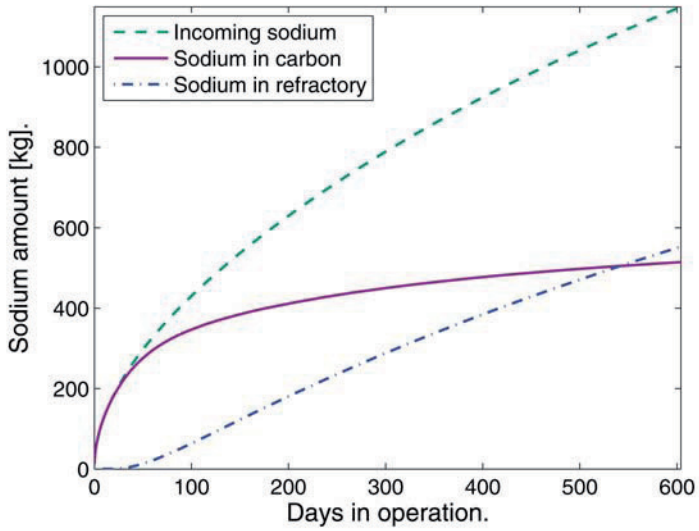

Figure 8.8: Sodium content in carbon as a function of time during 604 days. Simulation by using COMSOL 3.5a [93].

According to the simulation sodium starts to reach the carbon bottom after about 10 days. Sodium concentration at the carbon bottom as a function of time is shown in Figure 8.9. In the sidewall block, the simulation demonstrates that the sodium silicate starts to be formed after about 60 days operation. The concentration of sodium silicate at the position close to the frozen bath is shown in Figure 8.10.

The sodium silicate will accumulate in the lining during operation. It is important to foresee the amount of silicate as a function of time, since the sodium silicate results in a decreased thermal conductivity over time, which influences the thermal balance of the cell.

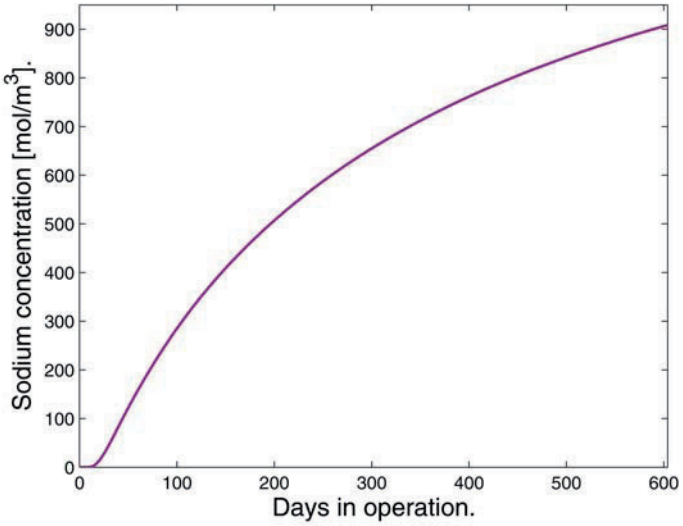

Figure 8.9: Sodium concentration at carbon bottom as a function of time. Simulation by using COMSOL 3.5a [93].

Moreover, by introducing the moving mesh (moving reaction front) in the refractory layer, the position of the reaction front as a function of time is possible to predict. Figure 8.11 shows the sodium infiltration depth as a function of time resulting from two simulations using different diffusion constant in the refractory layer. The diffusion constant for the first simulation (solid line in the figure) is 1×10^{-9} to 1×10^{-10} m^2/s in the temperature range 800 to 900 °C, while that for the second simulation (dashed line in the figure) is 1×10^{-9} to 1×10^{-10} m^2/s. The first is close to the sodium self-diffusion coefficient in the albite melt [78,79]. The penetration depth corresponding to the depth of "lens" material and reacted firebrick, measured by autopsies of the shut down cells [52], are also shown in the figure. These two depths can be treated as the upper and lower limits of the sodium diffusion depth.

The diffusion process in the refractory lining is complicated [20] and the penetration depth is difficult to estimate from the autopsies. The two extremes used in the present simulation might represent a reasonable interval for the true depth.

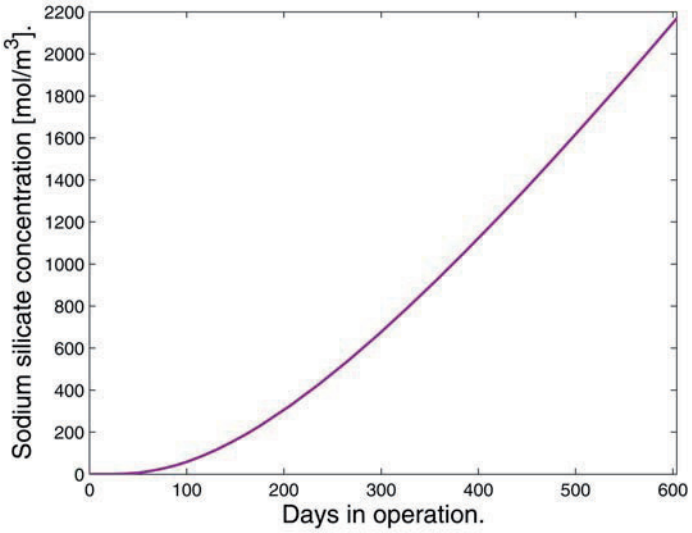

Figure 8.10: Concentration change of sodium silicate close to sidewall block-ramming paste (big joint) interface as a function of time. Simulation by using COMSOL 3.5a [93].

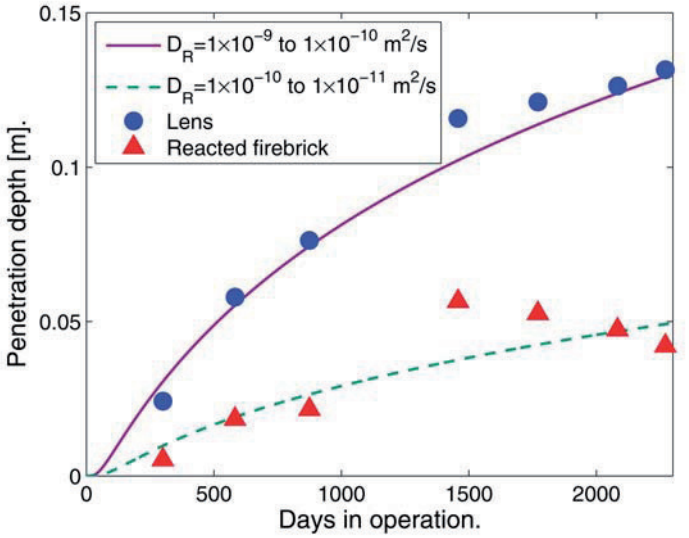

Figure 8.11: Sodium penetration depth as a function of time. D_R equal to 1×10^{-9} to 1×10^{-10} m^2/s is close to the sodium self-diffusion coefficient in the albite melt. Simulation by using COMSOL 3.5a [93]. Depth of "lens" and reacted firebrick is reported by Solheim **et.** *al* [52].

Using the diffusivity close to the sodium self-diffusion data in the albite melt, the simulated penetration depth fit the depth of the "lens" material, while when the diffusion constant was one order of magnitude lower, the penetration depth fit the depth of the reacted firebrick. If viscous diffusivity was used, which is 7-8 orders of magnitude lower than the self-diffusion coefficient [73], the penetration depth would be neglectable compared to the autopsy data. The simulations show clearly that the diffusion of sodium in the refractory lining is described reasonably well by the sodium self-diffusion in the molten albite like oxides.

Although the real diffusion process in the refractory is more complicated than described here, the simplified model simulates the time scale of the penetration depth in the refractory layer relatively good. The good agreement demonstrates that the sodium diffusion in the viscous layer at the reaction front is the rate limiting step of the diffusion process in the refractory layer.

Moreover, sodium penetrates fast in the early period of operation due to higher diffusion constant of sodium in the refractory and gradually slows down since the sodium front reaches colder regions in the refractory lining.

8.4 Model Application

Based on the simulation, the diffusion route of sodium is proposed in Figure 8.12. Solid state diffusion of sodium is dominated in the carbon cathode block and ramming paste (big joint), and gas phase diffusion is the main sodium transport mechanism in the sidewall block.

The simulation may also give an insight into the consequence of changing the material properties in the cathode lining, for example, the carbon cathode materials. The sodium concentration evolution at the bottom of the carbon block as a function of time is shown in Figure 8.13. If the carbon cathode material is changed from graphitic to amorphous carbon, it will take a longer time for sodium to reach the bottom, and over time, more sodium will be accumulated in the amorphous carbon than in graphitic material.

As mentioned previously the sodium silicate concentration in the sidewall block is not only a function of the operation time. It will also be related to the operation condition and the cell design. Sodium saturation concentration will vary with different types of carbon cathode, from 1 to 4 wt% or even higher [60]. The change in saturation concentration will change the boundary condition at the carbon surface. Assuming that the activity of sodium in the ramming paste (big joint)

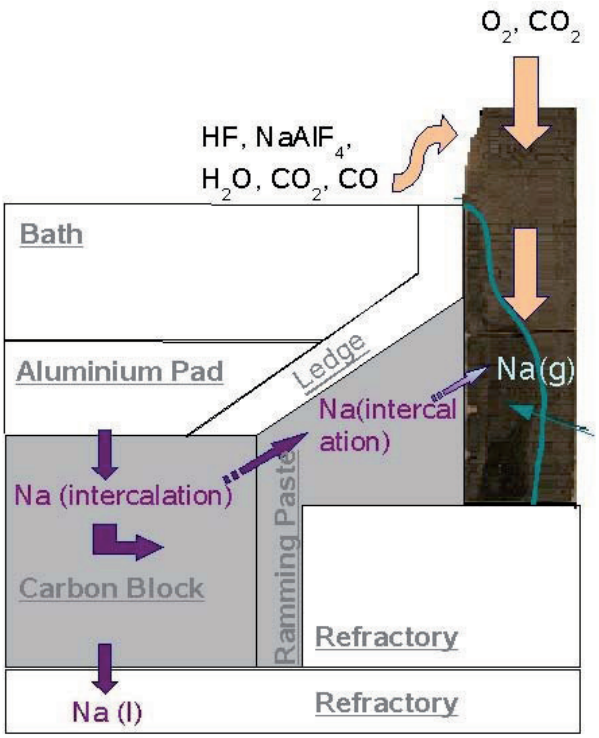

Figure 8.12: A schematic sodium diffusion route combining solid diffusion in the carbon cathode and gas diffusion in the sidewall block (not in scale).

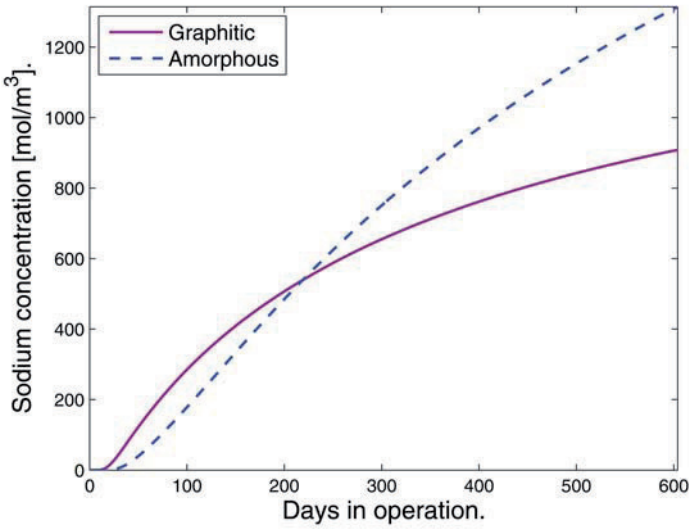

Figure 8.13: Sodium concentration at carbon cathode bottom. For graphitic: concentration is 2 wt%, D=1$\times 10^{-8}$ m^2/s. For amorphous: concentration is 4 wt%, D=1$\times 10^{-9}$ m^2/s. Simulation by using COMSOL 3.5a [93].

does not change, the ratio between sodium concentration in ramming paste (solid phase) and the concentration in the sidewall block (gas phase) remains constant. The simulation shows that the increase of the sodium concentration at the carbon surface (sodium saturation concentration in carbon cathode) gives a linear increase of the sodium silicate concentration in the sidewall block as shown in Figure 8.14. The change in cathode material will surely influence on the degradation of the sidewall block materials. Moreover, a change in the properties of the big joints between the carbon cathode and the sidewall block will also influence the degradation in the sidewall block since the activity coefficient of sodium in the ramming paste (big joint) determines the discontinuity of the sodium concentration at the ramming paste (big joint) - sidewall block interface. A higher activity coefficient of sodium in the ramming paste (big joint) results in a lower $c_{Na,s}/c_{Na,g}$ ratio, i.e. a higher concentration of sodium in the sidewall block as well as a higher concentration of sodium silicate, which indicates a more severe degradation of the sidewall block.

Finally, a stable sidewall block material is required in a high amperage cell due to both the requirements of the optimal thermal balance of the cell and the possibility to recover heat from the heat flux through the sidewall block. The possibility

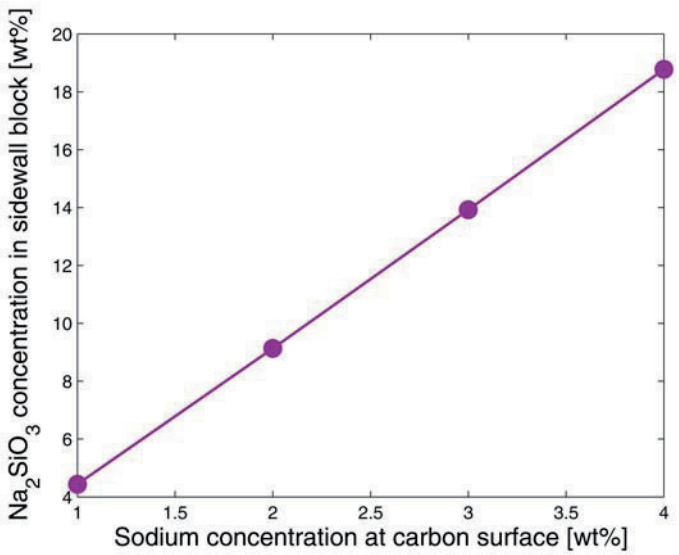

Figure 8.14: Sodium silicate concentration in sidelining as a function of sodium concentration at carbon surface during 604 days operation. Simulation by using COMSOL 3.5a [93].

to inhibit/reduce the sodium infiltration into the sidewall block is therefore of interest. The formation of sodium in cathode is inevitable due to the electrolysis process. However, since the aggressive bath components do not likely infiltrate the sidewall block, which is not the case in the refractory layer, it could be useful to add a diffusion barrier (like a steel plate or a chemical barrier) between the ramming paste (big joint) and the sidewall block. Without the molten bath, the barrier may survive a significant time and may block the sodium diffusion path and reduce the possibility for formation of sodium silicates.

8.5 Conclusion

The present simulations have demonstrated that in the carbon cathode the dominant diffusion process of sodium is solid state diffusion, while in the sidewall block the sodium diffusion is limited by the chemical reaction resulting in formation of sodium silicates. The simulations have also shown that changes in the properties of the cathode materials as well as the ramming paste (big joint) material will influence on the degradation of the sidewall block. Moreover, the simulation has demonstrated that sodium diffusion in the refractory lining is well

described by the self-diffusion of sodium in albite like molten oxides.

Chapter 9

Bath Flow in Porous Cathode Block

9.1 Introduction

Penetration of the bath into the refractory and thermal insulation layer is among the principal factors that determine the pot life. The time scale or rate of the bath penetration is, therefore, important to know. The bath penetrates first into the carbon cathode through the pore system. In this Chapter, the bath flow into the cathode materials is investigated by mathematical models considering the cathode and bath (Na_3AlF_6-AlF_3-Al_2O_3) properties both in macro-scale as permeability, bath density, viscosity and in micro-scale as pore structural (pore size distribution), wettability (contact angle), and surface tension of the bath.

9.2 Flow in Porous Media

At the macro-scale, according to Darcy's law as given by Equation (3.14), when the pressure drop, permeability, porosity of the porous media and the viscosity of the fluid are known, the velocity of the fluid through the porous media can be calculated.

The pressure drop over the carbon cathode is estimated to 9400 Pa, which is the weight of a 20 cm thick layer of the electrolyte and 20 cm thick layer of alu-

minium pad on top of the carbon block[1], the porosity of the carbon cathode is 23 vol% [60], permeability is 1 nP[2], and the bath viscosity is 2×10^{-3} Pa·s [1]. The infiltration velocity of the bath into the carbon cathode is in the order of 2×10^{-6} m/s. This means that the bath will travel 0.17 m per day and reach the bottom of the cathode (50 cm thick) after about 3 days. This calculation, however, does not take the wetting property of the carbon cathode material into consideration. The wetting properties and capillary pressure is proposed to have a significant influence on the bath infiltration phenomenon.

9.3 Capillary Force and Hydrostatic Pressure

At the micro-scale, the bath flow in the carbon materials can be described as micro-fluid in pores. The flow in a single pore is driven by a combination of capillary force and hydrostatic pressure. Hydrostatic pressure here refers to the total weight of the bath and metal pad on top of the carbon cathode, which attempts to push the bath into the pore channels.

Assuming pores in the cathode as cylindrical straight pores, the capillary force induced by surface tension can be derived by Young-Laplace equation and expressed as Equation (9.1)

$$\Delta p = \frac{2\gamma cos\theta}{a} \tag{9.1}$$

in which, Δp is the capillary pressure [Pa], γ is the surface tension of bath [N/m], a is the pore radius [m], and θ is the contact angle. The contact angle is a measure of the degree the liquid wets the solid surface.

For non-wetting materials, shown as Figure 9.1, the contact angle is higher than 90°, the capillary pressure is negative, meaning that the capillary force contributes to resist the fluid flow or push the fluid backwards along the pore walls. For wetting materials, the contact angle is lower than 90°. In this case the capillary force will drag the liquid along the pore walls.

As mentioned above the capillary pressure can be either a driving force or a resistance depending on the wetting property. The hydrostatic pressure on the carbon surface is always a driving force since it is pointing downwards along the penetration direction. At good wetting condition, certainly, the liquid will penetrate through the porous carbon materials. At poor wetting condition, however, the

[1]Density of the aluminium pad is 2.7 kg/m^3 [108], and that of the bath is 2.07 kg/m^3 [1].
[2]Gas permebility of graphitized carbon cathode is in the range of 1-5 nP [125]

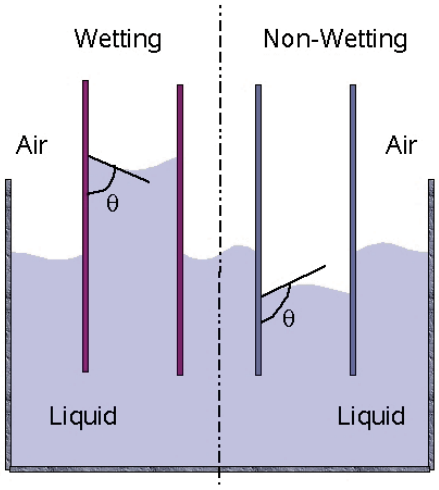

Figure 9.1: Illustration of capillary rise and fall resulting from a wetting and an non-wetting material respectively.

capillary force and the hydrostatic pressure are counteracted and the bath can not flow downwards if the capillary resistance is dominant.

The capillary pressure can be calculated by Equation (9.1) when the surface tension, pore diameter and contact angle are available. Thonstad **et.** *al* [1] have summarized the measured data for the surface tension, dynamic viscosity and density of cryolite based bath systems with various additions of fluorides and Al_2O_3. Some empirical formulas were also given. For a bath of Na_3AlF_6+9.5wt%AlF_3+ 5wt%Al_2O_3, which is similar to the industrial electrolyte, the surface tension can be described by the linear relationship as Equation (9.2)

$$\gamma = 193.4 - 0.0824 \times T \tag{9.2}$$

At 960 °C (temperature at carbon surface), the surface tension is 114 mN/m.

The density for the similar system can be calculated by Equation (9.3) which is obtained by rearrangement of an expression reported by Thonstad **et.** *al* [1]

$$2.983 - 8.466 \times 10^{-4} \times T - 3.373 \times 10^{-4} \times w^2(AlF_3) - 4.762 \times 10^{-3} \times w(Al_2O_3) \tag{9.3}$$

At 960 °C, the density for Na_3AlF_6+9.5wt%AlF_3+5wt%Al_2O_3 system is calculated as 2.07 g/cm^3.

Based on these data, the capillary pressure can be estimated as a function of contact angles and pore diameters. A contour plot of the capillary pressure is shown in Figure 9.2. In the figure, the negative number refers to the capillary resistance and the positive number refers to the capillary drag. At poor wetting condition (θ>90°), the capillary resistant force increases with increasing contact angle and decreasing pore diameter. It means that small pores have high resistance towards the bath flow. Only when the external force is higher than this resistance, the bath can penetrate into the pores. In the cell this external force is the total weight of the bath and aluminium pad above the carbon cathode, which is around 9400 Pa for a 20 cm thick layer of electrolyte and 20 cm thick layer of aluminium pad. Referring to the figure, the contour of -9.4 kPa divides the whole area into two regions. In the region below the pore will not be filled with the bath while in the region above the pore will be filled.

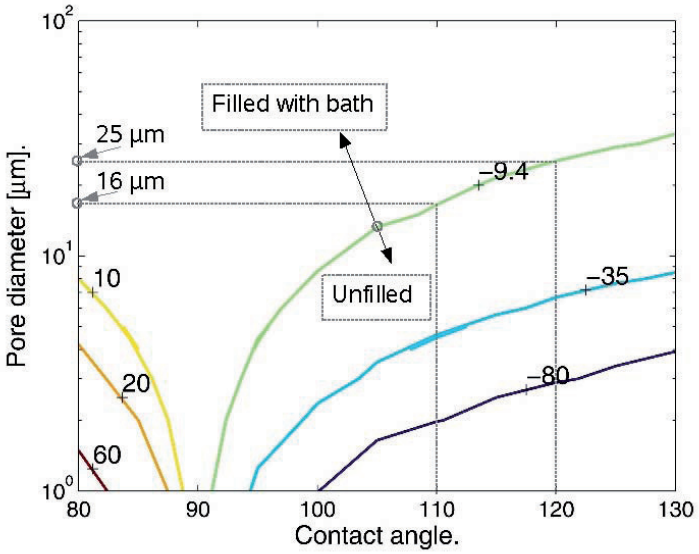

Figure 9.2: Contour of capillary pressure. Unit: kPa. γ=114 mN/m. In the region below the contour of -9.4 kPa, the pore is unfilled while in the region above the pore will be filled with bath. When contact angle is 120°, all pores smaller than 25 μm in diameter will not be filled with bath. For contact angle of 110°, the limiting pore size is 16 μm.

The contact angle obtained by the sessile drop method for graphite or other carbon materials in contact with cryolite based bath without polarization is between 127 and 114° [1], which shows poor wetting condition of the system. Contact angle varies with the degree of graphitization and composition of the bath (fluorides

addition and Al_2O_3 content). Referring to Figure 9.2, when contact angle is 120°, all pores smaller than 25 μm in diameter will not be filled with bath. For contact angle of 110° the limiting pore size reduces to 16 μm.

Due to the nature of cathode production the porosity in the cathode blocks can not be completely eliminated. Pores in cathode materials can range in size from nanometers to hundreds of microns, with bigger gaps being merely structural defects [126]. Bi-model pore size distribution is often observed in cathode blocks [127]. The majority pores appear around 5 μm and 20-50 μm. Pore size distribution for cathode blocks can vary from different producers. Figure 9.3 shows the pore size distribution of 5 industrial blocks A to F, in which Cathode E and F is impregnated [125].

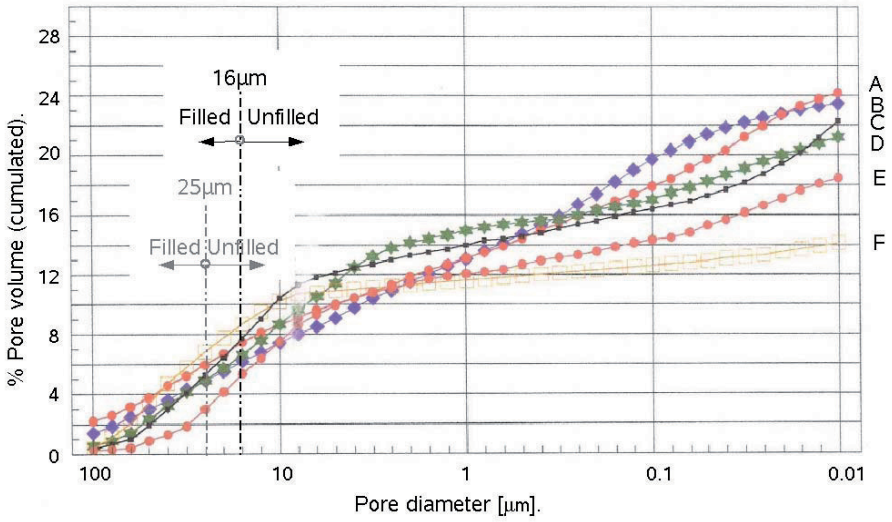

Figure 9.3: pore size distribution of 5 industrial blocks A to F [125]. When contact angle is 120°, all pores smaller than 25 μm in diameter will not be filled with bath. For contact angle of 110°, the limiting pore size is 16 μm.

Combined with the data for contact angle and pore diameter, at the initial state (without polarization), only macrocracks and large pores will be filled with bath and the rest can not be filled. Using the contact angle as 120° and 110°, the amount of pores which will not be filled with bath at a given contact angle is shown in Table 9.1. As can be seen from the table, large amount of pores in the carbon cathode is not infiltrated by bath at the initial stage without polarization. When the wetting angle is 120°, for example, 75% of the pores in Cathode A will

not be filled with bath, which corresponds to 18 vol% of the material. For Cathode F the number is 50% and 7 vol% respectively.

Table 9.1: Amount of pores which are unfilled at the initial stage, without polarization. Contact angle is 120° and 110° respectively. Unfilled pore diameter is less than 25 μm and 16.5 μm correspondingly. [1]: Impregnated.

	120°		**110°**	
	[% Prores]	[vol%]	[% Prores]	[vol%]
Cathode A	75	18	71	11
Cathode F[1]	50	7	36	5

The bath penetration is more dependent on the pore structure (pore size and volume distribution) than on the total porosity. As mentioned above, it also depends strongly on the wettability of the carbon materials.

In addition, the bath in the cathode block is often found to be basic, and the increase of NaF content will increase the surface tension of bath significantly [1]. If the molar ratio of NaF is 0.5 in the Na_3AlF_6-NaF system (CR=4), the surface tension at 1000 °C can reach 155 mN/m. According to Equation (9.1), the increasing surface tension will increase the capillary pressure, meaning that even larger amount of pores will not be filled by bath at the initial stage.

Due to the electrolysis process sodium gradually transports into the carbon materials forming the intercalation compounds resulting in the reduction of the contact angle. When the contact angle is small enough the hydrostatic pressure on top of the carbon cathode overweights the capillary resistance, and the bath starts to infiltrate into these pores. When good wetting condition is fulfilled, the bath will infiltrate into all pores with a considerable fast speed, which will be demonstrated later. Hence, the bath penetration is proposed to be controlled by how fast the wetting property changes from poor wetting to good wetting.

It was found that the contact angle reduced significantly down to around 20° or even lower [1]. Supposing the contact angle will reduce to around 20° or close to 0° (depending on different cathode quality) at sodium saturation, and assuming these two factors to have a linear relationship as shown in Figure 9.4, the contact angle will reduce to 90° when sodium concentration reaches to the range 0.49 to 0.6 wt%.

From the sodium diffusion model presented in Chapter 8, sodium concentration at the bottom of the carbon cathode will reach 0.49 or 0.6 wt% after around 120 or 150 days. Considering fast penetrating speed at good wetting condition, which

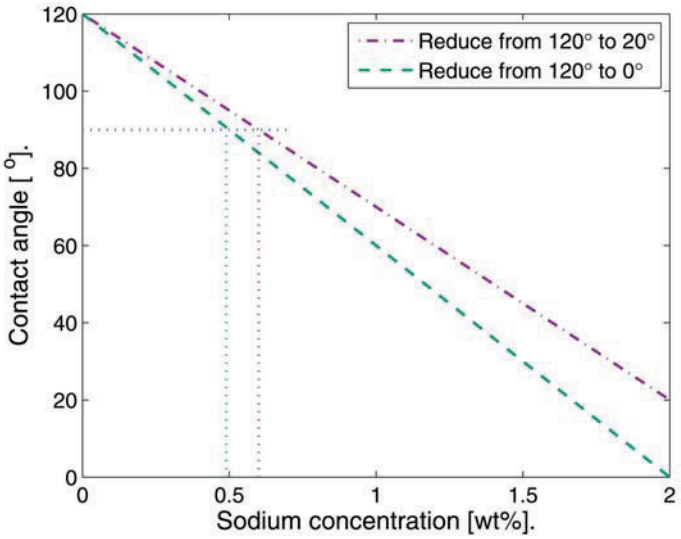

Figure 9.4: Contact angle as a function of sodium concentration (assuming linear relationship).

will be shown later, 120 to 150 days would correspond to the time it will take to fill all the pores in the cathode block all the way down to the bottom.

9.4 Micro-flow in Capillary Channel - Two Phase Flow

Bath flow in pores is a two-phase flow, and the flow speed can be solved by Navier-Stokes equation (3.17) and the phase field mode by using COMSOL 3.5a [93] when the density, viscosity of the two phases and the contact angle are known. The simulated transient velocity field and the bath/air interface is shown in Figure 9.5.

By tracking the movement of the interface/wall contact point over time, the linear velocity of the bath infiltration can be obtained. The increase in velocity is fast at the beginning and a constant speed can be achieved within 1 ms. For pore diameter of 300 μm and 150 μm, and wetting angle between 80° and 60°, the calculated moving speed is shown in Figure 9.6 (the hydrostatic pressure above carbon surface is not taken into consideration). When contact angle is 80°, the speed is in the order of 0.29 m/s for the 300 μm. The speed increases with reduction in the contact angle and increases with the decrease in pore diameter.

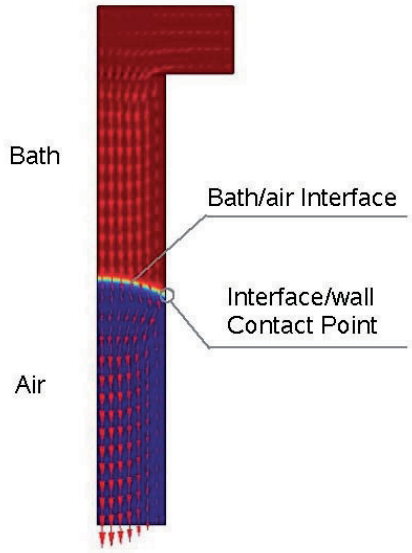

Figure 9.5: Velocity field and bath/air interface at 1 ms. Density of the bath is 2070 kg/m^3, and viscosity is 2×10^{-3} Pa·s [1]. Simulation by using COMSOL 3.5a [93].

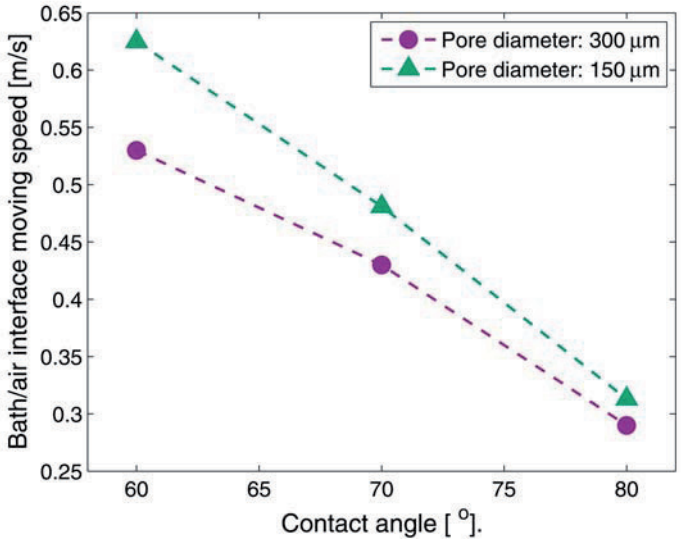

Figure 9.6: Bath/air interface moving speed as a function of contact angle. Pore diameter is 300 μm and 150 μm respectively. The speed is calculated by using COMSOL 3.5a [93].

The pores in the carbon cathode are not cylindrical as used here, therefore, tortuosity needs to be considered to estimating the length of the pores. The tortuosity of the carbon cathode material is not available. However, many efforts have been spent to derive the empirical relationship between tortuosity and porosity, which has been summarized in a handbook of porous media [128]. Based on Archie's law, a correlation has been obtained for natural consolidated media and is given by Equation (9.4)

$$\frac{1}{\tau} = 1.61\epsilon^{1.15} \tag{9.4}$$

where τ is the tortuosity and ϵ is the porosity.

For natural consolidated media, especially when the porosity is low, some of the pores may be blocked and hence not accessible to fluid flow and mass transfer. Depending on the degree of compaction, the tortuosity can be significantly different. The lower limit of the tortuosity for natural consolidated media is given by Equation (9.5)

$$\frac{1}{\tau} = \epsilon^{4/3} \tag{9.5}$$

For a porosity of 23 vol% for carbon materials, based on Equation (9.4) and (9.5), tortuosity is between 3 and 7. Taking 7 as an example, for a 0.5 m thick carbon cathode, the average length of the pores is around 3.5 m. In this case, when the contact angle is 80°, the bath will penetrate through the pore in 12 seconds. Hence, when the wetting condition is good, the bath will penetrate the carbon cathode fast through pore channels.

9.5 Discussion

The calculation at the macro-scale according to the Darcy's law demonstrates that the bath flow rate in the porous carbon materials is in the order of 10^{-6} m/s. The calculation at the micro-scale shows that when good wetting condition is fulfilled the bath penetration rate is considerably fast in the order of 0.29 m/s (300 μm in diameter at contact angle 80°). In smaller pores or at lower wetting angles, the bath will penetrate even faster. At the non-wetting condition, however, the bath can not penetrate into most of the pore channels at all due to the high capillary resistance. Therefore, the bath penetration speed is proposed to be controlled by how fast the wetting property changes from poor wetting to good wetting. A schematic drawing, illustrating the bath infiltration process, is shown in Figure 9.7.

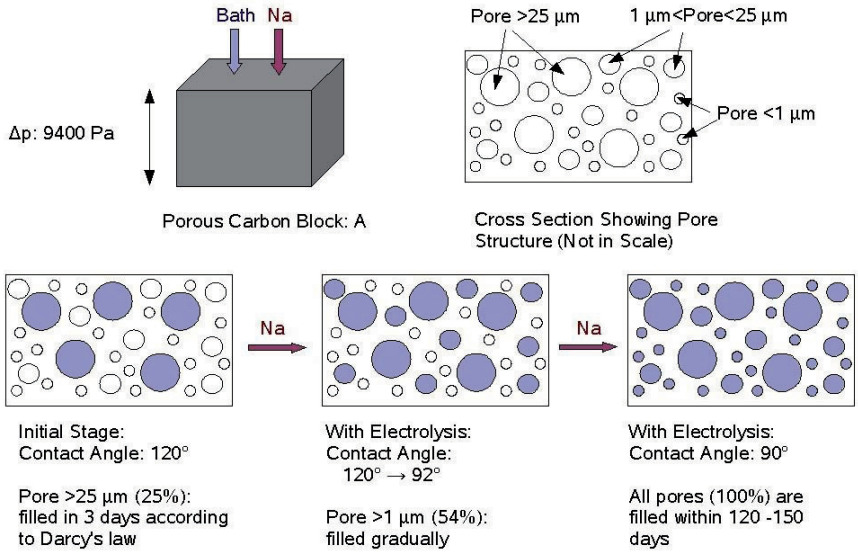

Figure 9.7: A schematic drawing illustrating the bath infiltration process (not in scale).

At the initial stage, the bath will infiltrate into large pores and cracks. The infiltration rate follows Darcy's law meaning that 12% to 50% pores will be filled with the bath after about three days. When the electrolysis takes place, the contact angle reduces gradually by the sodium infiltration. The small pores start to be filled with bath when the hydrostatic pressure is dominant. Among these small pores, relatively bigger pores would be filled by the bath earlier and followed by the smaller pores. Finally, when the contact angle reduces to 90° or even less, all the pores will be filled by the bath rapidly by the capillary drag. According to the combination of the simulations of the sodium diffusion in the cathode lining and the bath flow in the carbon cathode, it takes around 120 to 150 days until all the pores will be filled with bath.

According to the experiments done by Brilloit **et** *al.* [63], bath penetrated around 18 mm in 1.5 hours at 1010 °C, CR=2.25, CD=0.75 A/cm^2. According to Feng **et** *al.* [129], bath penetrated from 0.4 to 15 mm for different carbon materials in 1.5 hours at 1000 °C, and at same CR and current density. The bath infiltration rate depends on the type and quality of the carbon materials and ranges from 7.4×10^{-8} to 2.8×10^{-6} m/s meaning that it takes 2 to 78 days for bath to penetrate through a 0.5 m thick carbon cathode. In all cases, the bath penetration rate was slower than the sodium. Since polarizing microscope was used to determine the bath front, the

magnification might not be high enough to investigate the bath in pores of sub-micron scale. The reported rate is likely relevant to the bath flow in the pores with several micrometers in diameter or larger. From this point of view the calculations performed in this work show relatively good agreement with the measured data.

Chapter 10

Conclusion

The characterization of the virgin Si_3N_4-bonded SiC sidewall blocks has shown that the phase composition in the commercial blocks was homogeneous except the α/β Si_3N_4 phase ratio. α-Si_3N_4 was found more pronounced in the area close to the surface of the virgin block than in the center and the α/β ratio was therefore higher at the surface. Compared to the large SiC grains (in mm scale), Si_3N_4 grains (in micro or sub-micro scale) were much smaller and had a significantly larger surface area, which kinetically made Si_3N_4 the weak part of the Si_3N_4-bonded SiC materials with respect to chemical attack. Needle like α-Si_3N_4 grains had even larger surface area compared to the β-Si_3N_4 rods.

The degradation mechanisms in the gas zone (top part) and the electrolyte zone (bottom part) of the sidewall blocks were different due to the different chemical environments in the cell. The main degradation agents in the electrolyte zone were sodium diffusing from the carbon cathode and the oxidizing gases coming from the top of the sidewall blocks. The main degradation phase was Na_2SiO_3 or a mixture of Na_2SiO_3 and $Na_2Si_2O_5$ in the electrolyte zone. The presence of only Na_2SiO_3 pointed to a higher sodium potential. Sodium silicates with a layer structure was found in the electrolyte zone of the spent block. The sodium silicates filled up the pores and dramatically decreased the apparent porosity from 14-15 vol% to as low as 1 vol%. The degradation in the gas zone was more complicated. In addition to the oxidizing gas, HF gas, resulting from the volatilized bath components and the moisture inside the cell, was proposed to be involved in the degradation. The main detected degradation phase was Si_2ON_2 or cristobalite, propably reflecting different oxygen potential. The presence of Si_2ON_2 pointed to stronger reducing conditions. The oxidation was likely preferred to

α-Si_3N_4. Thinner and larger amount of needles were found in the gas zone of the spent block. The apparent porosity and density of the bulk material were not significantly changed compared to the virgin material. At the surface of the block towards the pot, material loss was observed and the remaining surface appeared porous, so the apparent porosity was proposed to be more pronouced than in the virgin material. The HF gas was proposed to "eat away" the formed oxides and further cause the detachment of the large SiC grains, and could also possibly explain the presence of the thinner needles found in the gas zone.

The area close to the surface of the virgin Si_3N_4-bonded SiC blocks with lower porosity and higher density was found to have around 10 W/(mK) lower thermal conductivity than their bulk counterpart. The thermal conductivity of the spent block was decreased significantly due to the deterioration of the materials. At room temperature, the thermal conductivity of the bottom part of the spent block (electrolyte zone) was reduced by 33% from 36 to 24 W/(mK), while at 500 °C the reduction was 52% from 23 to 11 W/(mK), despite the significant reduction in the porosity. The thermal conductivity of the top part of the spent block (gas zone) was decreased dramatically as well and below 15 W/(mK) at room temperature and 10 W/(mK) at 500 °C. The reduction relative to the virgin material was 64% and 72% respectively. It was proposed that the microstructure evolution had a strong influence on the thermal conductivity. The grain boundary resistance and pore complexity were shown to explain well the variation in the thermal conductivity of the virgin materials and the materials in the gas zone of the sidewall block. The thermal conductivity decreased with increasing of grain boudary resistance, i.e. the reduction in the grain size. In the electrolyte zone of the spent sidewall block, the sodium silicate layers, which formed at the surface of the grains during the degradation, act as a thermal insulating layer blocking the heat transfer. Computer simulations demonstrated that the drop in the thermal conductivity of the sidewall block will result in a hotter surface of the block towards the side ledge and a thinner side ledge.

Sodium diffusion and reaction behavior in the cathode lining were investigated by computer simulations by taking into consideration the different degradation mechanisms in each layer of the cathode lining and the sodium mass balance in the cell. The simulations demonstrated that in the carbon cathode the dominant diffusion process of sodium was solid state diffusion, while in the sidewall block the sodium diffusion was limited by the chemical reaction resulting in formation of sodium silicates. The simulations demonstrated that changes in the properties of the cathode materials as well as the ramming paste (big joint) material will influence on the degradation of the sidewall block. Moreover, the simula-

tion showed that sodium diffusion in the refractory lining is well described by the self-diffusion of sodium in albite like molten oxides, corresponding to a diffusion constant around 10^{-9} m^2/s at 900 °C.

The bath components are the other main degradation agents in addition to sodium. Efforts were made to estimate the penetration rate of the bath into the carbon cathode. The simulations demonstrate that the infiltration rate was determined by the changes in the wetting property of the carbon material towards the bath which was associated with the sodium concentration in the cathode lining. The bath infiltration is strongly related to the pore size distribution in the carbon cathode block rather than the apparent porosity. The big pores in the carbon cathode were shown to be filled with bath after about three days by Darcy's Law. With the reduction of contact angle during electrolysis the smaller pores will be filled. Combining the simulations of the sodium diffusion in the cathode lining, it was shown that it would take around 120 to 150 days until all the pores in the carbon block were filed with bath.

Chapter 11

Outlook

In Si_3N_4-bonded SiC materials, the Si_3N_4 binder is kinetically the weak part of the material due to its significantlt higher surface area. α-Si_3N_4 needles have even higher surface area, and easier attacked by the degradation agents. The microstructure of the materials therefore plays an important role in the chemical degradation. Moreover, microstructure related properties like grain size, grain boundary resistance, pore shape and orientation are the major factors influencing the thermal conductivity of the material. Therefore, finding the mechanisms to control the amount of α-Si_3N_4 in the binder phase of the virgin block and/or to manipulate the microstructure of the binder phase should be addressed in future. The α to β Si_3N_4 phase ratio is known to be influenced by the fabrication conditions such as heating process, dwelling temperature, nitridation time, etc. and raw material properties such as oxygen content in nitrogen gas, impurities in SiC and Si grains (especially oxides and cations). Systematical study of the nitridation conditions could be helpful to obtain Si_3N_4-bonded SiC material with optimized microstructure and phase composition.

Regarding the oxidation in the gas zone of the sidewall block, the presence of Si_2ON_2 points to strongly reducing condition during oxidation. The oxidation at such low oxidant potential is likely to be active oxidation instead of passive oxidation [39]. An oxidation test at reducing condition instead of air or nitrogen atmosphere could be considered as a method to test commercial Si_3N_4-bonded SiC materials. In addition, HF gas is proposed to be another important degradation agent in the gas zone. HF gas could also be included in such an oxidation test.

The degradation mechanisms in the gas zone (top part) and the electrolyte zone

(bottom part) are proven to be different due to the different chemical environments in the cell. Therefore, some points might be considered in further development of future sidewall blocks:

- Shaped Si_3N_4-bonded SiC sidewall block, meaning that the thickness of the top and bottom part of the block does not necessary need to be equal
- Introduce a dense coating to the top part of the block to obtain higher resistance to active oxidation, and reduce the thickness of the top part of the block for larger anodes
- Material of top and bottom part of the sidewall block can be different in order to get the optimized resistance to the oxidation and sodium involved oxidation respectively

A stable sidewall block material is required in a high amperage cell due to the requirements of both the optimal thermal balance of the cell and the possibility to recover heat from the heat flux through the sidewall block. A diffusion barrier (like a steel plate or a chemical barrier) between the ramming paste (big joint) and the sidewall block is proposed as a possible way to inhibit/reduce the sodium infiltration into the sidewall block, which will lower the degradation. Moreover, the simulation performed in this work demonstrated that using high thermal conductivity ramming paste (big joint) helps to extract more heat from the sidewall block and in such a way to possibly incorporate heat recovery through sidewall blocks.

In fact, a heat recovery set up inside the collector bar may be also a good choice since the temperature in the middle part of the collector bar is significantly higher than the sidewall block and the collector bar does not deteriorate over time. The deformation of the collector bar due to cathode heaving needs to be considered. The set up inside the collector bar needs to be somehow flexible at the region where the deformation occurs.

In order to estimate the bath infiltration rate more accurately, the variation in the wetting property of the carbon cathode during the electrolysis process, i.e. the variation with the sodium concentration in the carbon, is important to know. Experimental work for measuring the wetting angle and the sodium concentration of the carbon materials during the electrolysis will benefit both the understanding of the bath infiltration and the sodium diffusion phenomenon.

The simulations performed in this work demonstrated that the transport of sodium in the carbon block was dominated by solid phase diffusion and the diffusion

constant of sodium in the refractory layer could be well described by sodium self-diffusion in an albite like oxide. The transportation mechanisms of sodium in both carbon block and refraction layer, however, are still not well understood. Sodium intercalation or adsorption in the carbon material and sodium diffusion constant in the refractory material should be studied in more detail.

Last but not least, several models have been built in the present work to describe phenomenons with respect to the degradation of the cathode lining. Computer simulation has been proven to be a promising tool for understanding of the aging of the lining materials. In future work, more sophisticated and accurate models should be built in order to link chemical, thermal, electrical, mechanical and/or fluid dynamic problems occurring in the cell, for both fundamental study and complex industry process simulation. Ledge dynamics and cathode wear, for example, are all multi-physical phenomenons, using computer simulation will for sure give a better understanding of the problem and will benefit the process control for the industry in a long term.

Bibliography

[1] J. Thonstad, P. Fellner and G.M. Haarberg. *Aluminium Electrolysis.* Aluminium-Verlag Marketing and Kommunikation GmbH, 3rd. edition, 2001.

[2] K. Grjotheim and K. Kvande. *Introduction to Aluminium Electrolysis*. Aluminium-Verlag GmbH, 2nd. edition, 1993.

[3] M. Sørlie and H.A. Øye. *Cathodes in Aluminium Electrolysis.* Aluminium-Verlag GmbH, Düsseldorf, 2nd. edition, 1994.

[4] http://www.aluminumsmeltingprocess.com/index.html. The Aluminum Production Process. Quotation date: Mar. 18, 2010.

[5] Hydro Aluminium. Introduction to Hydro Aluminium Årdal, NTNU, 2006.

[6] M. Sørlie and H.A. Øye. *Cathodes in Aluminium Electrolysis.* Aluminium-Verlag Marketing & Kommunikation GmbH, Düsseldorf, 3rd. edition, 2010.

[7] E. Skybakmoen, L.I. Stoen, J.H. Kvello and O. Darell. Quality evaluation of nitride bonded silicon carbide sidelining materials. *Light Metals (TMS)*, pages 773–778, 2005.

[8] A.V. Froloy et al. Wetting and cryolite bath penetration in graphitized cathode materials. *Light Metals (TMS)*, pages 645–649, 2006.

[9] O.J. Siljan, Ch. Schøning and T. Grande. State-of-the-art alumino-silicate refractories for al electrolysis cell. *JOM*, 54(2):46–54, 2002.

[10] Ch. Schøning and T. Grande. The stability of refractory oxides in sodium-rich environments. *JOM*, pages 58–61, 2006.

[11] F.B. Andersen, G. Dörsam, M. Stam and M. Spreij. Wear of silicon nitride bonded SiC bricks in aluminium electrolysis cells. *Light Metals (TMS)*, pages 413–418, 2004.

[12] E. Skybakmoen. Evaluation of chemical/resistance/oxidation of Si_3N_4-SiC sidelining materials used in Al electrolysis cells. *Unified International Technical Conference on Refractories*, pages 1330–1339, 2001.

[13] K.R. Kvam and H.A. Øye. Homogeneity and degradation of SiC sidelinings. *Ninth International Symposium on Light Metals Production*, pages 313–320, 1997.

[14] R. Etzion, J.B. Metson and N. Depree. Wear mechanism study of silicon nitride bonded silicon carbide refractory materials. *Light Metals (TMS)*, pages 955–959, 2008.

[15] Günter Berndt. New sidewall lining in modern high current hall-herault electrolysis cell. Symposium, Refractories Technology for the Aluminium and the Petrochemical Industry, Düsseldorf, Germany, 2003.

[16] O.J. Siljan. Patent. electrolysis cell and structural elements to be used therein. International publication number: WO 2004/083489 A1. International publication date: September 30, 2004.

[17] A.P. Ratvik, A. Støre, A. Solheim and T. Foosnæs. The effect of current density on cathode expansion during start-up. *Light Metals (TMS)*, pages 973–978, 2008.

[18] A. Zolochevsky, J.G. Hop, T. Foosnæs and H.A. Øye. Surface exchange of sodium, anisotropy of diffusion and diffusional creep in carbon cathode materials. *Light Metals (TMS)*, pages 745–750, 2005.

[19] Zh. Wang. Thermo-mechanical models for degradation of sidelining in aluminium. Diploma work, Master of Science in Light Metals Production, NTNU, autumn 2007.

[20] K. Tschöpe. *Degradation of Cathode Lining in Hall-Héroult Cells - Autopsies and FEM Simulation*. PhD thesis, Norwegian University of Science and Technology (NTNU), Norway, 2010.

[21] W.J. Parker, R.J. Jenkins, C.P. Butler and G.L. Abbott. Flash method of determining thermal diffusivity, heat capacity, and thermal conductivity. *Journal of Applied Physics*, 32(9):1679–1684, 1961.

[22] J. Schoennahl, E. Jorge and P. Temme. Optimization of Si_3N_4 bonded sic refractories for aluminium reduction cells. *Light Metals (TMS)*, pages 251–255, 2001.

[23] R.P. Pawlek. SiC in electrolysis pots: An update. *Light Metals (TMS)*, 2006.

[24] R.P. Pawlek. SiC in aluminium electrolysis cells. *Light Metals (TMS)*, pages 527–533, 1995.

[25] E. Skybakmoen, J.H. Kvello and O. Darell. Chemical resistance of sidelining materials based on SiC and carbon in cryolitci melts - a laboratory study. *Light Metals (TMS)*, pages 215–222, 1999.

[26] Z. Huang. Excellect cryolite resistance and high thermal conductivity SiC sidewall material for high-amperage aluminium reduction cells. *Light Metals (TMS)*, pages 889–894, 2010.

[27] http://www.refractories.saint-gobain.com/aluminium-reduction.aspx. Saint-Gobain Ceramics. Quotation date: March 23, 2010.

[28] G.H. Aylward and T.J.V. Findlay. *SI Chemical Data*. John Wiley and Sons Australia, Ltd, 5th. edition, 2002.

[29] W. Bale, P. Chartrand, S.A. Degterov, G. Eriksson, K. Hack, R.B. Mahfoud, J. Melancon, A.D. Pelton and S. Petersen. FactSage thermochemical software and databases. *Calphad*, 83(9):189–228, 2002.

[30] A. Solheim. *Preparation and characterizations of AlN/Al-composite Materials as Side Lining in Alumiuium Electrolysis Cells.* PhD thesis, Norwegian University of Science and Technology (NTNU), Norway, 1999.

[31] A.J. Moulson. Review. reaction-bonded silicon nitride: Its formation and properties. *Journal of Materials Science*, 14:1017–51, 1979.

[32] H.M. Jennings. Review on reactions between silicon and nitrogen, Part 1 mechanisms. *Journal of Materials Science*, 18:951–967, 1983.

[33] Ch. Wang, X. Pan, M. Rühle and F.L. Riley. Review. Silicon nitride crystal structure and observations of lattice defects. *Journal of Materials Science*, 31:5281–5298, 1996.

[34] http://www.hardmaterials.de/html/alpha-si3n4_beta-si3n4.html. Handbook of Ceramic Hard Materials, WILEY-VCH, Quotation date: March 24, 2010.

[35] M.W. Chase, C.A. Davies, J.R. Downey and A.N. Syverud. JANAF thermochemical table. *Journal of Phys, Chem. Ref. Data*, 14, 1985.

[36] D. Park, H. Kim, K. Lim and C. Park. Microstructure of reaction-bonded silicon nitride fabricated under static nitrogen pressure. *Materials Science and Engineering A*, 405:158–162, 2005.

[37] K.R. Kvam and H.A. Øye. Homogeneity and degradation of SiC sidelining. Ninth International Symposium on Light Metals Production, NTNU, Trondheim, Norway, 1997.

[38] E. Hagen, M.A. Einarsrud and T. Grande. Chemical stability of ceramic sidelinings in hall-heroult cell. *TMS*, pages 257–264, 2001.

[39] G.X. Wang, B. Pei and A.B. Yu. Oxidation mechanism of Si_3N_4-bonded SiC ceramics by CO, CO_2 and steam. *Journal of Materials Science*, 33:1309–1317, 1998.

[40] W. Gao, A. Hendry and G. Holling. Oxidation of nitride bonded silicon carbide in wet air atmosphere. *British Ceramic Transactions*, 101(6):231–236, 2002.

[41] Georges Chollon. Oxidation behaviour of ceramic fibers from the Si-C-N-O system and related sub-system. *Journal of the European Ceramic Society*, 20:1959–1974, 2000.

[42] H. Du, R.E. Tressler and K.E. Spear. Thermodynamics of the Si-N-O system and kinetic modeling of oxidation of Si_3N_4. *Journal of Elctrochem. Society*, 136:3210–3215, 1989.

[43] V. Luthra. A mixed interface reaction/diffusion control model for oxidation of Si_3N_4. *Journal of Elctrochem. Society*, 138(10):3001–3007, 1991.

[44] K.L. Luthra. Some new perspectives on oxidation of silicon carbide and silicon nitride. *Journal of the American Ceramic Society*, 74(5):1095–1103, 1991.

[45] G.R. Pickrell, T. Sun and J.J. Brown. High temperature alkali corrosion of SiC and Si_3N_4. *Fuel Processing Technology*, 44:213–236, 1995.

[46] O.J. Siljan, T. Grande and Ch. Schøning. Refractories for aluminium electrolysis cells part III: Laboratory tests for cryolite resistance. *Aluminium*, 77(7/8):610–613, 2001.

[47] O.J. Siljan, T. Grande and Ch. Schøning. Refractories for aluminium electrolysis cells part I: Deterioration mechanisms based on phase equilibria. *Aluminium*, 77(4):294–300, 2001.

[48] O.J. Siljan, T. Grande and Ch. Schøning. Refractories for aluminium electrolysis cells part II: Physical properties of penetrating melt, reduction by metals and volatile fluorides. *Aluminium*, 77(5):385–390, 2001.

[49] O.J. Siljan, T. Grande and Ch. Schøning. Refractories for aluminium electrolysis cells part IV: Comparison of laboratory investigations and autopsies of pot linings. *Aluminium*, 77(7/8):610–613, 2001.

[50] Ch. Schøning. Review of degradation mechanisms relevant for transient modeling of cathode lining degradation. Internal report, 2007.

[51] K. Tschöpe and T. Grande. Chemical degradation map for sodium attack in refractory linings. *Light Metals (TMS)*, pages 871–876, 2010.

[52] A. Solheim, Ch. Schøning and E. Skybakmoen. Reactions in the bottom lining of aluminium reduction cells. *Light Metals (TMS)*, pages 877–882, 2010.

[53] Ch. Tan. Models for degradation of refractory lining in aluminium electrolysis cells. Project Work Report, Master of Science in Light Metals Production, NTNU, autumn 2007.

[54] K. Tschöpe, Ch. Schøning and T. Grande. Autopsies of spent pot linings - a revised view. *Light Metals (TMS)*, pages 1085–1090, 2009.

[55] Ch. Tan. Models for degradation of refractory lining in aluminium electrolysis cells. Diploma Work, Master of Science in Light Metals Production, NTNU, spring 2008.

[56] A.T. Tabereaux. The role of sodium in aluminium electrolysis: A possible indicator of cell performance. *Light Metals (TMS)*, pages 319–326, 1996.

[57] Y. Sun, Q. Wang, K.Å. Rye and H.A. Øye. Modelling of thermal and sodium expansion in prebaked aluminium reduction cells. *Light Metals (TMS)*, pages 603–610, 2003.

[58] P.Y. Brisson, G. Soucy, M. Fafard and M. Dionne. The effect of sodium on the carbon lining of the aluminum electrolysis cell - A review. *Canadia Metallurgical Quarterly*, 44(2):265–280, 2005.

[59] J.G. Hop. *Sodium Expansion and Creep of Cathode Carbon.* PhD thesis, Norwegian University of Science and Technology (NTNU), Norway, 2003.

[60] L.R. Lossius and H.A. Øye. Melt penetration and chemical reactions in 16 industrial aluminum carbon cathodes. *Metallurgical and Materials Transactions B*, 31B:1213–1224, 2000.

[61] M.B. Dell. Reaction between carbon lining and hall bath. *Extractive Metallurgy of Aluminium*, 2:403–416, 1963.

[62] E.W. Dewing. The reaction of sodium with nongraphitic carbon: Ractions occurring in the linings of aluminum reduction cells. *Transactions of the Metallurgical Society of AIME*, 227:1328–1333, 1963.

[63] P. Brilloit, L.P. Lossius and H.A. Øye. Penetration and chemical reactions in carbon cathodes during aluminum electrolysis: Part I. Laboratory expeiments. *Metallurgical Transactions B*, 24B:75–89, 1993.

[64] C. Krohn, M. Sørlie and H.A. Øye. Penetration of sodium and bath constituents into cathode carbon materials used in industrial cells. *Light Metals (TMS)*, pages 311–324, 1982.

[65] A. Zolochevsky, J.G. Hop, T. Foosnæs and H.A. Øye. Rapoport-Samoilenko test for cathode carbon materials I. Experimental reslts and constitutive modelling. *Carbon*, 41:497–505, 2003.

[66] E.W. Dewing. Longitudinal stresses in carbon lining blocks. *Light Metals (TMS)*, 3:879–887, 1974.

[67] T. Naas. *Interactions of Alkali Metals and Electrolyte with Cathode Carbons.* PhD thesis, NTNU, Norway, 1997.

[68] M.J. Toplis, D.B. Dingwell, K. Gess and T. Lenci. Viscosity, fragility, and configurational entropy of melts along the join SiO_2-$NaAlSiO_4$. *American Mineralogist*, 82:979–990, 1997.

[69] O.V. Mazurin. *Handbook of Glass Data - Physical Science Data 15., Part C.* Elsevier Science Publishing Company, New York, 1987.

[70] H. Scholze. *Glass - Nature, Structure, and Properties*. Springer-Verlag New York, Inc., 1990.

[71] http://commons.wikimedia.org/wiki/file:kalk-natron-glas_2d.png. Wikimedia Commons. Quotation date: March 26, 2010.

[72] E.B. Watson and D.R. Baker. Chemical diffusion in magmas: An overview of experimental results and geochemical applications. *Advances in Physical Geochemistry*, 9:120–151, 1991.

[73] D.B. Dingwell. Effects of structural relaxation on cationic tracer diffusion in silicate melts. *Chemical Geology*, 82:209–216, 1990.

[74] I. Avramov. Diffusion coefficient of foreign particles in glassforming melts. *Journal of Non-Crystalline Solids*, 354:1537–1540, 2008.

[75] E.M.T. Njiokep, A.W. Imre and H. Mehrer. Tracer diffusion of ^{22}Na and ^{45}Ca, ionic conduction and viscosity of two standard soda-lime glasses and their undercooled melts. *Journal of Non-Crystalline Solids*, 354:355–359, 2008.

[76] E.M.T. Njiokep and H. Mehrer. Diffusion of ^{22}Na and ^{45}Ca and ionic conduction in two standard soda-lime glasses. *Solid State Ionics*, 177:2839–2844, 2006.

[77] R. Hempelmann, C.J. Carlile, D. Beyer and Ch. Kaps. Sodium self-diffusion coefficient in sodium silicate glass by quasielastic neutron scattering. *Zeitschrift Für Physik B*, 95:49–53, 1995.

[78] A. Jambon and J.P. Carron. Diffusion of Na, K, Rb and Cs in glasses of albite and orthoclase composition. *Geochimica et Cosmochimica Acta*, 40:897–903, 1976.

[79] H.M. Garfinkel and H.E. Rauscher. Diffusion of radiotracer sodium by the residual surface counting technique in Soda-Alumina-Silica glasses. *Journal of Applied Physics*, 37(5):2169–2174, 1966.

[80] V.A. Zhabrev and S.I. Sviridov. Ion diffusion in oxide glasses and melts: I. Bibliography. *Glass Physics and Chemistry*, 29(2):140–159, 2003.

[81] D.B. Dingwell and Ch.M. Scarfe. Chemical diffusion of fluorine in melts in the system Na_2O-Al_2O_3-SiO_2. *Earth and Planetary Science Letters*, 73:377–384, 1985.

[82] R.C. Progelhof, J.L. Throne and R.R. Ruetsch. Methods for predicting the thermal conductivity of composite system: A review. *Polymer Engineering and Science*, 16(9):615–625, 1976.

[83] J.C. Maxwell. *A Treatise on Electricity and Magnetism.* Dover Publications, Inc, New York, 1954.

[84] B. Troschke and H. Burkhardt. Thermal conductivity models for two-phase system. *Physics and Chemistry of the Earth*, 23(3):351–355, 1998.

[85] R. Landauer. The electrical resistance of binary metallic mixtures. *Journal of Applied Physics*, 23(7):779–784, 1952.

[86] B. Schulz. Thermal conductivity of porous and highly porous materials. *High Temp. High Press.*, 13:649–660, 1981.

[87] F. Cernuschi, S. Ahmaniemi, P. Vuoristo and T. Mäntylä. Modelling of thermal conductivity of porous materials: application to thick thermal barrier coatings. *Journal of the European Ceramic Society*, 24:2657–2667, 2004.

[88] D.S. Smith, S. Fayette, S. Grandjean and Ch. Martin. Thermal resistance of grain boundaries in alumina ceramics and refractories. *Journal of the American Ceramic Society*, 86(1):105–111, 2003.

[89] D.S. Smith, S. Grandjean J. Absi and S. Fayette. Grain-boundary thermal resistance in polycrystalline oxides: alumina, tin oxide, and magnesia. *High Temperatures-High Pressures*, 35/36:93–99, 2003/2004.

[90] B. Nait-Ali, K. Haberko, H. Vesteghem and D.S. Smith. Thermal conductivity of highly porous zirconia. *Journal of the European Ceramic Society*, 26:3567–3574, 2006.

[91] N. Ottosen and H. Petersson. *Introduction to the Finite Element Method*. Prentice Hall Europe, 1st. edition, 1992.

[92] J.N. Reddy. *An Introduction to the Finite Element Method*. McGraw-Hill International Editions, 2nd. edition, 1993.

[93] COMSOL. *COMSOL Multiphysics® User's Guide*. COMSOL AB, 3.5a edition, 2008.

[94] Zh. Wang, E. Skybakmoen and T. Grande. Spent Si_3N_4 bonded SiC sidelining materials in alminium electrolysis cells. *Light Metals (TMS)*, pages 353–358, 2009.

[95] Zh. Wang, E. Skybakmoen and T. Grande. Chemical degradation of Si_3N_4-bonded SiC sidelining materials in alminium electrolysis cells. *Journal of the American Ceramic Society*, 92(6):1296–1302, 2009.

[96] H.M. Rietveld. A profile refinement method for nuclear and magnetic structures. *Journal of Applied Crystallography*, 2:65–71, 1969.

[97] L.B. McCusker, R.B.V. Dreele, D.E. Cox and P. Scardi. Rietveld refinement guidelines. *Journal of Crystallography)*, 32:36–50, 1999.

[98] H. Toraya. Crystal structure refinement of α-Si_3N_4 using synchrotron radiation powder diffraction data: Unbiased refinement strategy. *Journal of Applied Crystallography*, 33:95–102, 2000.

[99] R. Grün. The crystal structure of β-Si_3N_4; Structural and stability considerations between α- and β-Si_3N_4. *Acta Cryst.*, B35:800–804, 1979.

[100] P.T.B. Shaffer. A review of the structure of silicon carbide. *Acta Cryst.*, B25:477–488, 1968.

[101] J. Sjöberg, G. Helgesson and I. Idrestedt. Refinement of the structure of Si_2N_2O. *Acta Cryst.*, C47:2438–2441, 1991.

[102] D.R. Peacor. High-temperature single-crystal study of the cristobalite inversion. *Zeitschrift für Kristallographie*, 138:274–298, 1973.

[103] W.S. McDonald and D.W.J. Cruickshank. A reinvestigation of the structure of sodium metasilicate, Na_2SiO_3. *Acta Cryst.*, 22:37–43, 1967.

[104] A.K. Pant and D.W.J. Cruickshank. The crystal structure of α-$Na_2Si_2O_5$. *Acta Cryst.*, B24:13–19, 1968.

[105] A.K. Pant. A reconsideration of the crystal structure of β-$Na_2Si_2O_5$. *Acta Cryst.*, B24:1077–1083, 1968.

[106] G.S. Hughes, C. McGreavy and J.H. Merkin. A theoretical model of the manufacture of reaction-bonded silicon nitride with particular emphasis on the effect of ambient reaction temperature and compact size. *Journal of Materials Science*, 15:2345–2353, 1980.

[107] Sh. Wang. Fabrication of Si_3N_4-bonded SiC sidewall block. LIRR. Personal communication. Quotation date: February 2010.

[108] R.C. Weast and S.M. Selby. *Handbook of Chemistry and Physics.* The Chemical Rubber Co., Ohio, USA, 78th. edition, 1997.

[109] M.B. Fegley. The thermodynamic properties of silicon oxynitride. *Communications of the American Ceramic Society*, C:124–126, 1981.

[110] P. Rocabois, Ch. Chatillon and C. Bernard. Thermodynamics of the Si-O-N system: II, Stability of Si_2N_2O by high-temperature mass spectrometric vaporization. *Journal of the American Ceramic Society*, pages 1361–1365, 1996.

[111] M. Hillert, S. Jonsson and B. Sundman. Thermodynamic calculation of the Si-N-O system. *Z. Metallkd.*, 83(9):648–654, 1992.

[112] S. Stølen and T. Grande. *Chemical Thermodynamics of Materials - Macroscopic and Microscopic Aspects*. John Wiley and Sons, Ltd., England, 2004.

[113] E. Skybakmoen. Autopsies of the sidewall block in the aluminium electrolysis cell. SINTEF. Personal communication. Quotation date: November 2009.

[114] http://www.ioffe.ru/sva/nsm/semicond/sic/thermal.html. Ioffe Physico-Technical Institute. Quotation date: Mar. 18, 2010.

[115] D.T.Morelli and J.P. Heremans. Thermal conductivity of Germanium. Silicon, and Carbide Nitride. *Applied Physics Letters*, 81(27):5126–5128, 2002.

[116] H. Scholze. *Glass-Nature, Structure, and Properties*. Springer-Verlag New York, Inc, 1991. Page: 363.

[117] D.S. Severo and V. Gusberti. A modelling approach to estimate bath and metal heat transfer coefficients. *Light Metals (TMS)*, pages 557–562, 2009.

[118] A. Solheim. Thermal conductivity of the mortar. SINTEF. Personal communication. Quotation date: April 2010.

[119] J.L. Rutlin. Soda ash addition. Hydro Aluminium AS. Personal communication. Quotation date: February 2009.

[120] S.O. Ryman. AlF_3 and soda ash addition. Hydro Aluminium AS. Personal communication. Quotation date: February 2009.

[121] J. Sangster. C-Na (Carbon-Sodium) system. *Journal of Phase Equilibria and Diffusion*, 28(6):571–579, 2007.

[122] J.C. Slattery. *Advanced transport phenomena.* Cambridge University Press, Printed in USA, 1999.

[123] J.L. Rutlin. *Chemical reactions and mineral formation during sodium aluminium fluoride attack on aluminosilicate and anorthite based refractories.* PhD thesis, Norwegian University of Science and Technology (NTNU), Norway, 1998.

[124] A. Solheim and Ch. Schøning. Deterioration of the bottom lining in aluminium reduction cells - Part I: Chemical equilibria at 1100K. *Proceeding of Aluminium of Siberia*, pages 69–75, 2008. Knrasnoyarsk, Russia.

[125] J. Stanislaw. Pore size distribution in carbon cathode materials. Hydro Aluminium AS. Personal communication. Quotation date: June 2009.

[126] F. Hiltmann, P. Patel and M. Hyland. Influence of internal cathodes structure on behavior during electrolysis. Part I: Properties of graphitec and graphitized material. *Light Metals (TMS)*, pages 751–756, 2005.

[127] S.A. Khramenko, P.V. Polyakov, A.V. Rozin and A.P. Skibin. Effect of porosity structure on penetration and performance of lining materials. *Light Metals (TMS)*, pages 795–799, 2005.

[128] K. Vafai. *Handbook of Porous Media.* Taylor & Francis, 2005.

[129] N. Feng, H. Kvande and H.A. Øye. Penetration of sodium and molten bath into high pressure baked cathode blocks. *Aluminium*, 73:265–270, 1997.

Appendix A

LECO

Table A.1: Total oxygen, nitrogen, and carbon content from LECO, units in wt%. [1]: close to the surface to the frozen bath, [2]: close to the surface to the steel shell.

Sample Label		Oxygen	Nitrogen	Carbon	Age
Block A2	Surface	0.9	9.8	NA	Virgin
	Center	0.6	9.2	NA	
C1[1]	Electrolyte Zone	4.4	7.0	20.3	270 days
C2		4.8	6.1	19.8	
C3		5.2	6.0	20.7	
C4[2]		1.7	9.1	21.4	
C6		5.8	5.5	20.8	
C7		1.4	8.3	21.6	
D1	Gas Zone	1.1	8.6	NA	
D2		1.0	8.7	19.7	
D3		0.9	8.7	19.5	
D4		0.9	7.6	21.0	
E1[1]	Electrolyte Zone	4.7	6.3	NA	604 days
E2		5.2	5.7	NA	
E3		5.5	5.4	NA	
E4		2.5	7.5	NA	
E5[2]		1.2	9.1	NA	
F1[1]	Gas Zone	2.2	7.4	NA	
F2		0.9	8.5	NA	
F3		1.0	8.8	NA	
F4		0.8	8.5	NA	
F5[2]		0.8	9.0	NA	
G1[1]	Electrolyte Zone	4.4	4.3	NA	1569 days/Refrax 20
G2		5.6	4.2	NA	
G3		6.3	3.1	NA	
G4		6.0	3.3	NA	
G5[2]		5.7	4.7	NA	
H1[1]	Gas Zone	3.0	4.4	NA	
H2		3.5	5.7	NA	
H3		3.1	5.6	NA	
H4		2.6	5.3	NA	
H5[2]		2.4	6.6	NA	

Appendix B

Thermal Conductivity Data

B.1 Virgin Blocks

B.1.1 Block A Center

Table B.1: Thermal conductivity data for virgin Block A.

Temperature [^{o}C]	**Thermal Diffucivity** [m^2/s]	**Thermal Conductivity** [W/(m·K)]	**Specific Heat** [J/(kg·K)]
27	13.72	28.88	0.58
102	14.25	30.60	0.82
201	11.48	28.99	0.95
301	9.76	27.11	1.05
402	8.62	25.49	1.11
501	7.72	23.84	1.15
603	7.05	22.50	1.19
702	6.39	20.90	1.23
802	5.94	19.80	1.27
901	5.67	19.18	1.27

B.1.2 Block B Surface

Table B.2: Thermal conductivity data for virgin Block B surface.

Temperature [^{o}C]	**Thermal Diffucivity** [m^2/s]	**Thermal Conductivity** [W/(m·K)]	**Specific Heat** [J/(kg·K)]
27	20.67	44.78	0.72
102	18.05	42.76	0.91
201	14.20	38.27	1.00
301	11.91	34.66	1.09
402	10.33	31.66	1.15
501	9.15	29.07	1.20
603	8.17	26.66	1.21
702	7.40	24.63	1.26
801	6.74	22.80	1.28
901	6.23	21.36	1.28

B.1.3 Block B Center

Table B.3: Thermal conductivity data for virgin Block B center.

Temperature [^{o}C]	**Thermal Diffucivity** [m^2/s]	**Thermal Conductivity** [W/(m·K)]	**Specific Heat** [J/(kg·K)]
28	25.85	53.89	0.72
102	20.54	50.18	0.60
201	16.86	45.05	0.99
301	14.01	40.46	1.08
402	12.00	36.53	1.14
501	10.51	33.17	1.19
603	9.38	30.42	1.20
702	8.52	28.22	1.24
802	7.75	26.07	1.29
901	7.15	24.38	1.28

B.1.4 Block C Surface

Table B.4: Thermal conductivity data for virgin Block C surface.

Temperature [^{o}C]	**Thermal Diffucivity** [m^2/s]	**Thermal Conductivity** [W/(m·K)]	**Specific Heat** [J/(kg·K)]
26	15.11	24.38	0.58
101	12.45	25.07	0.73
201	10.15	23.85	0.85
301	11.91	22.62	0.94
402	7.78	21.35	0.99
501	7.11	20.31	1.04
602	6.49	19.30	1.08
702	5.99	18.40	1.12
802	5.57	17.71	1.16
901	5.21	16.37	1.15
1001	4.93	16.23	1.20

B.1.5 Block C Center

Table B.5: Thermal conductivity data for virgin Block C center.

Temperature [^{o}C]	**Thermal Diffucivity** [m^2/s]	**Thermal Conductivity** [W/(m·K)]	**Specific Heat** [J/(kg·K)]
25	23.15	38.23	0.60
101	18.61	38.23	0.74
201	14.90	35.88	0.87
301	12.48	33.24	0.96
402	10.81	30.23	1.01
501	9.66	28.17	1.06
602	8.69	26.17	1.10
702	7.92	24.30	1.12
802	7.24	22.67	1.14
1001	6.24	20.60	1.21

B.1.6 Block D Surface

Table B.6: Thermal conductivity data for virgin Block D surface.

Temperature [^{o}C]	**Thermal Diffucivity** [m^2/s]	**Thermal Conductivity** [W/(m·K)]	**Specific Heat** [J/(kg·K)]
26	17.36	29.53	0.64
101	14.12	29.94	0.80
201	11.44	28.07	0.92
301	9.74	26.06	1.01
402	8.51	23.95	1.06
501	7.69	22.43	1.10
602	7.01	21.43	1.15
702	6.47	21.50	1.26
802	6.03	19.78	1.24
901	5.62	20.42	1.38
1001	5.26	17.21	1.24

B.1.7 Block D Center

Table B.7: Thermal conductivity data for virgin Block D center.

Temperature [^{o}C]	**Thermal Diffucivity** [m^2/s]	**Thermal Conductivity** [W/(m·K)]	**Specific Heat** [J/(kg·K)]
26	22.26	40.17	0.62
101	18.85	37.42	0.74
201	14.84	33.72	0.85
301	12.42	31.21	0.94
402	10.70	28.37	1.00
501	9.45	26.19	1.04
602	8.44	25.05	1.12
702	7.63	23.21	1.15
802	7.02	21.67	1.17
901	6.51	20.37	1.18
1001	6.03	18.81	1.18

B.2 Spent Block

B.2.1 1767 Day Electrolyte Zone S-1

Table B.8: Thermal conductivity data for spent block S-1.

Temperature [^{o}C]	**Thermal Diffucivity** [m^2/s]	**Thermal Conductivity** [W/(m·K)]	**Specific Heat** [J/(kg·K)]
26	15.77	31.65	0.86
102	12.61	30.89	1.05
201	9.90	27.95	1.19
301	8.08	24.81	1.31
352	7.43	23.53	1.35
402	6.61	21.46	1.39
453	5.74	19.02	1.43
503	5.00	16.88	1.47

B.2.2 1767 Day Electrolyte Zone S-2

Table B.9: Thermal conductivity data for spent block 1767 day S-2.

Temperature [^{o}C]	**Thermal Diffucivity** [m^2/s]	**Thermal Conductivity** [W/(m·K)]	**Specific Heat** [J/(kg·K)]
26	11.27	23.32	0.90
102	9.35	22.93	1.03
201	7.17	19.88	1.18
301	5.70	17.01	1.27
352	5.22	16.02	1.31
402	4.32	13.55	1.34
453	3.69	11.79	1.38
503	3.26	10.59	1.41

B.2.3 1767 Day Electrolyte Zone S-3

Table B.10: Thermal conductivity data for spent block 1767 day Bottom S-3.

Temperature [^{o}C]	**Thermal Diffucivity** [m^2/s]	**Thermal Conductivity** [W/(m·K)]	**Specific Heat** [J/(kg·K)]
26	11.94	23.94	0.68
102	9.80	24.19	0.87
201	7.65	21.89	1.00
301	6.02	18.77	1.08
352	5.39	17.46	1.10
402	4.30	14.21	1.14
453	3.60	12.14	1.18
503	3.33	11.44	1.20

B.2.4 1767 Day Electrolyte Zone S-7

Table B.11: Thermal conductivity data for spent block 1767 day S-7.

Temperature [^{o}C]	**Thermal Diffucivity** [m^2/s]	**Thermal Conductivity** [W/(m·K)]	**Specific Heat** [J/(kg·K)]
26	13.75	28.50	0.72
102	11.43	28.29	0.92
201	8.37	23.57	1.01
301	6.67	20.27	1.10
351	5.90	18.34	1.05
402	5.29	16.92	1.15
452	4.57	14.90	1.19
503	4.08	13.53	1.21

B.2.5 1767 Day Electrolyte Zone S-9

Table B.12: Thermal conductivity data for spent block 1767 day S-9.

Temperature [^{o}C]	**Thermal Diffucivity** [m^2/s]	**Thermal Conductivity** [W/(m·K)]	**Specific Heat** [J/(kg·K)]
27	11.95	24.43	0.71
102	9.46	23.27	0.91
201	7.33	20.64	1.01
301	6.03	18.40	1.09
352	5.48	17.20	1.13
402	4.85	15.60	1.15
452	4.27	14.01	1.18
502	3.84	12.81	1.20

B.2.6 1767 Day Gas Zone Top 3-2

Table B.13: Thermal conductivity data for spent block 1767 day Top 3-2.

Temperature [^{o}C]	**Thermal Diffucivity** [m^2/s]	**Thermal Conductivity** [W/(m·K)]	**Specific Heat** [J/(kg·K)]
27	13.25	24.69	0.68
102	10.92	24.30	0.86
201	8.82	22.36	0.94
301	7.64	20.93	1.01
402	6.77	19.53	1.08
501	6.11	18.29	1.12
602	5.64	17.34	1.13
702	5.25	16.45	1.18
802	4.95	15.77	1.23
901	4.61	14.87	1.22

B.2.7 1767 Day Gas Zone Top 3-4

Table B.14: Thermal conductivity data for spent block 1767 day Top 3-4.

Temperature [^{o}C]	**Thermal Diffucivity** [m^2/s]	**Thermal Conductivity** [W/(m·K)]	**Specific Heat** [J/(kg·K)]
28	7.64	13.84	0.65
102	6.48	14.04	0.85
201	5.36	13.31	0.93
301	4.72	12.70	1.00
402	4.28	12.14	1.06
501	3.94	11.61	1.11
603	3.66	11.07	1.11
702	3.44	10.64	1.16
802	3.26	10.23	1.21
901	3.09	9.84	1.21

B.2.8 1767 Day Gas Zone Top 3-5

Table B.15: Thermal conductivity data for spent block 1767 day Top 3-5.

Temperature [^{o}C]	**Thermal Diffucivity** [m^2/s]	**Thermal Conductivity** [W/(m·K)]	**Specific Heat** [J/(kg·K)]
26	6.80	12.61	0.70
102	5.55	12.19	0.83
201	4.63	11.49	0.92
301	4.10	10.99	0.99
402	3.72	10.46	1.05
501	3.40	9.92	1.09
603	3.19	9.55	1.12
702	3.01	9.17	1.15
802	2.84	8.80	1.19
901	2.71	8.50	1.19

B.2.9 1767 Day Gas Zone Top 4-2

Table B.16: Thermal conductivity data for spent block 1767 day Top 4-2.

Temperature [^{o}C]	**Thermal Diffucivity** [m^2/s]	**Thermal Conductivity** [W/(m·K)]	**Specific Heat** [J/(kg·K)]
28	8.39	15.37	0.65
102	7.40	16.28	0.86
201	6.22	15.65	0.95
301	5.44	14.83	1.02
402	4.89	14.06	1.08
501	4.47	13.36	1.12
603	4.13	12.70	1.14
702	3.89	12.19	1.17
801	3.69	11.78	1.22
901	3.49	11.28	1.21